Magnetic materials consist of a wide variety of metals and oxides. Their effective properties are given by a combination of two property categories: *intrinsic* properties which are the atomic moment per atom p_{at}, Curie temperature T_c, magnetocrystalline anisotropy coefficients K_i, and magnetostriction coefficients λ_i; and *extrinsic* properties which are essentially their coercivity H_c and their magnetisation M or magnetic Induction J as a function of the applied magnetic field H. Moreover, the effective properties are depending decisively on the microstructural features, texture and, in most cases, on the external geometric dimensions such as thickness or shape of the magnetic part. In some cases non-magnetic inorganic and organic compounds serve as binders or magnetic insulators in multiphase or composite magnetic materials.

4.3.1 Basic Magnetic Properties

Basic magnetic properties of metallic systems and materials are treated by *Gignoux* in [3.1]. Extensive data on magnetic properties of metals can be found in [3.2]. Magnetic properties of ferrites are treated by *Guillot* in [3.3]. Extensive data on magnetic and other properties of oxides and related compounds can be found in [3.4] and [3.5].

4.3.1.1 Atomic Moment

The suitability of a metal or oxide to be used as a magnetic material is determined by its mean atomic moment (p_{at}). For metals the Bethe–Slater–Pauling curves, Fig. 4.3-1, indicate how p_{at} depends on the average number (n) of 3d and 4s electrons per atom, and on the crystal structure, i. e., face-centered cubic (fcc) or body-centered cubic (bcc) structure. Alloys based on Fe, Co, and Ni are most suitable from this point of view, corresponding to their actual use. The characteristic temperature dependence of the spontaneous magnetization $I_s(T)$, shown for Fe in Fig. 4.3-2, the Curie temperature T_c and the spontaneous magnetization at room temperature I_s (see Table 4.3-1), are the ensuing properties.
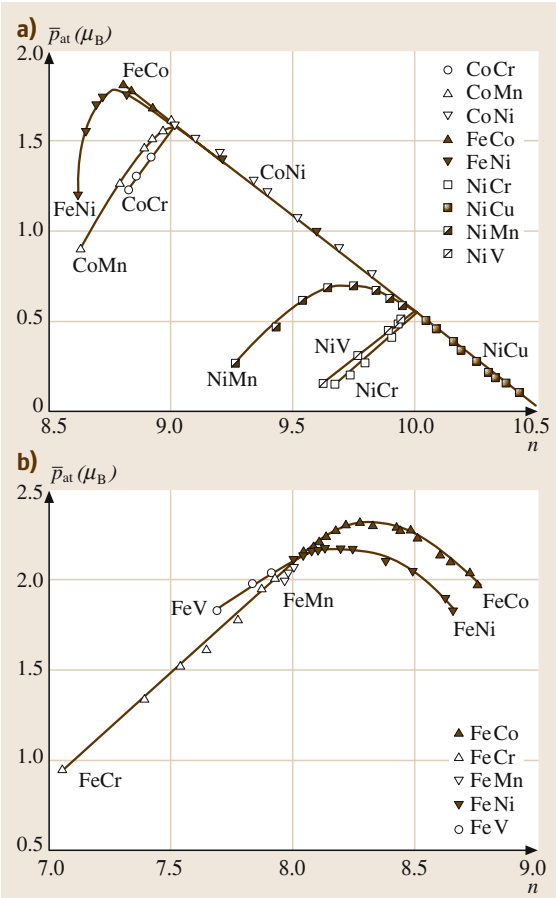
a) $\bar{p}_{at}\,(\mu_B)$

b) $\bar{p}_{at}\,(\mu_B)$

Fig. 4.3-1a,b Bethe–Slater–Pauling relation indicating the dependence of the mean magnetic moment per atom p_{at} on the average number n of 3d and 4s electrons per atom for binary alloys with **(a)** fcc structure and **(b)** bcc structure [3.6]
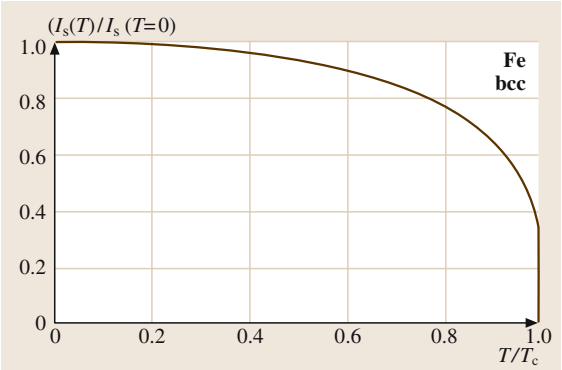
$(I_s(T)/I_s\,(T=0))$

Fig. 4.3-2 Reduced spontaneous magnetization $I_s(T)/I_s$ $(T=0)$ vs. reduced temperature T/T_c for Fe [3.6]

4.3.1.2 Magnetocrystalline Anisotropy

Since the magnetic moment arises from the exchange coupling of neighboring ions, it is also, coupled to their positions in the crystal structures. Basically this is the origin of the magnetocrystalline anisotropy which plays a major role as an intrinsic property for the optimization of both soft and hard magnetic materials because it determines the crystallographic direction and relative magnitude of easy magnetization. As an example, Fig. 4.3-3a shows the magnetization curves for a single crystal of Fe in the three major crystallo-

a) $I\,(T)$

b)

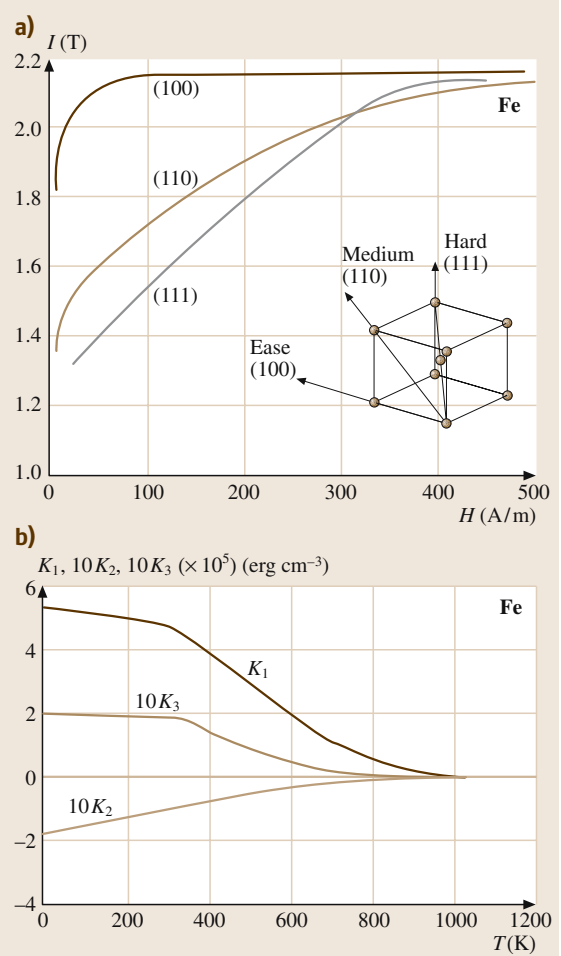$K_1,\,10K_2,\,10K_3\,(\times 10^5)\,(\text{erg cm}^{-3})$

Fig. 4.3-3a,b Magnetization curves of an Fe single crystal indicting the typical characteristics of **(a)** magnetocrystalline anisotropy and **(b)** the temperature dependence of the magnetocrystalline anisotropy constants K_i of Fe [3.6]

Table 4.3-1 Curie temperatures and intrinsic magnetic properties at room temperature

Element	T_c (K)	I_s (T)	K_1 ($10^4\,\mathrm{J\,m^{-3}}$)	K_2 ($10^4\,\mathrm{J\,m^{-3}}$)	K_3 ($10^4\,\mathrm{J\,m^{-3}}$)	λ_{100} (10^{-6})	λ_{111} (10^{-6})	λ_{0001} (10^{-6})	λ_{1010} (10^{-6})	λ_s (10^{-6})
Fe, bcc	1044	2.15	4.81	0.012	-0.012	22.5	-18.8	–	–	-4
Co, hcp	1388	1.62	41	120	–	–	–	-4	-22	-71
Ni, fcc	624	0.55	-0.57	-0.23	0	-46	-24.3	–	–	-34

graphic directions of the body-centered cubic crystal structure.

The anisotropy constants K_1, K_2, ... are defined for cubic lattices, such as Fe and Ni, by expressing the free energy of the crystal anisotropy per unit volume as

$$E_a = K_0 + K_1 S + K_2 P + K_3 S^2 + K_4 SP + \dots ,$$

with

$$S = \alpha_1^2\alpha_2^2 + \alpha_2^2\alpha_3^2 + \alpha_3^2\alpha_1^2 \quad \text{and} \quad P = \alpha_1^2\alpha_2^2\alpha_3^2 ,$$

where α_i, α_j, and α_k are the direction cosines of the angle between the magnetization vector and the crystallographic axes. Corresponding definitions pertain to the anisotropy constants for other crystal lattices.

In practice it can be important to know not only the room temperature value of the magnetocrystalline anisotropy constants K_i but also their temperature dependence, which is shown for Fe in Fig. 4.3-3b. For many technical considerations it suffices to take the dominating anisotropy constant K_1 into account.

4.3.1.3 Magnetostriction

Magnetostriction is the intrinsic magnetic property which relates spontaneous lattice strains to magnetization. It is treated extensively by *Cullen* et al. in [3.3]. As a crystal property magnetostriction is purely intrinsic. The phenomenon of macroscopic magnetostrictive strains of a single or polycrystalline sample is due to the presence of magnetic domains whose reorientation occurs under the influence of magnetic fields or applied stresses and, thus, is a secondary property which has to be distinguished.

Magnetostriction plays a role in determining a number of different effects:

- As a major factor of influence on the coercivity of soft magnetic materials because it determines the magnitude of interaction of internal stresses of materials with the movement of magnetic domain walls.
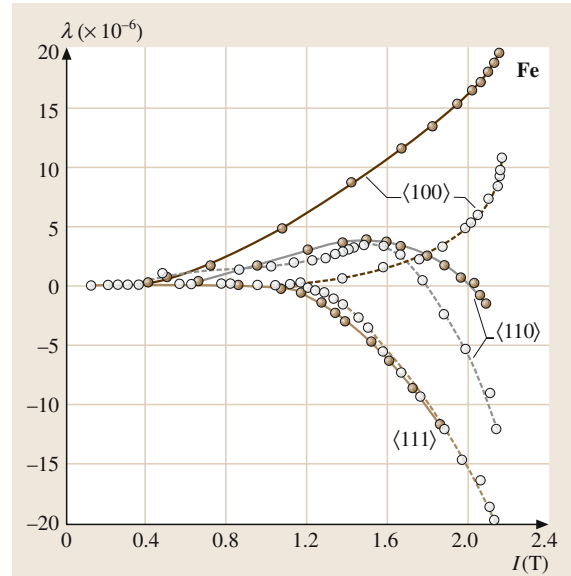

Fig. 4.3-4 Dependence of the magnetostrictive elongation on the magnetization intensity in three different crystallographic directions of Fe single crystals according to two different sources (*open* and *closed circles*) [3.7]

These boundaries are associated with strains themselves unless the material is free of magnetostriction altogether. This is practically impossible because the components of this property vary with the applied magnetic field, as shown for the example of Fe in Fig. 4.3-4. Moreover, they vary with temperature and alloy composition.

- As a decisive variable determining the properties of invar and elinvar alloys (Sect. 4.3.2.8).
- As a property of anomalously high magnitude in cubic Laves phase compounds of rare earth metals such as $Fe_2(Tb_{0.3}Dy_{0.7})$, which are the basis of magnetostrictive materials serving as magnetostrictive transducers and sensors [3.3].

4.3.2 Soft Magnetic Alloys

The basic suitability of a metal or alloy as a soft magnetic material is provided if its Curie temperature T_c and saturation polarization I_s at room temperature are sufficiently high. The main goal in developing soft magnetic materials is to reduce the magnetocrystalline anisotropy constants K_i, in particular K_1, and the magnetostriction constants λ_i, to a minimum. This leads to a minimum energy requirement for magnetization reversal. The appropriate combination of the intrinsic magnetic properties can be achieved by alloying additions and, in some cases, by annealing treatments which induce atomic ordering and, thus, an additional variation of K_1 and/or λ_i. Surveys and data of soft magnetic alloys are given in [3.8].

4.3.2.1 Low Carbon Steels

Low carbon steels are the most widespread magnetic metallic materials for use in electric motors and inductive components such as transformers, chokes, and a variety of other AC applications which require high magnetic induction at moderate to low losses. This is mainly due to the high intrinsic saturation polarization of the base element Fe, $J_s = 2.15\,\text{T}$, and to the low cost of mass produced steels.

Main processing effects on achieving materials with a high relative permeability is the minimization of the formation of particles (mainly carbides and sulfides) which may impede domain boundary motion, and induc-

Table 4.3-2 Standard IEC specification for non-alloyed magnetic steel sheet. The conventional designation of the different grades (first column) comprises the following order: (1) 100 times the maximum specified loss (W kg^{-1}) at 1.5 T; (2) 100 times the nominal sheet thickness in (mm); (3) the characteristic letter "D"; (4) one tenth of the frequency in Hz at which the magnetic properties are specified. The materials are delivered in the semi-processed state. The magnetic properties apply to test specimens heat-treated according to manufacturer's specifications

Grade	Nominal thickness (mm)	Maximum specific total loss for peak induction (W kg^{-1})			Minimum induction in a direct or alternating field at field strength given (T)			Stacking factor	Conventional density (kg dm^{-3})
		1.5 T at at 50 Hz	1.0 T at at 50 Hz	1.5 T at at 60 Hz	at 2500 A/m	at 5000 A/m	at 10 000 A/m		
660-50-D5	0.50	6.60	2.80	8.38	1.60	1.70	1.80	0.97	7.85
890-50-D5	0.50	8.90	3.70	11.30	1.58	1.68	1.79	0.97	7.85
1050-50-D5	0.50	10.50	4.30	13.34	1.55	1.65	1.78	0.97	7.85
800-65-D5	0.65	8.00	3.30	10.16	1.60	1.70	1.80	0.97	7.85
1000-65-D5	0.65	10.00	4.20	12.70	1.58	1.68	1.79	0.97	7.85
1200-65-D5	0.65	12.00	5.00	15.24	1.55	1.65	1.78	0.97	7.85

Table 4.3-3 Standard IEC specifictaion for cold rolled magnetic alloyed steel strip delivered in the semi-processed state. The conventional designation of the different grades comprises the following order (first column): (1) 100 times the maximum specified loss at 1.5 T peak induction in (W kg^{-1}); (2) 100 times the nominal strip thickness, in (mm); (3) the characteristic letter "E"; (4) one tenth of the frequency in Hz, at which the magnetic properties are specified. the magnetic properties apply to test specimens subjected to a reference heat treatment

Grade	Nominal thickness (mm)	Reference treatment temperature (°C)	Maximum specific total loss for peak induction (W kg^{-1})		Minimum induction in a direct or alternating field at field strength given (T)			Conventional density (10^3 kg m^{-3})
			1.5 T	1.0 T	2500 Am^{-1}	5000 Am^{-1}	10 000 Am^{-1}	
340-50-E5	0.50	840	3.40	1.40	1.52	1.62	1.73	7.65
390-50-E5	0.50	840	3.90	1.60	1.54	1.64	1.75	7.70
450-50-E5	0.50	790	4.50	1.90	1.55	1.65	1.76	7.75
560-50-E5	0.50	790	5.60	2.40	1.56	1.66	1.77	7.80

ing a texture – by suitable combinations of deformation and recrystallization – with a preponderance of $\langle 100 \rangle$ and $\langle 110 \rangle$ components, while suppressing the $\langle 111 \rangle$ and $\langle 211 \rangle$ components, such that the operating induction can be aligned most closely to the easiest direction of magnetization $\langle 100 \rangle$. More details are given by *Rastogi* in [3.9]. Tables 4.3-2 and 4.3-3 show characteristic data of nonalloyed magnetic steel sheet and cold rolled magnetic alloyed steel strip, respectively.

4.3.2.2 Fe–based Sintered and Composite Soft Magnetic Materials

Iron-based sintered and composite soft magnetic materials are treated and listed extensively in [3.10]. Iron and Fe based alloys are used as sintered soft magnetic materials because of the particular advantages of powder metallurgical processing in providing net-shaped parts economically. The sintering process serves to achieve diffusion-bonding of the powder particles with a uniform distribution of the alloying elements. The metallic bond and degree of particle contact determine the magnetic properties in each alloy system.

The operating frequency in an application is limited by the resistivity of the material, which is increased beyond that of pure and dense Fe, primarily by varying the type and concentration of alloying elements. Density and crystal structure have a major impact on the magnetic properties, but only a minor effect on the resistivity. The sintered materials have a resistivity ranging from 10 to 80 $\mu\Omega$ cm and are applicable in DC and very low frequency fields. The sintered materials comprise Fe and Fe−P, Fe−Si, Fe−Si−P, Fe−Sn−P, Fe−Ni, Fe−Cr, and Fe−Co alloys. Characteristic data are listed in Tables 4.3-4 to 4.3-11 [3.10].

It is useful to note that the evaluation of a large number of test data of sintered soft magnetic materials yields consistent empirical relations. For sintered Fe products these are:

$$B_{15}[\mathrm{T}] = 4.47\varrho - 10.38 \,,$$

$$B_r[\mathrm{T}] = 3.87\varrho - 17.23 \,,$$

$$H_c[\mathrm{A/m}] = 11.47L^{-0.59} \,,$$

$$\rho[\mu\Omega\,\mathrm{cm}] = -4.34\varrho + 44.77 \,,$$

and

$$\mu_{max} = 0.21L^{0.68} \times 10^3 \,,$$

where ϱ = density (g cm^{-3}) and L = grain diameter (average intercept length) (μm).

Dust core materials consist of Fe or Fe alloy particles which are insolated by an inorganic high resistivity barrier. They are applied in the 1 kHz to 1 MHz range. These are to be distinguished from soft magnetic Fe composite materials, which consist of pure Fe particles separated by an insolating organic barrier, providing a medium to high bulk resistance. Compositions and magnetic properties of Fe based composite materials are listed in Tables 4.3-12 and 4.3-13. These materials are applicable in the frequency range from 50 Hz to 1 kHz.

Table 4.3–4 Magnetic properties of sintered Fe products in relation to density [3.10]

Density ϱ (g cm^{-3})	Sintering conditions temp. (°C), atm.	Induction at 1200 A m^{-1} (T)	Coercivity H_c (A m^{-1})	Remanence B_r (T)	Max. rel. permeability μ_{max}
6.6	1120, DA	0.90	170[a]	0.78[a]	1700
6.6	1120, H$_2$/Vac.	0.95	140[a]	0.82[a]	1800
6.6	1260, H$_2$/Vac.	1.05	120[a]	0.85[a]	2800
6.9	1120, DA	1.05	170[a]	0.90[a]	2100
6.9	1120, H$_2$/Vac.	1.05	140[a]	0.97[a]	2300
6.9	1260, H$_2$/Vac.	1.20	120[a]	1.0[a]	3300
7.2	1120, DA	1.20	170[a]	1.05[a]	2700
7.2	1120, H$_2$/Vac.	1.20	140[a]	1.10[a]	2900
7.2	1260, H$_2$/Vac.	1.30	120[a]	1.15[a]	3800
7.4		1.25	136	1.20	3500
7.4		1.30	112	1.30	5500
7.6		1.50	80	1.40	6000

[a] Measured from a maximum applied magnetic field strength of 1200 A/m.

Table 4.3-5 Magnetic properties of sintered Fe–0.8 wt% P products in relation to density [3.10]

Density ϱ (g cm^{-3})	Sintering conditions temp. (°C), atm.	Induction at 1200 A m^{-1} (T)	Coercitivity H_c (A m^{-1})	Remanence B_r (T)	Max. rel. permeability μ_{max}
6.8	1120, DA	1.05	120[a]	1.00[a]	3500
7.0	1120, H$_2$/Vac.	1.20	100[a]	1.05[a]	4000
7.2	1260, H$_2$/Vac.	1.25	95[a]	1.15[a]	4000
7.0	1120, DA	1.20	120[a]	1.10[a]	4000
7.2	1120, H$_2$/Vac.	1.25	100[a]	1.15[a]	4500
7.4	1260, H$_2$/Vac.	1.30	95[a]	1.20[a]	4500
7.0	1120, DA	1.25	120[a]	1.20[a]	4500
7.2	1120, H$_2$/Vac.	1.30	100[a]	1.30[a]	5000
7.4	1260, H$_2$/Vac.	1.35	95[a]	1.25[a]	5000

[a] Measured from a maximum applied magnetic field strength of 1200 A/m   .

Table 4.3-6 Magnetic properties of sintered Fe–3 wt% Si products in relation to density[a] [3.10]

Density ϱ (g cm^{-3})	Sintering conditions temp. (°C), time, atm.	Coercitivity H_c (A m^{-1})	Remanence B_r (T)	Sat. induction B_s (T)	Max. rel. permeability μ_{max}
7.3		64	1.15	1.90	8000
7.5		48	1.25	2.00	9500
7.2	1250, 30 min, H$_2$ [b]	80	1.0		4300
7.01	1120, 60 min, H$_2$ [b]	117[d]			2800
7.19	1200, 60 min, H$_2$ [b]	88[d]			4200
7.40	1200, 60 min, H$_2$ [c]	79[d]	1.25		5600
7.43	1300, 60 min, H$_2$	56[d]			8400
7.55	1371, DA[e]	51	1.21	1.50	
7.55	1371, DA[e]	57	1.07	1.45	

[a] Measured according to ASTM A 596
[b] Conventional compacting at 600 MPa
[c] Warm compacted at 600 MPa
[d] Defined as coercive force i.e. magnetized to a field strength well below saturation
[e] Formed by MIM

Table 4.3-7 Magnetic properties of sintered Fe−S−P in relation to density[a] [3.10]

Density ϱ (g cm^{-3})	Sintering conditions temp. (°C), atm.	Coercitivity H_c (A m^{-1})	Remanence B_r (T)	Sat. induction B_s (T)	Max. rel. permeability μ_{max}
7.3[b]		45[b]	1.30[b]	1.90[b]	10 800[b]
7.55[c]		33[c]		2.00[c]	12 500[c]
7.3[c]	1250 30 min, H$_2$	60[c]	1.1[c]		6100[c]
6.8[d]	1120 30 min, H$_2$	100[d]	0.6[d]		2200[d]

[a] Measured according to ASTM A 596
[b] Fe/3 wt% Si/0.45 wt% P
[c] Fe/2 wt% Si/0.45 wt% P
[d] Fe/4 wt% Si/0.45 wt% P

Table 4.3-8 Magnetic properties of sintered Fe−Sn−P in relation to density [3.10]

Density ϱ (g cm^{-3})	Sintering temp. (°C), time, atm.	Coercivity H_c (A m^{-1})	Remanence B_r (T)	Max. rel. permeability μ_{max}
7.2 [a]	1120 30 min, H_2 [b]	80 [a]	1.1 [a]	4800 [a]
7.4 [b]	1250 30 min, H_2 [b]	37 [b]	1.0 [b]	9700 [b]

[a] Fe/5 wt% Sn/0.45 wt% P
[b] Fe/5 wt% Sn/0.5 wt% P

Table 4.3-9 Magnetic properties of sintered Fe−Ni in relation to density[a] [3.10]

Density ϱ (g cm^{-3})	Sintering temp. (°C), time atm.	Coercivity H_c (A m^{-1})	Remanence B_r (T)	Sat. induction B_s (T)	Max. rel. permeability μ_{max}
8.0 [b]		24 [b]	0.25 [b]	1.55 [b]	6000 [b]
8.0 [c]		13 [c]	0.85 [c]	1.60 [c]	30 000 [c]
8.5 [d]		2 [d]	0.40 [d]	0.80 [d]	74 900 [d]
6.99 [e]	1260, H_2/Vac.	20 [e]	0.75 [e]		
6.99 [f]		24 [f]	0.76 [f]		7800 [f]
7.30 [e]	1260, H_2/Vac.	19 [e]	0.90 [e]		
7.30 [f]		32 [f]	0.85 [f]		8700 [f]
7.50 [e]	1260, H_2/Vac.	16 [e]	0.94 [e]		21 000 [e]
7.50 [f]		32 [f]	0.90 [f]		9100 [f]
7.4 [c]	1250, 30 min, H_2	25 [c]	0.8 [c]		13 000 [c]
7.66	1371, DA [f]	16	0.42	1.27	

[a] Measured according to ASTM A 596
[b] Fe/35−40 wt% Ni
[c] Fe/45−50 wt% Ni
[d] Fe/72−82 wt% Ni/3−5 wt% Mo
[e] Fe/47−50 wt% Ni
[f] Formed by MIM

Table 4.3-10 Magnetic properties of sintered Fe−Cr in relation to density[a] [3.10]

Density ϱ (g cm^{-3})	Coercivity H_c (A m^{-1})	Remanence B_r (T)	Sat. induction B_s (T)	Max. rel. permeability μ_{max}
7.1 [b]	200 [b]	0.50 [b]		1200 [b]
7.45 [c]	100 [c]		1.70 [c]	2500 [c]
7.35 [d]	100 [d]		1.55 [d]	1900 [d]

[a] Measured according to ASTM A 596
[b] Fe/16−18 wt% Cr/0.5−1.5 wt% Mo
[c] Fe/12 wt% Cr/0.2 wt% Ni/0.7 wt% Si
[d] Fe/17 wt% Cr/0.9 wt% Mo/0.2 wt% Ni/0.8 wt% Si

Table 4.3-11 Magnetic properties of sintered Fe−Co products in relation to density[a] [3.10]

Density ϱ (g cm^{-3})	Coercivity H_c (A m^{-1})	Remanence B_r (T)	Sat. induction B_s (T)	Max. rel. permeability μ_{max}
7.9[b]	136[b]	1.10[b]	2.25[b]	3900[b]

[a] Measured according to ASTM A 596

[b] Fe/47−50 wt% Co/1−3 wt% V

Table 4.3-12 Magnetic properties of composite Fe products in relation to density and insulation [3.10]

Density ϱ (g cm^{-3})	Insulation	Curing (°C) (min)	Coercivity H_c (A m^{-1})	Induction at 3183 A m^{-1} (T)	Max. rel. permeability μ_{max}
5.7−7.26	Polymer		263−374	0.33−0.83	97−245
7.2	Oxide + 0.75 Polymer		374	0.77	210
7.4−7.45	0.75−0.6 % Polymer		381−374	1.09−1.12	400−425
7.54	Oxide				630
7.04	Inorganic (LCM^{TM})				305
7.0	0.5 % Phenolic resin[a]	150, 60	400		270
7.13−6.84[b]	0.4−1.8 % Phenolic[a]	160.30			325−175[c]
7.2[b]	0.8 % Phenolic[a]	150−500.30	445−310		270−390
6.6	3 % resin				200
6.7−7.0	Inorganic & 2 % resin	?−500			200−400
7.4	Inorganic (Somaloy^{TM}500)	500			600

[a] Dry Mixing or wet mixing with phenolic resin

[b] Compacted at 620 MPa and 65 °C

[c] AC permeability at 60 Hz and 1.0 T

Table 4.3-13 Core loss of composite Fe products in relation to lubricant and heat treatment [3.10]

Lubricant	Heat treatment (°C)	(min.)	(Atm.)	Density ϱ (g cm^{-3})	Total loss at 100 Hz, 1.5 T (W kg^{-1})	Total loss at 1000 Hz, 1.5 T (W kg^{-1})
0.1 % Kenolube^{TM} [d]	500	30	air	7.40[b]	29	
0.5 % Kenolube^{TM}	500	30	air	7.20[a]	32	450
0.5−0.8 % Kenolube^{TM}	500	30	air	7.36−7.26[b]	29−31	330−450
0.5 % Kenolube^{TM}	500	30	nitrogen	7.35[b]	31	350
0.5 % Kenolube^{TM}	250−580	30	steam	7.35[b]	30−70	
0.6 % LBI^{TM}	275	60	air	7.27[b]		700
0.5 % Kenolube^{TM}	500	30	air	7.20[a]	35	480
0.5 % Kenolube^{TM}	500	30	air	7.34[a]	34	420

[a] Conventional compacting at 600 MPa

[b] Conventional compacting at 800 MPa

Water atomized iron powder, particle size > 150 μm < 400 μm, low inorganic insulation thickness, (Somatoy^{TM} 550)

4.3.2.3 Iron−Silicon Alloys

The physical basis of the use of Fe−Si alloys, commonly called silicon steels, as soft magnetic materials is the fact that both the magnetocrystalline anisotropy K_1 and the magnetostriction parameters λ_{100} and λ_{111} of Fe approach zero with increasing Si content (see Fig. 4.3-5a). The lower the magnitude of these two intrinsic magnetic properties is, the lower are the coercivity H_c and the AC magnetic losses p_{Fe}. The total losses p_{Fe} consist of the static hysteresis losses p_h and the dynamic eddy current losses p_w which may be subdivided into a classical p_{wc} and an anomalous p_{wa} eddy current loss term,

$$p_{Fe} = p_h + p_{wc} + p_{wa}$$
$$= c_h(f)H_c B f$$
$$+ c_{wc}(\pi d B f)^2/6\rho\gamma + c_{wa}(\alpha_R/\rho)(B f)^{3/2} ,$$

where $c_h(f)$ is a form factor of the hysteresis which depends on the frequency f, H_c is the coercivity of the material, B is the peak operating induction, c_{wc} and c_{wa} are terms taking the wave form of the applied field into account, d is the sheet thickness, ρ is the resistivity, γ is the density of the material, and α_R is the Raleigh constant. These are the factors to be controlled to obtain minimal losses. The increase in electrical resistivity with Si content (Fig. 4.3-5b) adds to lowering the eddy current losses as shown by the relation above.

The Fe−Si equilibrium diagram shows a very small stability range of the γ phase, indicating that the ferromagnetic α phase can be heat-treated in a wide temperature range without interference of a phase transformation which would decrease the magnetic softness of the material by the lattice defects induced.

Next to low-carbon steels, Fe−Si steels are the most significant group of soft magnetic materials (30% of the world market). A differentiation is made between non-oriented, isotropic (NO), and grain-oriented (GO) silicon steels. Non-oriented steels are mainly applied in rotating machines where the material is exposed to varying directions of magnetic flux. Grain-oriented steels with GOSS-texture (110) ⟨001⟩ are used predominantly as core material for power transformers.

Since Fe−Si steels are brittle above about 4.0 wt% Si, conventional cold rolling is impossible at higher Si contents.

Non−oriented Silicon Steels (NO)

NO laminations are usually produced with thicknesses between 0.65 mm and 0.35 mm, and Si concentrations up to 3.5 wt%. According to their grade, NO silicon
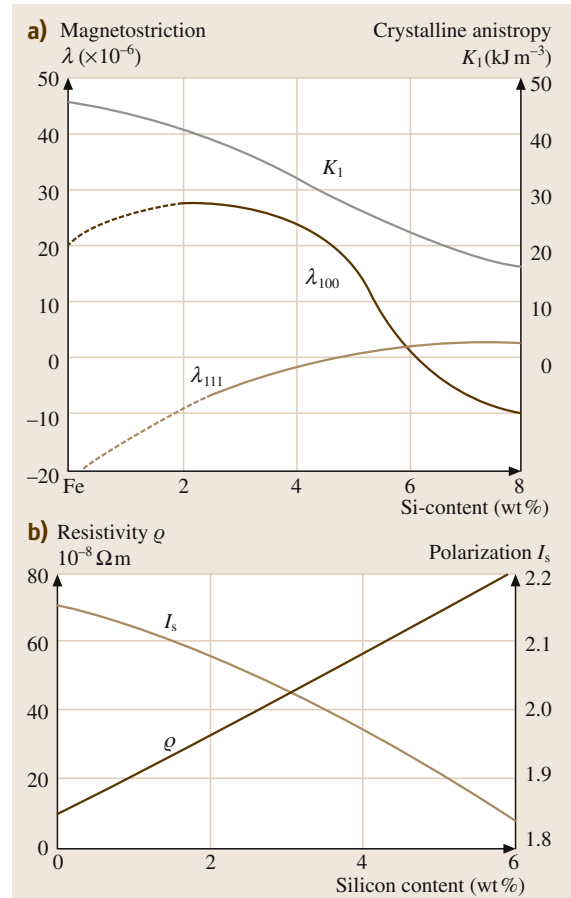

Fig. 4.3-5 (a) Magnetostriction λ_{100} and λ_{111} and magneto-crystalline anisotropy energy K_1. **(b)** Electrical resistivity ρ and saturation polarization I_s, as a function of the Si content in Fe−Si alloys

steels are classified in low grade (low Si content) alloys employed in small devices and high-grade (high Si content) alloys for large machines (motors and generators). Suitable microstructural features (optimum grain size) and a low level of impurities are necessary for optimum magnetic properties. Critical factors in processing are the mechanical behavior upon punching of laminations, the application of insulating coatings, and the build-up of stresses in magnetic cores. Table 4.3-14 lists the ranges of typical processing parameters.

In the case of low Si steels (< 1 wt% Si), the last two annealing steps are applied by the user after lamination punching (semi-finished sheet). Table 4.3-15 lists specifications, including all relevant properties for non-oriented magnetic steel sheet.

Part 4 | 3.2

Composition (wt%) Si: 0.9–3.4, Al: 0.2–0.6, Mn: 0.1–0.3
Melting, degassing, continous casting
Hot rolling to 1.8–2.3 mm (1000–1250 °C)
Cold rolling to intermediate gauge
Annealing (750–900 °C)
Cold rolling to final gauge (0.65–0.35 mm)
Decarburizing anneal (830–900 °C, wet H_2)
Recrystallization
Grain growth anneal (830–1100 °C)
Coating

Table 4.3-14 Schematic of NO silicon steel processing. Addition of small quantities (50–800 wt ppm) of Sb, Sn, or rare earth metals can be made to improve texture and/or control the morphology of the precipitates. Cold reduction in a single stage repesents a basic variant of the above scheme. The final grain growth annealing aims at an optimum grain size, leading to minimum losses. Coating provides the necessary interlaminar electrial insulation. Phosphate- or chromate-based coatings are applied, which ensure good lamination punchability [3.7]

Table 4.3-15 Standard IEC specification for nonoriented magnetic steel sheet delivered in the final sate. The conventional designation of the different grades comprises the following order (first column): (1) 100 times the maximum specified loss at 1.5 T peak induction in (W kg^{-1}); (2) 100 times the nominal sheet thickness; (3) the characteristic letter "A"; (4) one tenth of the frequency in Hz, at which the magnetic properties are specified. The anisotropy of loss, T, is specified at 1.5 T peak induction according to the formula $T = (P_1 - P_2)/(P_1 + P_2)100$, with P_1 and P_2 the power losses of samples cut perpendicular and parallel to the rolling direction, respectively [3.7]

Quality	Nominal thickness (mm)	Maximum specific total loss (W kg^{-1}) at peak induction		Minimum magnetic flux density (T) in direct or alternating field at field strength			Maximum anisotropy of loss (%)	Minimum stacking factor	Minimum number of bends	Conven-tional density (10^3 kg m^{-3})
		1.5 T	1.0 T	2500 Am^{-1}	5000 Am^{-1}	10 000 Am^{-1}				
250-35-A5	0.35	2.50	1.00	1.49	1.60	1.71			2	7.60
270-35-A5	0.35	2.70	1.10	1.49	1.60	1.71	±18	0.95	2	7.65
300-35-A5	0.35	3.00	1.20	1.49	1.60	1.71			3	7.65
330-35-A5	0.35	3.30	1.30	1.49	1.60	1.71			3	7.65
270-50-A5	0.50	2.70	1.10	1.49	1.60	1.71			2	7.60
290-50-A5	0.50	2.90	1.15	1.49	1.60	1.71	±18		2	7.60
310-50-A5	0.50	3.10	1.25	1.49	1.60	1.71			3	7.65
330-50-A5	0.50	3.30	1.35	1.49	1.60	1.71	±14		3	7.65
350-50-A5	0.50	3.50	1.50	1.50	1.60	1.71			5	7.65
400-50-A5	0.50	4.00	1.70	1.51	1.61	1.72		0.97	5	7.65
470-50-A5	0.50	4.70	2.00	1.52	1.62	1.73				7.70
530-50-A5	0.50	5.30	2.30	1.54	1.64	1.75				7.70
600-50-A5	0.50	6.00	2.60	1.55	1.65	1.76	±12		10	7.75
700-50-A5	0.50	7.00	3.00	1.58	1.68	1.76				7.80
800-50-A5	0.50	8.00	3.60	1.58	1.68	1.78				7.80
350-65-A5	0.65	3.50	1.50	1.49	1.60	1.71			2	7.65
400-65-A5	0.65	4.00	1.70	1.50	1.60	1.71			2	7.65
470-65-A5	0.65	4.70	2.00	1.51	1.61	1.72	±14		5	7.65
530-65-A5	0.65	5.30	2.30	1.52	1.62	1.73		0.97	5	7.70
600-65-A5	0.65	6.00	2.60	1.54	1.64	1.75				7.75
700-65-A5	0.65	7.00	3.00	1.55	1.65	1.76	±12		10	7.75
800-65-A5	0.65	8.00	3.60	1.58	1.68	1.76				7.80
1000-65-A5	0.65	10.00	4.40	1.58	1.68	1.78				7.80

Grain-Oriented Silicon Steels (GO)

Grain-oriented (GO) silicon steel is used mainly as core material for power transformers. Worldwide production is about 1.5 million tons per year. The increasing demand for energy-efficient transformers requiring still lower loss materials has led to continuous improvements of the magnetic properties over the years, where a decrease in the deviation from the ideal Goss texture (110)[001] has played a decisive role. Moreover, the eddy current losses have been reduced by decreasing the lamination thickness from 0.35 mm through 0.30 mm and 0.27 mm to 0.23 mm. Surface treatments of the laminations by mechanical scratching or laser scribing have been introduced. They increase the number of mobile Bloch walls and, thus, decrease the spacing between them, i. e., the domain size. Accordingly, the anomalous eddy current losses were reduced. The reduction of the total losses of grain oriented electrical steel due to these improvements is illustrated in Fig. 4.3-6.

The GO steels are classified in two categories: conventional grain-oriented (CGO) and high permeability (HGO) steels. The latter are characterized by a sharp crystallographic texture, with average misorientation of the [001] axes of the individual crystallites around the rolling direction (RD) on the order of 3°. For CGO the misorientation is about 7°. The relation between the angular deviation of grain orientation and the total loss reduction for HGO material is shown in Fig. 4.3-7.

Fig. 4.3-7 Relation between grain orientation and power loss reduction for highly grain-oriented material (single crystal) (*Bölling* and *Hastenrath*) [3.12, 13]

Fig. 4.3-6 Qualitative improvment of GO electrical steel [3.11]

The (GO) manufacturing route is an extraordinarily long sequence of hot and cold processing steps. The final magnetic properties are highly sensitive to even small parameter variations throughout this route. Some of these processes, their microstructure, and the inhibitor element influence are given in Table 4.3-16.

A key factor is the controlled development of the (110)[001] texture during secondary recrystallization. It requires the presence of large Goss textured grains in the surface layers of the annealed hot band, the presence of inhibitors as finely dispersed second-phase particles which strongly impede normal grain growth during primary recrystallization and a primary recrystallized texture having a suitable orientation relationship with respect to the Goss texture. This can be obtained through carefully-controlled chemistry and a precisely-defined sequence of thermomechanical treatments. Abnormal grain growth during secondary recrystallization may increase the size of magnetic domains and consequently greater energy dissipation under dynamic conditions. Refining the domain structure by laser or mechanical scribing core as mentioned above reduces the losses. Standard IEC specifications for grain-oriented magnetic

Part 4 | 3.2

Table 4.3-16 Summary of the processing of grain-oriented silicon steel. The first column relates to the conventional grain-oriented (CGO) laminations. Process for three different types of high permeability (HGO) steels are outlined in columns 2–4. They basically differ for the type of grain growth inhibitors, the cold-rolling sequence, and the annealing temperatures. The processes CGO and HGO-1 adopt a two-stage cold reduction, with intermediate annealing, while HGO-2 and HGO-3 steels are reduced to the final thickness in a single step. Growth inhibition of the primary recrystallized grains is obtained by MnS precipitates in the CGO process. MnSe particles + solute Sb operate in process HGO-1, MnS + AlN particles in HGO-2, and solute B + N + S in HGO-3. Abnormal growth of (110)[001] grains occurs by final box annealing, which also promotes the dissolution of the precipitates [3.7]

Type of Steel							
CGO		**HGO-1**		**HGO-2**		**HGO-3**	
		Composition		(wt%)			
3–3.2	Si	2.9–3.3	Si	2.9–3.3	Si	3.1–3.3	Si
0.04–0.1	Mn	0.05	Mn	0.03	Al	0.02	Mn
0.02	S	0.02	Se	0.015	N	0.02	S
0.03	C	0.04	Sb	0.07	Mn	0.001	B
balance	Fe	0.03–0.07	C	0.03	S	0.005	N
		balance	Fe	0.05–0.07	C	0.03–0.05	C
				balance	Fe	balance	Fe
		Inhibitors					
MnS		MnSe + Sb		MnS + AlN		B + N + S	
Melting, degassing and continuous casting							
		Reheating - hot rolling					
1320 °C		1320 °C		1360 °C		1250 °C	
		Annealing					
800–1000 °C		900 °C		1100 °C		870–1020 °C	
		Cold rolling					
70 %		60–70 %		87 %		80 %	
Annealing							
800–1000 °C							
Cold rolling							
55 %		65 %					
		Decarburizing anneal					
		800–850 °C (wet H$_2$)					
MgO coating and coiling							
		Box-annealing					
1200 °C		820–900 °C		1200 °C		1200 °C	
		+ 1200 °C					
Phospate coating and thermal flattening							

steel sheets are listed in Table 4.3-17. Basic properties of grain-oriented Fe–3.2 wt% Si alloys are given in Table 4.3-18.

A recent technology development in the production of GO electrical steel is the combination of thin slab casting, direct hot rolling, and acquired inhibitor formation. This practice combines the advantages of low temperatures, process-shortening, microstructural homogeneity, improved strip geometry, and better surface condition of the products. The slab thickness is on the order of 50–70 mm. Another future technology with remarkable process shortening is to produce (GO) hot strip in the thickness range of about 2–3 mm by direct casting from the steel melt using a twin-roll casting method. In pilot line tests, good workability and good magnetic properties have been achieved.

Further potential for cost and time saving is expected from replacing box annealing at the end of the cold process by short-time continuous annealing.

Table 4.3-17 Standard IEC specification for grain-oriented magnetic steel sheet: **(a)** normal material; **(b)** material with reduced loss; **(c)** high-permeability material. The conventional designation of the various grades (first column) includes, from left to right, (1) 100 times the maximum power loss, in $(W\,kg^{-1})$, at 1.5 T **(a)** or 1.7 T **(b,c)** peak induction; (2) 100 times the nominal sheet thickness, in (mm); (3) the letter "N" for the nominal material **(a)**, or "S" for material with reduced loss **(b)**, or "P" for high-permeability material **(c)**; (4) one tenth of the frequency in Hz, at which the magnetic properties are specified [3.7]

a) Grade	Thickness (mm)	Maximum specific total loss $(W\,kg^{-1})$ at peak induction		Minimum magnetic flux density (T) for $H = 800\,Am^{-1}$	Minimum stacking factor
		1.5 T	1.7 T		
089-27-N 5	0.27	0.89	1.40	1.75	0.950
097-30-N 5	0.30	0.97	1.50	1.75	0.955
111-35-N 5	0.35	1.11	1.65	1.75	0.960

b) Grade	Thickness (mm)	Maximum specific total loss $(W\,kg^{-1})$ at 1.7 T peak induction	Minimum magnetic flux density (T) for $H = 800\,Am^{-1}$	Minimum stacking factor
130-27-S 5	0.27	1.30	1.78	0.950
140-30-S 5	0.30	1.40	1.78	0.955
155-35-S 5	0.35	1.55	1.78	0.960

c) Grade	Thickness (mm)	Maximum specific total loss $(W\,kg^{-1})$ at 1.7 T peak induction	Minimum magnetic flux density (T) for $H = 800\,Am^{-1}$	Minimum stacking factor
111-30-P 5	0.30	1.11	1.85	0.955
117-30-P 5	0.30	1.17	1.85	0.955
125-35-P 5	0.35	1.25	1.85	0.960
135-35-P 5	0.35	1.35	1.85	0.960

Table 4.3-18 Basic properties of grain-oriented Fe–3.2 wt% Si alloys [3.7]

Property	Value
Density	$7.65 \times 10^3\,kg\,m^{-3}$
Thermal concuctivity	$16.3\,W\,°C^{-1}\,kg\,m^{-3}$
Electrical resistivity	$48 \times 10^{-8}\,\Omega\,m$
Young's modulus	
Single crystals	
[100] direction	120 GPa
[110] direction	216 GPa
[111] direction	295 GPa
(110)[001] texture	
Rolling direction (RD)	122 GPa
45° to RD	236 GPa
90° to RD	200 GPa
Yield strength	
(110)[001] texture	
Rolling direction	324 MPa
Tensile strength	
(110)[001] texture	
Rolling direction	345 MPa
Saturation induction	2.0 T

Table 4.3-18 Basic properties of grain-oriented Fe–3.2 wt% Si alloys [3.7], cont.

Property	Value
Curie temperature	745 °C
Magnetocrystalline anisotropy	3.6×10^4 J m^{-3}
Magnetostriction constants	
λ_{100}	23×10^{-6}
λ_{111}	-4×10^{-6}

Rapidly Solidified Fe–Si Alloys

The Fe–6.5 wt% Si alloy exhibits good high-frequency soft magnetic properties due to a favorable combination of low values of the saturation magnetostriction λ_s, as well as the low values of the magnetocrystalline anisotropy energy K_1, and a high electrical resistivity. But as mentioned above, Fe–Si alloys which contain more than about 4 wt% Si are brittle and thin sheets cannot be manufactured by rolling. Therefore, Fe–6.5 wt% Si sheets and ribbons are manufactured via two different routes by which the adverse mechanical properties are circumvented: a continuous "siliconizing" process in commercial scale production and a rapid quenching process.

In the siliconizing process Fe–3 wt% Si sheet reacts with a Si-containing gas at 1200 °C. The sheet is held at 1200 °C in order to increase and homogenize the Si content by diffusion. After this treatment the ductility of Fe–6.5 wt% Si sheets amounts to about 5% elongation to fracture.

By rapid quenching from the melt, the formation of the B2 and D0$_3$ type ordered structures, based on conventional cooling after casting of Fe–6.5 wt% Si alloys, may be suppressed. Thus, the ensuing material brittleness can be overcome. The ribbons formed by the rapid quenching process are about 20 to 60 μm thick and are ductile, with a microcrystalline structure. By means of an annealing treatment above 1000 °C fol-

Table 4.3-19 Physical and magnetic properties of rapidly quenched Fe–6.5 wt% Si alloys [3.7]

Property	Value
Density	7.48×10^3 kg m^{-3}
Thermal conductivity (31 °C)	4.5 cal m^{-1}°C^{-1}s^{-1}
Specific heat (31 °C)	128 cal °C^{-1} kg^{-1}
Coefficient of thermal expansion (150 °C)	11.6×10^{-6} °C^{-1}
Electrical resistivity	82×10^{-8} Ω m
Tensile strength (rapidly-quenched ribbons 60 μm thick)	630 MPa
Saturation magnetization	1.8 T
Curie temperature	700 °C
Saturation magnetostriction	0.6×10^{-6}

Table 4.3-20 Magnetic properties of 30–40 μm thick, rapidly-quenched ribbons of Fe–6.5 wt% Si, in the as-quenched state and after 24 h annealing at various temperatures [3.7]

Annealing temperature (°C)	H_c (A m^{-1})	H_{10} (T)	B_r/B_{10}	μ_{max}/μ_0
As-quenched	112	1.25	0.70	3100
500	100	1.27	0.93	4300
700	72	1.32	0.90	5400
800	45	1.31	0.92	9400
850	37.5	1.28	0.94	10 000
900	33	1.30	0.77	12 500
1000	21	1.31	0.83	17 000
1100	18	1.30	0.84	18 000
1200	20	1.32	0.87	22 000

lowed by rapid cooling to restrain D0$_3$ type ordering, large-grain-sized, recrystalllized (100) $\langle 0vw \rangle$ textured material with good ductility and good soft magnetic properties is obtained, as characterized in Tables 4.3-19 and 4.3-20. Figures 4.3-8 and 4.3-9 show the loss behavior as a function of magnetizing frequency and ribbon thickness.
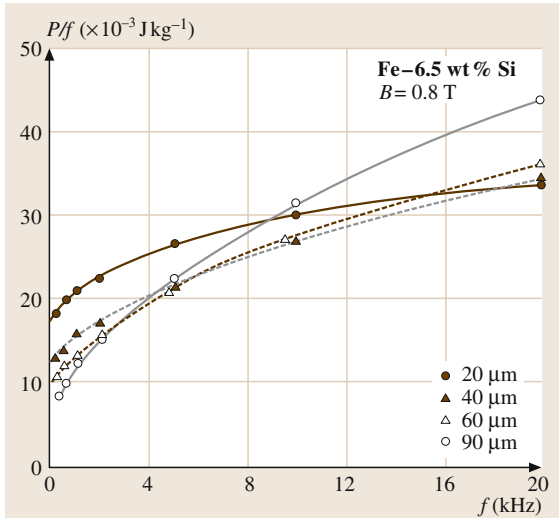

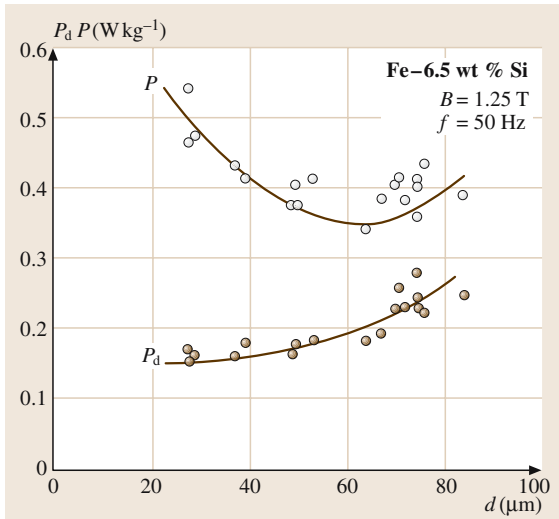**Fig. 4.3-8** Power loss per cycle vs. magnetizing frequency for rapidly quenched Fe–6.5 wt% Si ribbons of various thicknesses [3.7]

Fig. 4.3-9 Total and dynamic loss at 1.25 T peak induction and 50 Hz vs. ribbon thickness for rapidly quenched Fe–6.5 wt% Si ribbons characterized by a strong (100) [0uv] grain texture induced by vacuum annealing [3.7]

4.3.2.4 Nickel−Iron-Based Alloys

The fcc phase in the Ni−Fe alloy system and the formation of the ordered Ni$_3$Fe phase provide a wide range of structural and magnetic properties for developing soft magnetic materials with specific characteristics for different applications. The phase diagram is shown in Sect. 3.1.5. Before amorphous and nanocrystalline soft magnetic alloys were introduced, the Ni−Fe materials
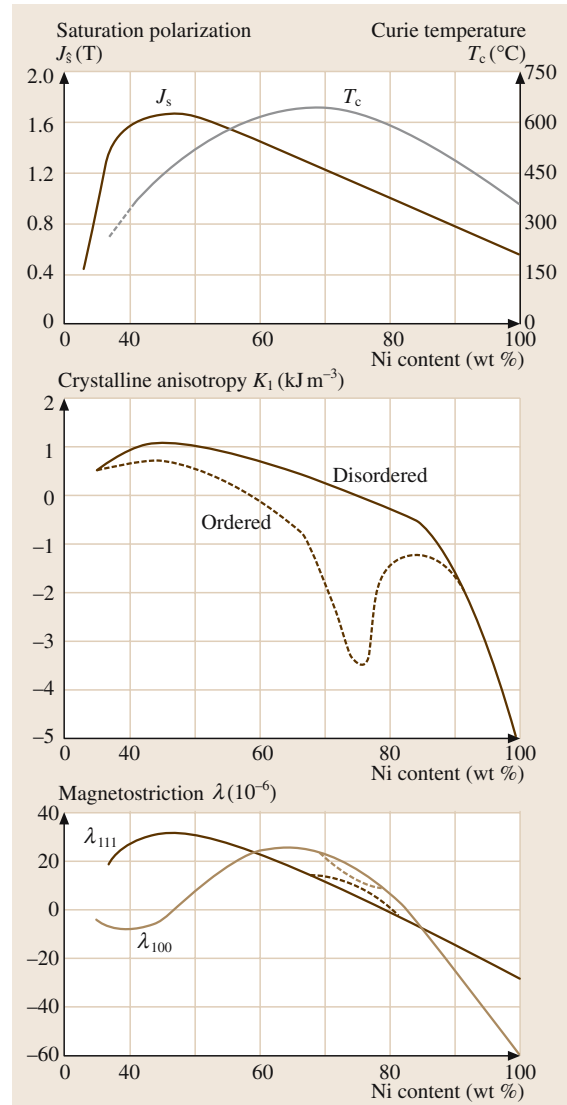
Fig. 4.3-10 The dependence of the intrinsic magnetic parameters I_s, T_c, K_1, λ of Ni−Fe alloys on the Ni concentration [3.12]
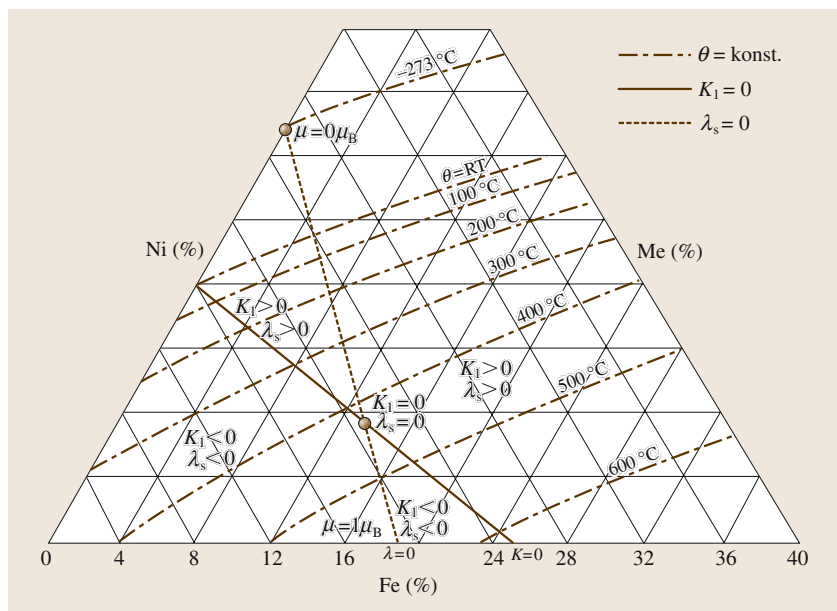
Fig. 4.3-11 Zero lines for $K_1 = 0$ and $\lambda_s = 0$ in the Ni−Fe−Me system [3.14, 15]

containing about 72 to 83 wt% Ni with additions of Mo, Cu, and/or Cr were the magnetically softest materials available.

Based on the low magnetocrystalline anisotropy K_1 and low saturation magnetostriction λ_s, the alloys containing about 80 wt% Ni where K_1 and λ_s pass through zero attain the lowest coercivity $H_c \approx 0.5 \, \mathrm{A \, m^{-1}}$ and the highest initial permeability $\mu_i \approx 200\,000$. Figure 4.3-10 shows the variation of the decisive intrinsic magnetic parameters I_s, T_c, K_1, λ_{100}, and λ_{111} of binary Ni−Fe alloys with the Ni concentration. The strong effect of structural ordering on the magnitude of K_1 should be noted because it permits control of this intrinsic magnetic property by heat treatment.

In the binary Ni−Fe system, $K_1 = 0$ at about 76 wt% Ni and $\lambda_s = 0$ at about 81 wt% Ni. Small additions of Cu lower the Ni content for which $\lambda_s = 0$ while Mo additions increase the Ni content for $K_1 = 0$. Thus different alloy compositions around 78 wt% Ni are available which have optimal soft magnetic properties. General relations of the effect of alloying elements in Ni−Fe-based alloys on K_1, λ_s, and on the permeability have been developed in [3.14, 15]. Figure 4.3-11 shows the position of the lines for $K_1 = 0$ and $\lambda_s = 0$ in the disordered Ni−Fe−Me system, where Me = Cu, Cr, Mo, W, and V. High permeability regions in the Ni−Fe−Me system with a different valence of Me are delineated in Fig. 4.3-12.

The main fields of application of high permeability Ni−Fe alloys are fault-current circuit breakers, LF and HF transformers, chokes, magnetic shielding, and high sensitivity relays.

It should be noted that annealing treatments in a magnetic field of specified direction induce atomic rearrangements which provide an additional anisotropy termed uniaxial anisotropy K_u. It can be used to modify the field dependence of magnetic induction in such a way that the hysteresis loop takes drastically different forms, as shown in Fig. 4.3-13.

The extremes of a steep loop (Z type) and a skewed loop (F type) are obtained by field annealing with the direction of the field (during annealing) longitudinal and transverse to the operating field of the product, respectively. Materials with Z and F loops produced by magnetic field annealing are used in magnetic amplifiers, switching and storing cores, as well as for pulse and instrument transformers and chokes.

Combined with small alloy variations, primary treatments and field annealing treatments, a wide variety of annealed states can be realized to vary the induction behavior. The field dependence of the permeability of some high-permeability Ni−Fe alloys (designations according to Vacuumschmelze GmbH) are shown in Fig. 4.3-14 [3.16].

Alloys of Ni−Fe in the range of 54−68 wt% Ni combine relatively high permeability with high saturation
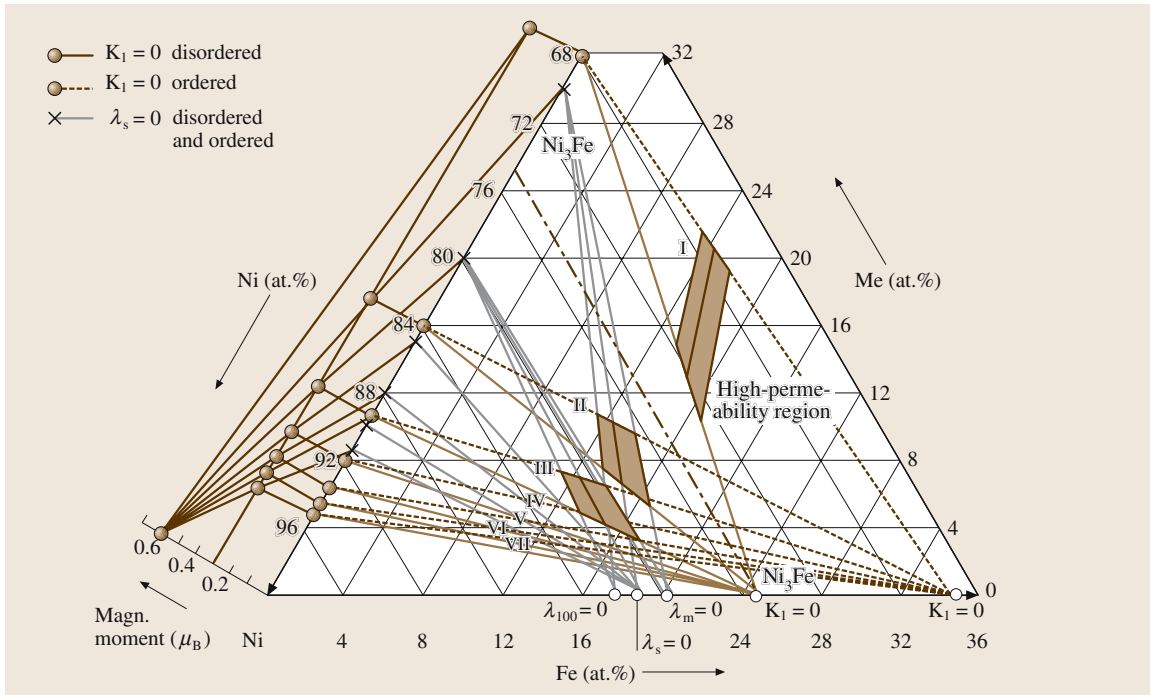
Fig. 4.3-12 Schematic representation of high-permeability regions in the ternary system Ni−Fe−Me by means of the zero curves K_1, $\lambda_{100} = 0$ and $\lambda_{111} = 0$ for additives with valence I–VIII [3.15]
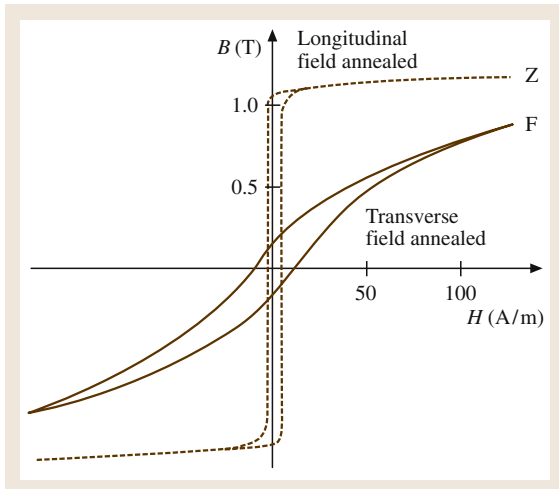

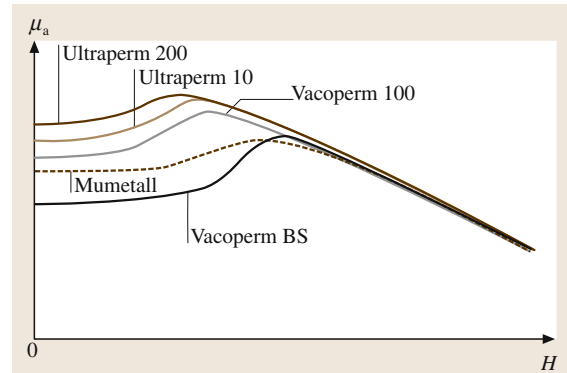**Fig. 4.3-13** Alloy of the 54−68 wt% NiFe-group with Z- and F-loop [3.12]

Fig. 4.3-14 Permeability versus field strength for high permeability high Ni-content Ni−Fe-alloys of Vacuumschmelze Hanau

polarization. Magnetic field annealing of these alloys provides a particularly high uniaxial anisotropy with ensuing Z and F type loops [3.12].

Alloys containing 45 to 50 wt% Ni reach maximum saturation polarization of about 1.6 T. Under suitable rolling and annealing conditions a cubic texture with an ensuing rectangular hysteresis loop and further loop variants over a wide range can be realized. The microstructure may vary from fine grained to coarsely grained.

Alloys containing 35 to 40 wt% Ni show a small but constant permeability, $\mu_r = 2000-8000$, over a wide range of magnetic field strength. Moreover,
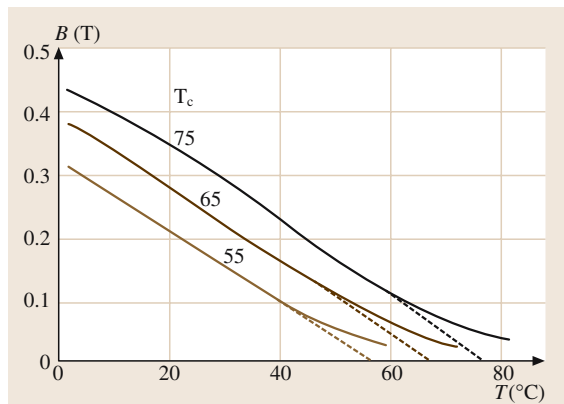
Fig. 4.3-15 Induction vs. temperature of Fe−Ni alloys with approximately 30% Ni as a function of Curie temperature [3.17]

they have the highest resistivity of all Ni−Fe alloys and a saturation polarization between 1.3 and 1.5 T.

The Curie temperature of the alloys with about 30 wt% Ni is near room temperature. Accordingly, the magnetization is strongly temperature-dependent in this vicinity (see Fig. 4.3-15). By slight variation of the Ni content (a composition increase of 0.1 wt% Ni gives rise to an increase of T_c by 10 K) T_c can be varied between 30 °C and 120 °C. These alloys are used mainly for temperature compensation in permanent magnet systems, measuring systems, and temperature sensitive switches [3.16].

4.3.2.5 Iron−Cobalt Alloys

Of all known magnetic materials, Fe−Co alloys with about 35 wt% Co have the highest saturation polarization $I_s = 2.4$ T at room temperature and the highest Curie temperature of nearly 950 °C. The intrinsic magnetic properties I_s, T_c, K_1, and λ_{hkl} as a function of Co content are shown in Fig. 4.3-16.

Since K_1 and λ_s have minima at different Co contents, different compositions for different applications have been developed. A Fe–49 wt% Co–2 wt% V composition is commonly used. The V addition reduces the brittleness by retarding the structural ordering transformation, improves the rolling behavior, and increases the electrical resistivity. The workability of Co−Fe alloys is difficult altogether. Two further alloy variants containing 35 wt% Co and 27 wt% Co, respectively, are of technical interest. They are applied where highest flux density is required, e.g., in magnet yokes, pole
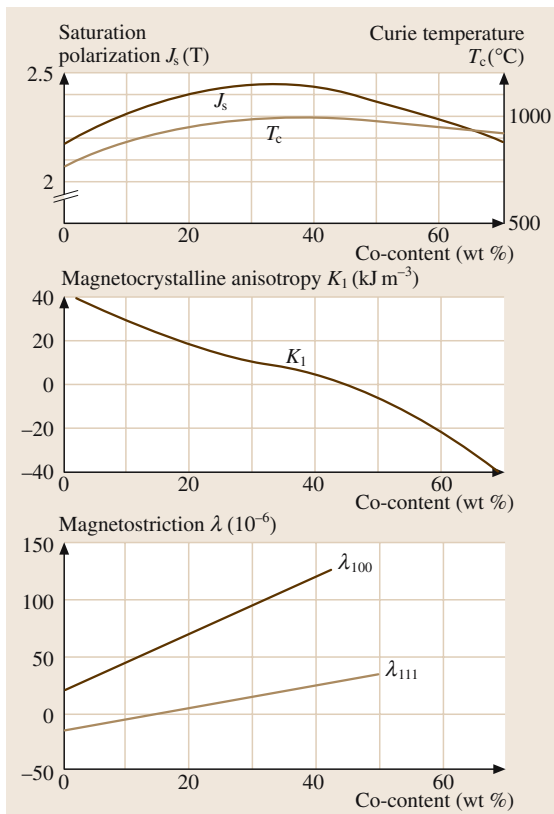

Fig. 4.3-16 The dependence of intrinsic magnetic parameters I_s, T_c, K_1 and λ of Co−Fe alloys on the Co content [3.12]

shoes, and magnetic lenses. The high T_c makes Fe−Co based alloys applicable as high temperature magnet material.

4.3.2.6 Amorphous Metallic Alloys

By rapid quenching of a suitable alloy from the melt at a cooling rate of about 10^{-5}–10^{-6} K/s, an amorphous metallic state will be produced where crystallization is suppressed. Commonly, casting through a slit nozzle onto a rotating copper wheel is used to form a ribbon-shaped product. The thickness of the ribbons is typically between 20 and 40 μm.

From the magnetic point of view amorphous alloys have several advantages compared to crystalline alloys: they have no magnetocrystalline anisotropy, they combine high magnetic softness with high mechanical hardness, their low ribbon thickness and their high electrical resistivity (100−150 μΩ cm)
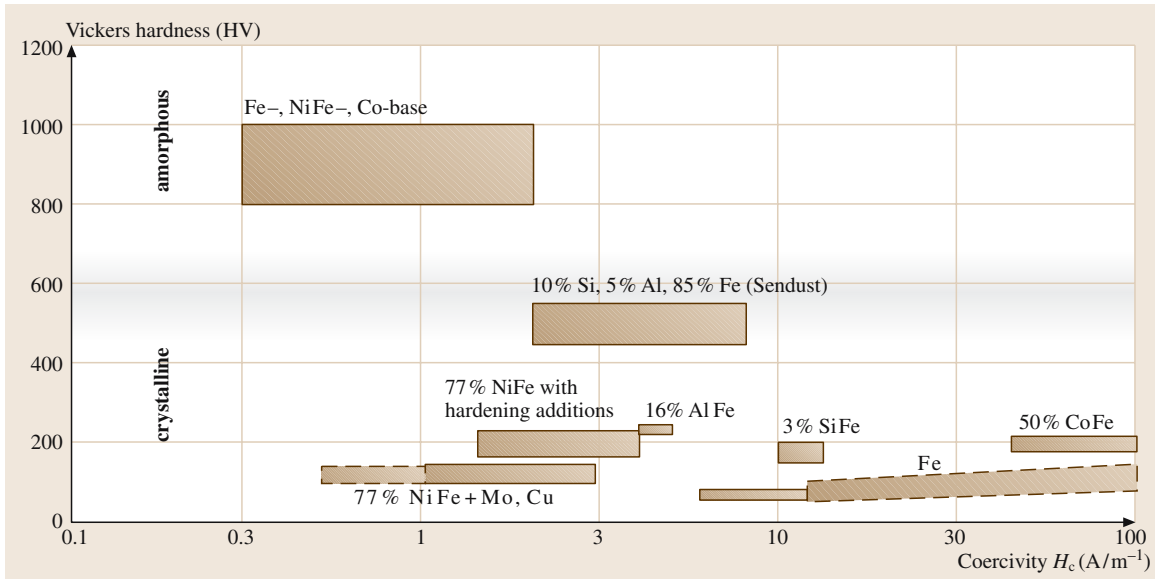
Fig. 4.3-17 Vickers hardness and coercivity of crystalline and amorphous alloys [3.12]

provide excellent soft magnetic material properties for high frequency applications, in particular low losses. A plot of Vickers hardness (HV) vs. coercivity (H_c) for crystalline and amorphous alloys is shown in Fig. 4.3-17 and indicates that a particularly favorable combination for soft magnetic amorphous alloys applies: being magnetically soft and mechanically hard.

The soft magnetic properties of amorphous alloys depend essentially on alloy composition, focusing on a low saturation magnetostriction λ_s, high glass forming ability required for ribbon preparation at technically accessible cooling conditions, and annealing treatments which provide structural stability and field-induced anisotropy K_u.

The soft magnetic amorphous alloys are based on the ferromagnetic elements Fe, Co, and Ni with additions of metalloid elements, the so-called glass forming elements Si, B, C, and P. The most stable alloys contain about 80 at.% transition metal (TM) and 20 at.% metalloid (M) components.

Depending on their base metal they exhibit characteristic differences of technical significance. Accordingly they are classified into three groups: Fe-based alloys, Co-based alloys, and Ni-based alloys. The characteristic variation of their intrinsic magnetic properties saturation polarization I_s, saturation magnetostriction λ_s, and the maximum field induced magnetic
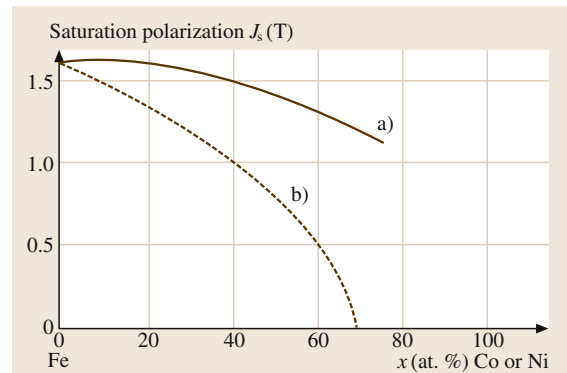

Fig. 4.3-18a,b Saturation polarization J_s of Fe-based amorphous alloys depending on Co and Ni content: **(a)** $Fe_{80-x}Co_xB_{20}$ (*O'Handley*, 1977) [3.18]. **(b)** $Fe_{80-x}Ni_xB_{20}$ (*Hilzinger*, 1980) [3.12, 19]

anisotropy energy K_u, as functions of alloy concentration is shown in Figures 4.3-18 to 4.3-20.

Iron−Based Amorphous Alloys

Of all amorphous magnetic alloys, the iron-rich alloys on the basis $Fe_{\sim 80}(Si, B)_{\sim 20}$ have the highest saturation polarization of 1.5−1.8 T. Because of their relatively high saturation magnetostriction (λ_s) of around 30×10^{-6}, their use as soft magnetic material is limited. The application is focused on transformers at low and
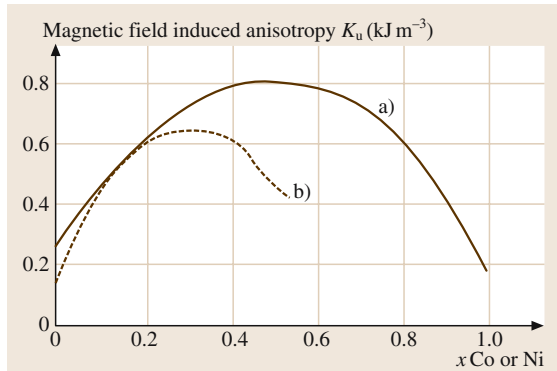
Fig. 4.3-19a,b Field induced anisotropy K_u of FeCo-based and FeNi-based amorphous alloys: **(a)** $(Fe_{1-x}Co_x)_{77}Si_{10}B_{13}$ (*Miyazaki* et al., 1972) [3.20]. **(b)** $(Fe_{1-x}Ni_x)_{80}B_{20}$ (*Fujimori* et al., 1976) [3.12, 21]
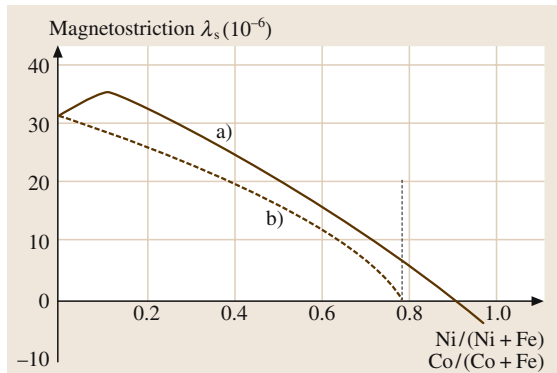

Fig. 4.3-20a,b Magnetostriction λ_s of FeCo-based and FeNi-based amorphous alloys depending on Co and Ni Content: **(a)** $(FeCo)_{80}B_{20}$ [3.18]. **(b)** $(FeNi)_{80}B_{20}$ [3.12, 18]

medium frequencies in electric power distribution systems.

Compared to grain-oriented silicon steels the iron-rich amorphous alloys show appreciably lower coercivity and consequently lower total losses.

The physical and magnetic properties of a characteristic commercial Fe-rich Metglas amorphous alloy are shown in Fig. 4.3-21 and Table 4.3-21 [3.22].
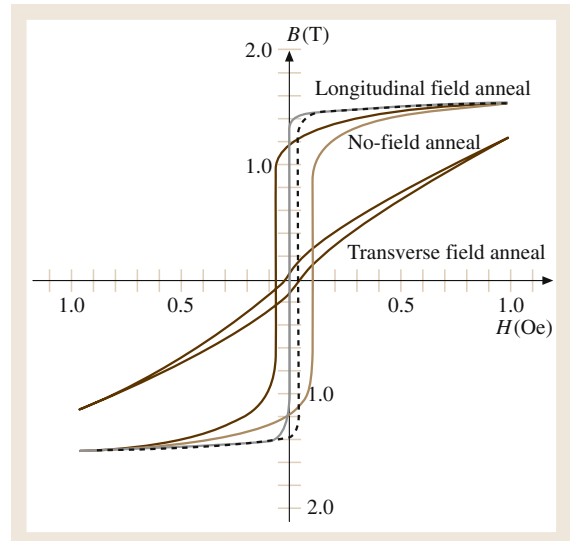

Fig. 4.3-21 Typical dc hysteresis loop of Fe-rich METGLAS alloy SA 1 [3.22]

Cobalt–Based Amorphous Alloys

In the $(Fe_xCo_{1-x})_{\sim80}B_{\sim20}$ system the saturation magnetostriction λ_s passes through zero. Along with a proper selection of alloy composition this behavior gives rise to a particularly low coercivity, the highest permeability of all amorphous magnetic alloys, low stress sensitivity, and extremely low total losses.

The saturation polarization ranging from 0.55 to 1.0 T is lower than in Fe-rich amorphous alloys but comparable to the ~80 wt% Ni crystalline permalloy materials. By applying magnetic field annealing, well-controlled Z-type and F-type loops can be realized.

Nickel–Based Amorphous Alloys

A typical composition of this amorphous alloy group is $Fe_{40}Ni_{40}(Si, B)_{20}$, with a saturation polarization I_s of 0.8 T and a saturation magnetostriction λ_s of 10×10^{-6}. The latter is causing magnetoelastic anisotropy which can be applied to design magnetoelastic sensors where a change in the state of applied stress causes a change in permeability and loop shape, respectively. Upon annealing, Fe–Ni-based alloys will have an R-(round) type

Table 4.3-21 Physical and magnetic properties of Fe-rich METGLAS alloy SA 1 [3.22]

Property	Value
Ribbon Thickness (μm)	25
Density (g/cm^3)	7.19
Thermal Expansion (ppm/°C)	7.6
Crystallization Temperature (°C)	550
Curie Temperature (°C)	415
Countinuous Service Temperature (°C)	155
Tensile Strength (MN/m^2)	1–1.7 k
Elastic Modulus (GN/m^2)	100–110
Vicker's Hardness (50 g load)	860
Saturation Flux Density (Tesla)	1.56
Permeability (depending on gap size)	Variable
Saturation Magnetostriction (ppm)	27
Electrical Resistivity ($\mu\Omega$ cm)	137
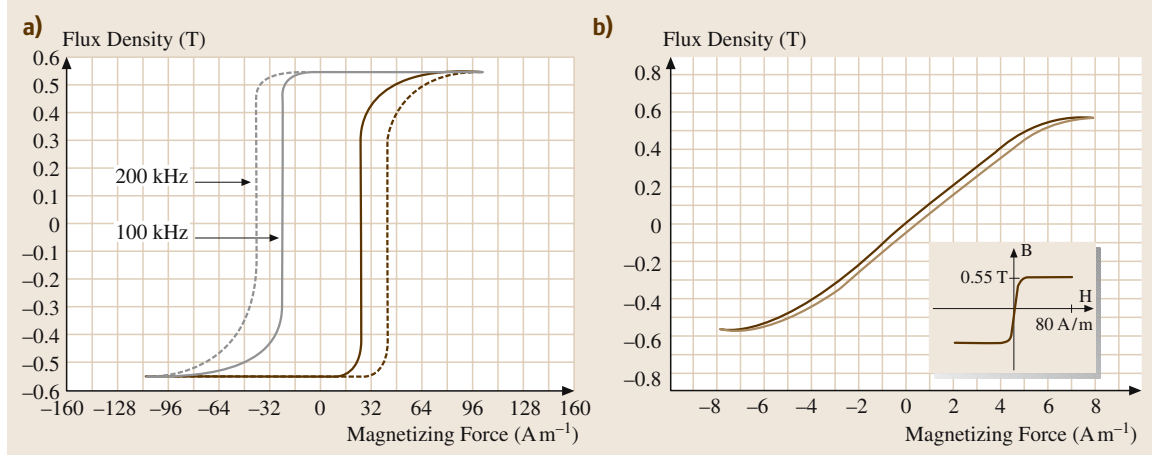
Fig. 4.3-22a,b Typical dc hysteresis loop of Co-based METGLAS alloy: (**a**) alloy 2714 AS (Z-loop) and (**b**) alloy 2714 AF (F-loop) [3.22]

Table 4.3-22 Physical and magnetic properties of the cobalt-based amorphous alloy METGLAS alloy 2714 AF [3.22]

Property	Value
Ribbon Thickness (μm)	18
Density (g/cm^3)	7.59
Thermal Expansion (ppm/°C)	12.7
Crystallization Temperature (°C)	560
Curie Temperature (°C)	225
Countinuous Service Temperature (°C)	90
Tensile Strength (MN/m^2)	1–1.7 k
Elastic Modulus (GN/m^2)	100–110
Vicker's Hardness (50 g load)	960
Saturation Flux Density (Tesla)	0.55
Permeability (μ @ 1 kHz, 2.0 mA/cm)	90 000 ± 20%
Saturation Magnetostriction (ppm)	$\ll 1$
Electrical Resistivity ($\mu\Omega$ cm)	142

Table 4.3-23 Survey of soft magnetic amorphous and nanocrystalline alloys. Some amorphous alloy of METGLAS (Allied Signal Inc., Morristown/NJ) and VITROVAC (Vacuumschmelze GmbH, Hanau, Germany) have been selected from commercially available alloys [3.12]

Composition	Typical properties						
	Saturation polarization in (T)	Curie temperature in (°C)	Saturation magnetostriction in 10^{-6}	Coercivity (dc) in $(A\,m^{-1})$	Permeability[a] at $H = 4\,mA\,m^{-1}$ $\times 10^3$	Density in $(g\,cm^{-3})$	Specific electrical resistivity[b] in $(\Omega\,mm^2\,m^{-1})$
Amorphorus							
Fe-based:							
$Fe_{78}Si_9B_{13}$	1.55	415	27	3	8	7.18	1.37
$Fe_{67}Co_{18}Si_1B_{14}$	1.80	~ 550[c]	35	5	1.5	7.56	1.23
FeNi-based:							
$Fe_{39}Ni_{39}Mo_2Si_{12}B_8$	0.8	260	+8	2	20	7.4	1.35
Co-based:							
$Fe_{67}Fe_4Mo_1Si_{17}B_{11}$	0.55	210	< 0.2	0.3	100	7.7	1.35
$Fe_{74}Fe_2Mn_4Si_{11}B_9$	1.0	480[c]	< 0.2	1.0	2	7.85	1.15
Nanocristalline							
$Fe_{73.5}Cu_1Nb_3Si_{13.5}B_9$	1.25	600	+2	1	100	7.35	1.35

[a] Materials with round (R) or flat loops (F), $f = 50\,Hz$

[b] $1\,\Omega\,mm^2/m = 10^{-4}\,\Omega\,cm$

[c] Extrapolated values ($T_c > T_x$, T_x: crystallization temperature)

hysteresis loop associated with high initial permeability, or an F-type loop with low losses.

Table 4.3-23 gives a survey of the magnetic and physical properties of several soft magnetic amorphous alloys

4.3.2.7 Nanocrystalline Soft Magnetic Alloys

Nanocrystalline soft magnetic alloys are a rather recent class of soft magnetic materials with excellent magnetic properties such as low losses, high permeability, high saturation polarization up to 1.3 T, and near-zero magnetostriction. The decisive structural feature of this alloy type is its ultra-fine microstructure of bcc α-Fe−Si nanocrystals, with grain sizes of 10−15 nm which are embedded in an amorphous residual phase. Originally, this group of materials was discovered in the alloy system Fe−Si−B−Cu−Nb with the composition $Fe_{73.5}Si_{15.5}B_7Cu_1Nb_3$. This material is prepared by rapid quenching like an amorphous Fe−Si−B alloy with a subsequent annealing treatment and comparatively high temperature in the range of 500 to 600 °C which leads to partial crystallization.

The evolution of the nanocrystalline state during annealing occurs by partial crystallization into randomly oriented, ultrafine bcc α-Fe−Si grains that are 10−15 nm in diameter. The residual amorphous matrix phase forms a boundary layer that is 1−2 nm thick. This particular nano-scaled microstructure is the basis for ferromagnetically-coupled exchange interaction of and through these phases, developing excellent soft magnetic properties: $\mu_a \approx 10^5$, $H_c < 1\,A\,m^{-1}$. Annealing above 600 °C gives rise to the precipitation of the borides Fe_2B and/or Fe_3B with grain sizes of 50−100 nm. At higher annealing temperatures, grain coarsening arises. Both of these microstructural changes are leading to a deterioration of the soft magnetic properties.

The influence of the annealing temperature on grain size, H_c, and μ_i of a nanocrystalline type alloy is shown in Fig. 4.3-23 [3.23].

The small additions of Cu and Nb favor the formation of the nanocrystalline structure. Copper is thought to increase the rate of nucleation of α-Fe−Si grains by a preceding cluster formation, and Nb is supposed to lower the growth rate because of its partitioning effect and decrease of diffusivity in the amorphous phase. Figure 4.3-24 illustrates the formation of the nanocrystalline structure schematically.

It is useful to note the influence of the atomic diameter of alloying additions on the grain size of the α-Fe−Si phase starting from the classical alloy composition $Fe_{73.5}Si_{15.5}B_7Cu_1Nb_3$. This effect is shown for
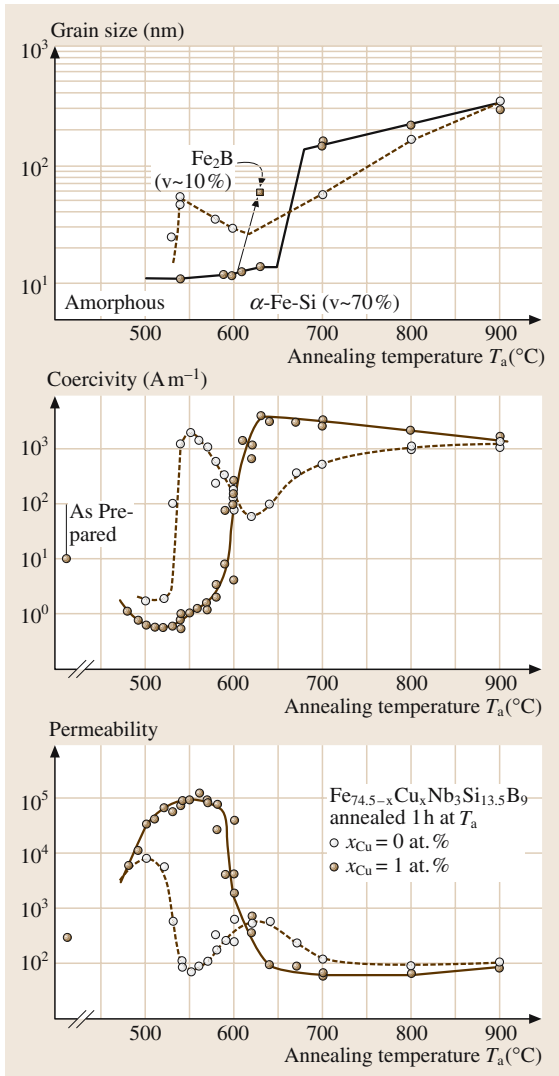
Fig. 4.3-23 Average grain size, coercivity and initial permeability of a nanocrystalline soft magnetic alloy as a function of the annealing temperature [3.23]
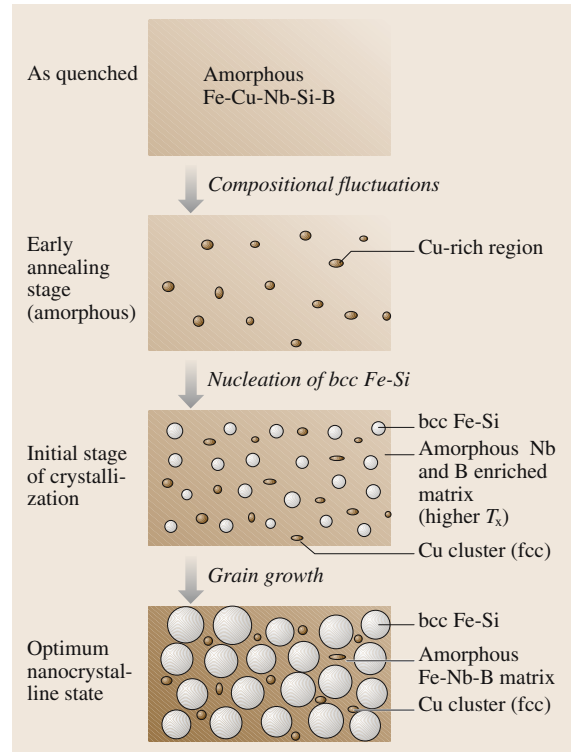

Fig. 4.3-24 Schematic illustration of the formation of the nanocrystalline structure in Fe−Cu−Nb−Si−B alloys, based on atom probe analysis results and transmission electron microscopy observations by *Hono* et al. [3.23, 24]
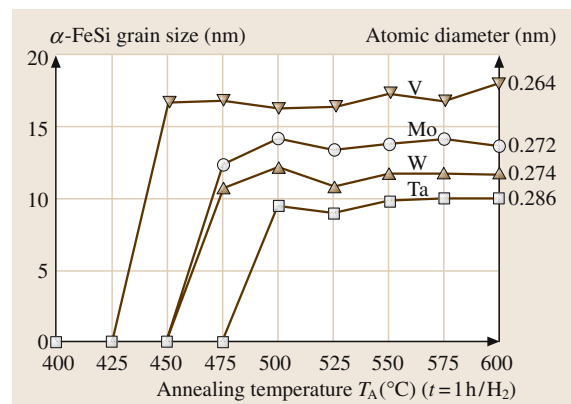
partial substitution of Nb by V, Mo, W, and Ta (2 at.% each) in Fig. 4.3-25. The larger the atomic diameter, the smaller the resulting grain size. The elements Nb and Ta have the same atomic diameter. Furthermore, the smaller the atomic diameter of the alloying element, the sooner the crystallization of the α-Fe-Si phase begins.

One of the decisive requirements for excellent soft magnetic properties is the absence of magnetostriction. Amorphous Fe−Si−B−Cu−Nb alloys have a saturation

Fig. 4.3-25 Influence of partial substitution of Nb by the refractory elements R = V, Mo, W and Ta on the α-FeSi grain size during annealing of the alloy $Fe_{73.5}Si_{15.5}B_7Cu_1Nb_3R_2$ [3.25]
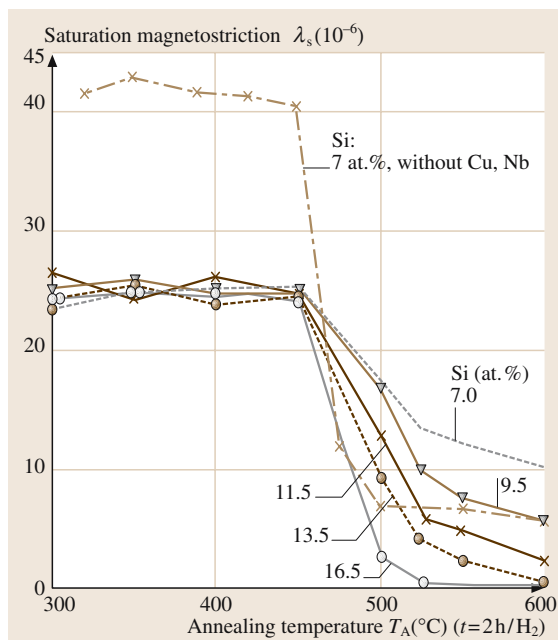
Fig. 4.3-26 Influence of the Si-content on the saturation magnetostriction λ_s during annealing of the nanocrystalline alloys $Fe_{(75-73.5)}Si_{(7-16.5)}B_{(14-6)}Cu_1Nb_3$ [3.26]

magnetostriction $\lambda_s \approx 24 \times 10^{-6}$, with a magnetoelastic anisotropy energy $K_\sigma \approx 50\,J\,m^{-3}$. With partial crystallization of the α-Fe−Si phase during annealing, λ_s varies significantly. At higher Si contents it decreases strongly and passes through zero at about 16 at.% Si, as shown in Fig. 4.3-26.

This behavior is caused by the compensation of the negative saturation magnetostriction λ_s of the α-Fe−Si phase $\lambda_s \approx -8 \times 10^{-6}$ and the positve values of λ_s of the residual amorphous phase of $\lambda_s \approx +24 \times 10^{-6}$.

The superposition of the local magnetostrictive strains to an effective zero requires a large crystalline volume fraction of about 70 vol.% to compensate the high positive value of the amorphous residual phase of about 30 vol.%. By anealing at about 550 °C this relation can be realized. The second requirement for superior soft magnetic properties is a small or vanishing magnetocrystalline anisotropy energy K_1.

By developing a particular variant of the random anisotropy model, it was shown [3.27] that for grain diameters D smaller than the magnetic exchange length L_0, the averaged anisotropy energy density $\langle K \rangle$ is given by

$$\langle K \rangle \approx v_{cr}^2 K_1 (D\,L_0^{-1})^6 = v_{cr}^2 D^6 K_1^4 A^{-3}\,,$$

where v_{cr} = crystallized volume, K_1 = intrinsic crystal anisotropy energy of α-Fe−Si, $L_0 = \sqrt{A\,K_1^{-1}}$, and A = exchange stiffness constant. A schematic representation of this model is given in Fig. 4.3-27. The basic effect of decreasing the grain size consists of local averaging of the magnetocrystalline anisotropy energy K_1 for $D = 10-15\,nm$ at $L_0 = 30-50\,nm$ (about equal to
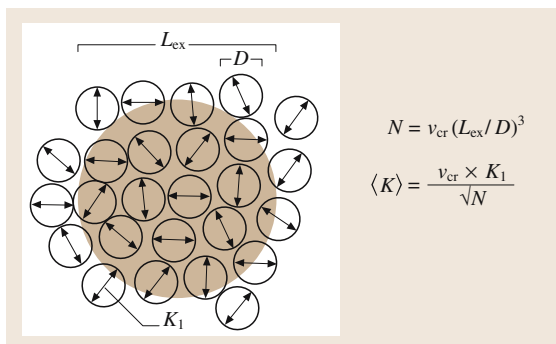

Fig. 4.3-27 Schematic representation of the random anisotropy model for grains embedded in an ideally soft ferromagnetic matrix. The *double arrows* indicate the randomly fluctuating anisotropy axis; the *dark* area represents the ferromagnetic correlation volume determined by the exchange length $L_{ex} = (A/\langle K \rangle)^{1/2}$ [3.23]
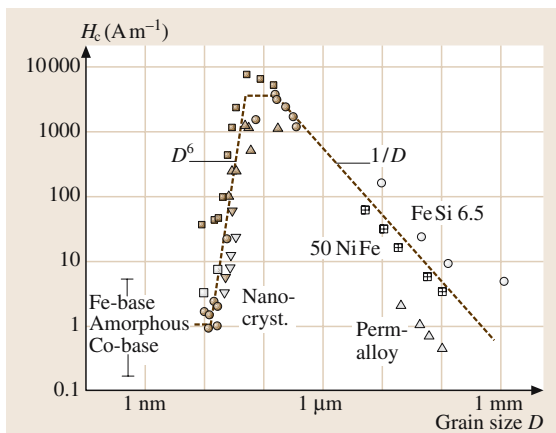

Fig. 4.3-28 Coercivity, H_c, vs. grain size, D, for various soft magnetic metallic alloys [3.27]: Fe−Nb−Si−B (*solid up triangles*) [3.28], Fe−Cu−Nb−Si−B (*solid circles*) [3.29, 30], Fe−Cu−V−Si−B (*solid* and *open down triangles*) [3.31], Fe−Zr−B (*open squares*) [3.32], Fe−Co−Zr (*open diamonds*) [3.33], NiFe-alloys (+ *center squares* and *open up triangles*) [3.34], and Fe−Si(6.5 wt%) (*open circles*) [3.35]

Table 4.3-24 Typical values of grain size D, saturation magnetization J_s, saturation magnetostriction λ_s, coercivity H_c, initial permeability μ_i, electrical resistivity ρ, core losses P_{Fe} at 0.2 T, 100 kHz and ribbon thickness t for nanocrystalline, amorphous, and crystalline soft magnetic ribbons

Alloy	D (nm)	J_s (T)	λ_s (10^{-6})	H_c (A m^{-1})	μ_i (1 kHz)	ρ ($\mu\Omega$ cm)	P_{Fe} (W kg^{-1})	t (μm)	Ref
$Fe_{73.5}Cu_1NB_3Si_{13.5}B_9$	13	1.24	2.1	0.5	100 000	118	38	18	a
$Fe_{73.5}Cu_1NB_3Si_{15.5}B_7$	14	1.23	~ 0	0.4	110 000	115	35	21	b
$Fe_{84}NB_7B_9$	9	1.49	0.1	8	22 000	58	76	22	c
$Fe_{86}Cu_1Zr_7B_6$	10	1.52	~ 0	3.2	48 000	56	116	20	c
$Fe_{91}Zr_7B_3$	17	1.63	-1.1	5.6	22 000	44	80	18	c
$Co_{68}Fe_4(MoSiB)_{28}$	amorphous	0.55	~ 0	0.3	150 000	135	35	23	b
$Co_{72}(FeMn)_5(MoSiB)_{23}$	amorphous	0.8	~ 0	0.5	3000	130	40	23	b
$Fe_{76}(SiB)_{24}$	amorphous	1.45	32	3	8000	135	50	23	b
80 % Ni−Fe (permalloys)	$\sim 100\,000$	0.75	< 1	0.5	100 000[d]	55	>90[e]	50	b
50−60 % Ni−Fe	$\sim 100\,000$	1.55	25	5	40 000[d]	45	>200[e]	70	b

[a] [3.36]

[b] Typical commercial grades for low remanence hysteresis loops, Vacuumschmelze GmbH 1990, 1993

[c] [3.37, 38]

[d] 50 Hz-values

[e] Lower bound due to eddy currents

the domain wall thickness), which leads to the extreme variation of $\langle K \rangle$ with the sixth power of grain size. These relations were confirmed experimentally and result in an anomalous variation of the coercivity with grain size, as shown in Fig. 4.3-28.

Another type of nanocrystalline soft magnetic materials is based on Fe−Zr−B−Cu alloys [3.37, 38]. A typical composition is $Fe_{86}Zr_7B_6Cu_1$. As Zr provides high glass-forming ability, the total content of glass-forming elements can be set to $\ll 20$ at.%. As a consequence the Fe content is higher, which implies higher saturation polarization. The nanocrystalline microstructure consists of a crystalline α-Fe phase with grain sizes of about 10 nm embedded in an amorphous residual phase. After annealing at 600 °C, an optimum combination of magnetic properties is obtained: $I_s \geq 1.5$ T, $H_c \approx 3$ A m^{-1}, $\lambda_s \approx 0$. Because of the high reactivity of Zr with oxygen the preparation of this type of alloy is difficult. The production of these materials on an industrial scale has not yet succeeded.

Table 4.3-24 shows the magnetic and physical properties of some commercially-available nanocrystalline alloys for comparison to amorphous and Ni−Fe-based crystalline soft magnetic alloys. Magnetic field annealing allows the shape of the hysteresis loops of

a) Flux density B(T)

75−80 % NiFe

54−68 % NiFe

Field strength H(A/m)

b) Flux density B(T)

$Fe_{73.5}Cu_1Nb_3Si_{13.5}B_9$ (n)

$Fe_{76}Si_{12}B_{12}$

$Co_{67}Fe_4Mo_1Si_{17}B_{11}$

$Co_{71}Fe_1Mn_4Mo_1Si_{14}B_9$

Field strength H(A/m)

Fig. 4.3-29a,b Soft magnetic alloys with flat hysteresis loops: **(a)** Crystalline. **(b)** Amorphous and nanocrystalline (curve indicated by n) [3.12]
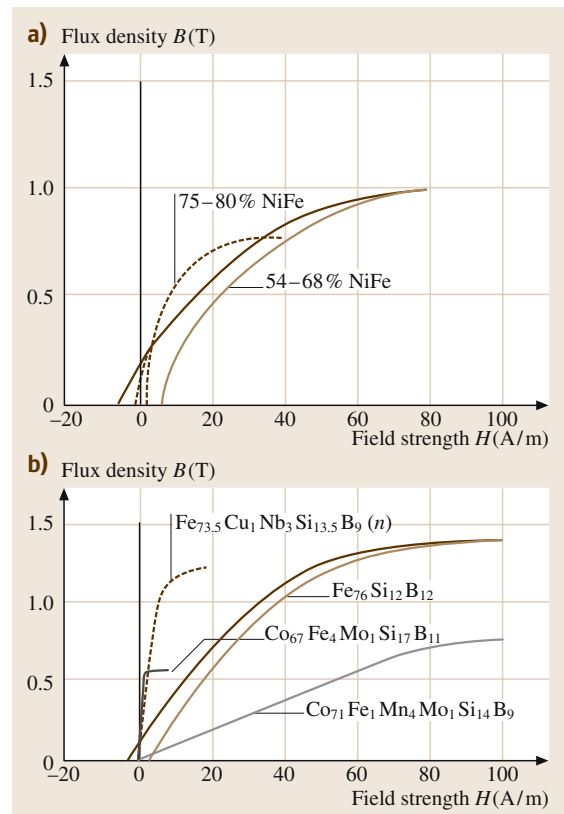
nanocrystalline soft magnetic alloys to be varied according to the demands of the users. Accordingly, different shapes of hystesis loops (Z, F, or R type) may be
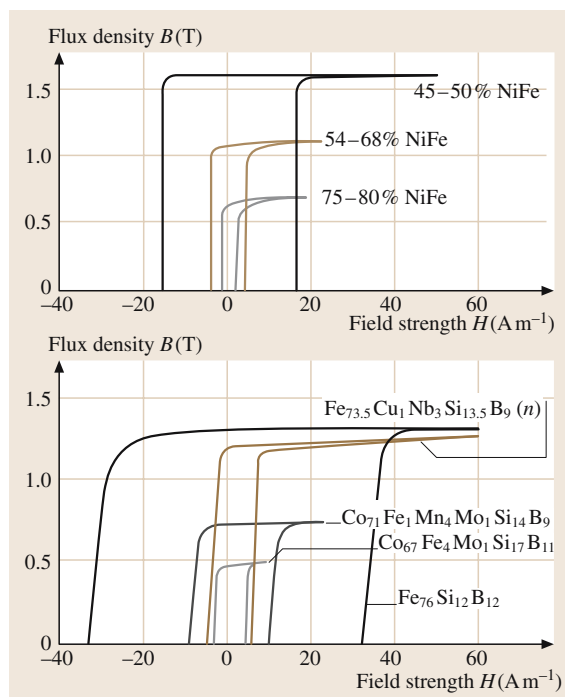

Fig. 4.3-30a,b Soft magnetic alloys with rectangular hysteresis loops: **(a)** Crystalline. **(b)** amorphous and nanocrystalline (curve indicated by n) [3.12]
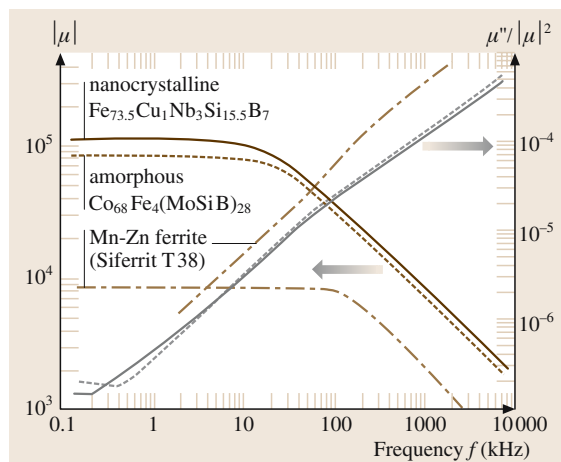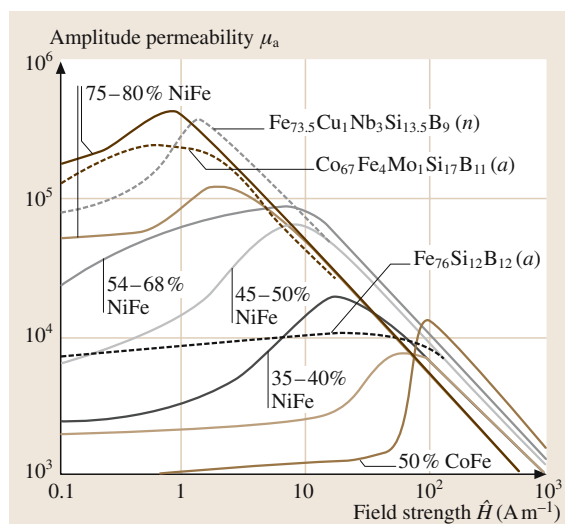

Fig. 4.3-32 Frequency dependence of permeability, $|\mu|$, and the relative loss factor, $\mu''/|\mu|^2$, for nanocrystalline $Fe_{73.5}Cu_1Nb_3Si_{15.5}B_7$ and comparable, low remanence soft magnetic materials used for common mode choke cores [3.23]

achieved. For comparison several characteristic hysteresis loops of crystalline, amorphous, and nanocrystalline soft magnetic alloys are shown in Figs. 4.3-29a,b and 4.3-30a,b.

A survey of the field dependence of the amplitude permeability of various crystalline, amorphous, and nanocrystalline soft magnetic alloys is given in Fig. 4.3-31 [3.12]. Figure 4.3-32 [3.23] represents the frequency behavior of the permeability $|\mu|$ of different soft magnetic materials for comparison.

4.3.2.8 Invar and Elinvar Alloys

The term invar alloys is used for some groups of alloys characterized by having temperature-invariant properties, either temperature-independent volume (invar) or temperature-independent elastic properties (elinvar) in a limited temperature range. A comprehensive survey of the physics and applications of invar alloys is given in [3.17].

Invar Alloys
With the discovery of an Fe–36 wt% Ni alloy with an uncommonly low thermal expansion coefficient (TEC) around room temperature and called "Invar" by Guil-

Fig. 4.3-31 Amplitude permeability–field strength curves of soft magnetic alloys ($f = 50$ Hz): amorphous (a); nanocrystalline (n) [3.12]

laume in the 1890s, the history of invar and elinvar type alloys began. Below the magnetic transition temperature, Curie temperature T_c or Néel temperature T_N of ferromagnetic or antiferromagnetic materials, a spontaneous volume magnetostriction ω_s sets in. With some alloy compositions, ω_s is comparable in magnitude to the linear thermal expansion but opposite in sign. As a result the coefficient of linear thermal expansion may become low and even zero.

The linear (α) and volumetric (β) thermal expansion coefficients (TECs) are defined as:

$$\alpha = (1/l)(\Delta l/\Delta T)_P \quad [\text{K}^{-1}]$$

and

$$\beta = (1/V)(\Delta V/\Delta T)_P \quad [\text{K}^{-1}] ,$$

with l = length, V = volume, and T = temperature. If the alloys are isotropic the volumetric thermal expansion coefficient is equal to three times the linear TEC:

$$\beta = 3\alpha .$$

The spontaneous volume magnetostriction ω_s is in a first approximation:

$$\omega_s = \kappa C M_s^2 ,$$

with κ = compressibility, C = magnetovolume coupling constant, and M_s = spontaneous magnetization. Figure 4.3-33 [3.42] illustrates schematically the

Fig. 4.3-34 Temperature coefficient of linear thermal expansion α at room temperature as a function of the composition in typical invar alloy systems: Fe−Ni [3.39], Fe−Pt [3.40], Fe−Pd [3.40], and Fe−Co−Cr [3.39]. *Vertical dotted lines* show boundary between bcc and fcc phases

temperature-dependent behavior of thermal expansion, ω_s and M_s, which give rise to a small linear expansion coefficient.

Crystalline invar alloys are essentially based on 4 binary alloy systems: Fe−Ni, Fe−Pt, Fe−Pd, and Fe−Co, containing a few percent of Cr. Figure 4.3-34 [3.17] shows the thermal expansion coefficient of these invar type alloy systems. The invar alloy in each system is fcc
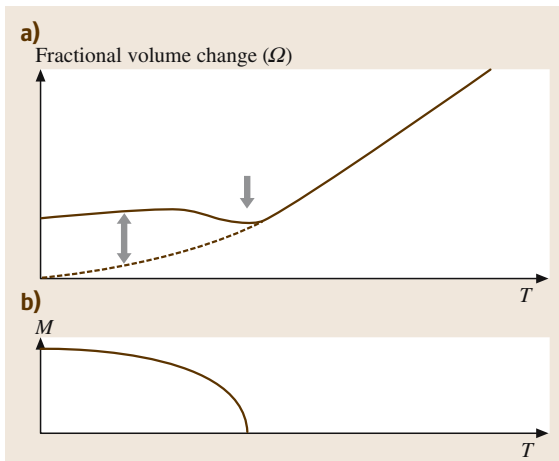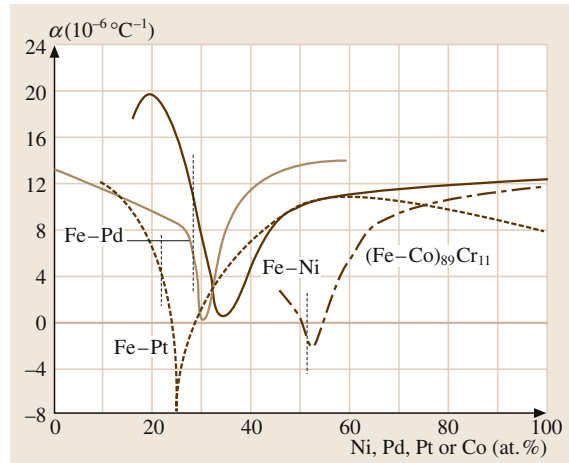

Fig. 4.3-33 (a) Schematic diagram of invar-type thermal-expansion anomaly. The *dashed curve* indicates thermal expansion for hypothetical paramagnetic state. The difference between the two curves corresponds to the spontaneous volume magnetostriction, ω_s. **(b)** Temperature dependence of the spontaneous magnetization
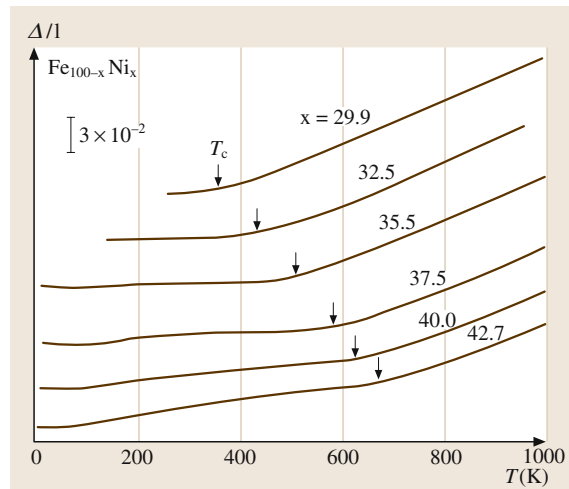

Fig. 4.3-35 Thermal expansion curves of Fe−Ni alloys annealed at 1323 K for 5 days [3.41]
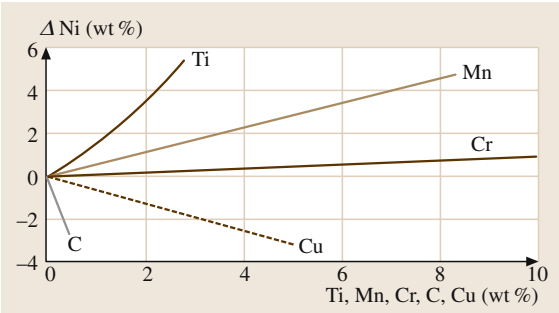
Fig. 4.3-36 Displacement of the composition corresponding to the minimum thermal expansion coefficient of Fe−Ni alloys by the addition of Ti, Mn, Cr, Cu, and C [3.17]
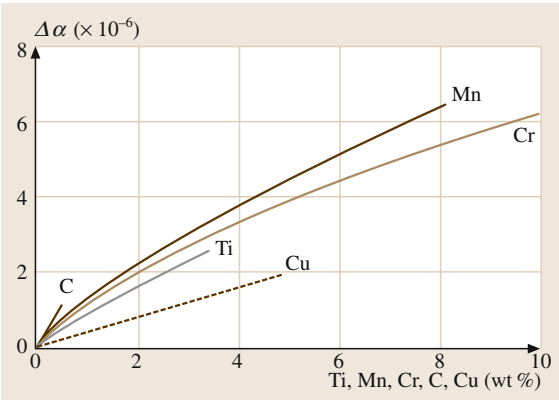

Fig. 4.3-37 Increase of the minimum value of thermal expansion coefficient of Fe−Ni alloys by the addition of Ti, Mn, Cr, Cu, and C [3.17]

and its composition is near the boundary between the bcc and fcc phase fields.

Fe−Ni−Based Invar Alloys. An iron alloy containing 34 to 36.5 wt% Ni is well known as a commercial invar material. The materials C < 0.12 wt%, Mn < 0.50 wt%, and Si < 0.50 wt% are generally added for metallurgical purposes. Figure 4.3-35 [3.41] shows the thermal expansion curves of some Fe−Ni alloys.

The thermal expansion of invar alloys is affected significantly by the addition of third elements,
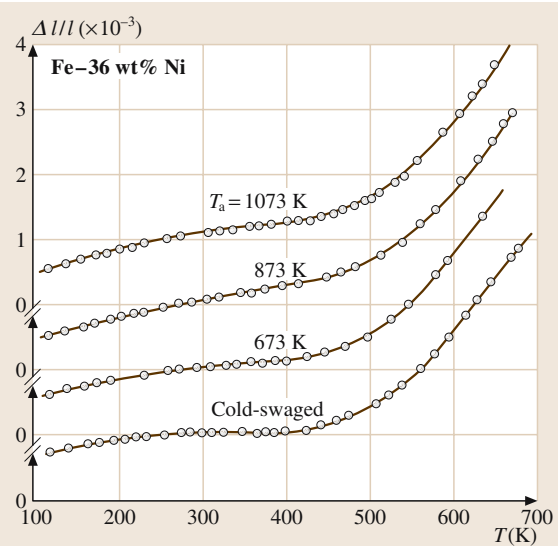
Fig. 4.3-38 Effect of thermal annealing at a temperature T_a and of mechanical treatment on the thermal expansion of Fe–36 at.% Ni invar alloy [3.41]

by cold working and by thermal treatment as shown in Fig. 4.3-36 [3.17], Fig. 4.3-37 [3.17] and Fig. 4.3-38 [3.41].

Invar is an austenitic alloy and cannot be hardened by heat treatment. The effect of heat treatment on the TEC α depends on the method of cooling after annealing. Air cooling or water quenching from the annealing temperature results in a reduction of α but at the same time α becomes unstable. In order to stabilize the material, annealing at low temperature and slow cooling to room temperature are necessary.

Following heat treatments for an optimum and stable magnitude of α are recommended: 830 °C, 1/2 h, water quenching; 315 °C, 1 h, air cooling; 95 °C, 20 h, air cooling. Cold working reduces α. But before use in high precision instruments a stress-relief anneal at 320 to 370 °C for 1 h followed by air cooling is required.

The mechanical properties of some invar-type alloys are listed in Table 4.3-25 [3.42].

Table 4.3-25 Thermal expansion coeffcient, α and mechanical properties of invar alloys for practical use [3.42]

	Composition (wt%)	α at RT (10^{-6} K^{-1})	Vickers hardness	Tensile stress (MPa)
Invar	Fe−36Ni	<2	150–200	500–750
Super Invar [a]	Fe−32Ni−4Co	<0.5	150–200	500–800
Stainless Invar [b]	Fe−54Co−9Cr	<0.5		
High strength Invar	Fe−Ni−Mo−C [c]	<4		1250
	Fe−Ni−Co−Ti [d]	<4	300–400	1100–1400

[a] Masumoto, 1931
[b] Masumoto, 1934
[c] Yokota et al., 1982
[d] Yahagi et al., 1980

Table 4.3-26 Thermal expansion coeffcient of invar 36 and free-cut invar [3.17]

Temperature	α ($\times 10^{-6}$ K^{-1}) As annealed		As cold-drawn	
(°C)	Invar 36	Free-cut Invar 36	Invar 36	Free-cut Invar 36
25−100	11.18	1.60	0.655	0.89
25−200	1.72	2.91	0.956	1.62
25−300	4.92	5.99	2.73	3.33
25−350	6.60	7.56	3.67	4.20
25−400	7.82	8.88	4.34	4.93
25−450	8.82	9.80	4.90	5.45
25−500	9.72	10.66	5.40	5.92
25−600	11.35	12.00	6.31	6.67
25−700	12.70	12.90	7.06	7.17
25−800	13.45	13.60	7.48	7.56
25−900	13.85	14.60	7.70	8.12

Table 4.3-27 Some physical properties of invar alloys [3.17]

| Property	Value	
Melting point	1.425 °C	2600 °F
Density	8 g cm^{-3} (8.0–8.13)	500 lb ft^{-3}
Thermal electromotive force to copper (0–96 °C)	9.8 μV/K	
Specific resistance (Annealed)	82 × 10^{-6} Ω cm (81–88)	495 Ω circ. mil/ft
Temperature coefficient of electric resistivity	1.21 × 10^{-3} K^{-1}	0.67 × 10^{-3} °F^{-1}
Specific heat	0.123 cal/g K (25–100 °C)	0.123 Btu/lb °F (77–212 °F)
Thermal conductivity	0.0262 cal/sec cm K (22–100 °C)	72.6 Btu in./hr ft^2 °F (68–212 °F)
Curie temperature	277 °C (277–280 °C)	530 °F
Inflection temperature	191 °C	375 °F
Modulus of elasticity (in tension)	15.0 × 10^{10} Pa	21.4 × 10^6 lb in.$^{-2}$
Temperature coefficient of elastic modulus	+50 × 10^{-5} K^{-1} (16–50 °C)	+27 × 10^{-5} °F^{-1} (60–122 °F)
Modulus of rigidity	5.7 × 10^{10} Pa	8.1 × 10^6 lb in.$^{-2}$
Temperature coefficient of rigidity modulus	+58 × 10^{-5} K^{-1}	+30 × 10^{-5} °F^{-1}
Posson's ratio	0.290	
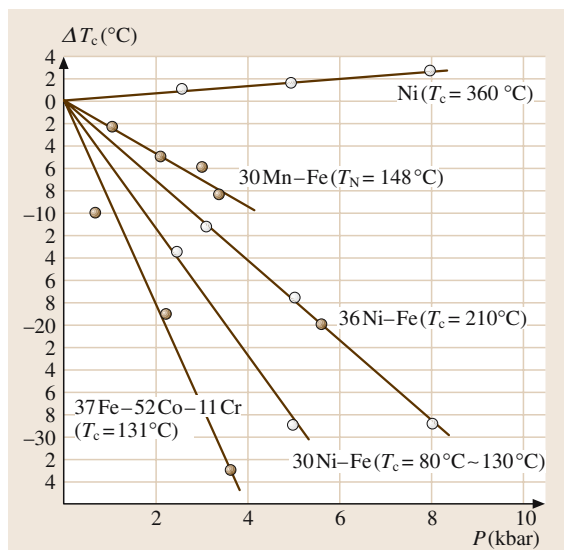
Fig. 4.3-39 The displacement of the Curie point ΔT_c vs. pressure in Fe−Ni invar alloys [3.43] and in Fe−Co−Cr invar alloy [3.44]. The results for Ni [3.43] and for a 30Mn−Fe alloy [3.44] are also shown for comparison. Numerical values in parentheses show the Curie or Néel point at atmospheric pressure

Invar-type alloys show large effects of pressure on magnetization and on the Curie temperature, which suggests a high sensitivity to the interatomic spacing, as shown in Fig. 4.3-39 [3.17].

Thermal expansion coefficients of invar 36 and free-cut invar 36 (containing S and P, or Se) between 25 and 900 °C are listed in Table 4.3-26 [3.17]. Some physical properties of Invar alloys are given in Table 4.3-27 [3.17].

Low thermal expansion coefficients are observed at ternary and quaternary Fe-alloy systems, too. The composition Fe–32 wt% Ni–4 wt% Co was the starting point of superinvar, whose TEC α is in the order of $10^{-7}\,\mathrm{K}^{-1}$. The thermal expansion curves of different variants are shown in Fig. 4.3-40 [3.17].

In order to improve the corrosion resistance of invar alloys, "stainless invar" was developed. The basic composition is Fe–54 wt% Co–9.5 wt% Cr. Stainless invar has the bcc structure at room temperature in the equilibrium state. As an invar material, it is used after quenching from a high temperature to retain the fcc structure [3.17].

To improve the mechanical properties two types of high strength invar materials were developed: a work-hardening type based on Fe−Ni−Mo−C, and
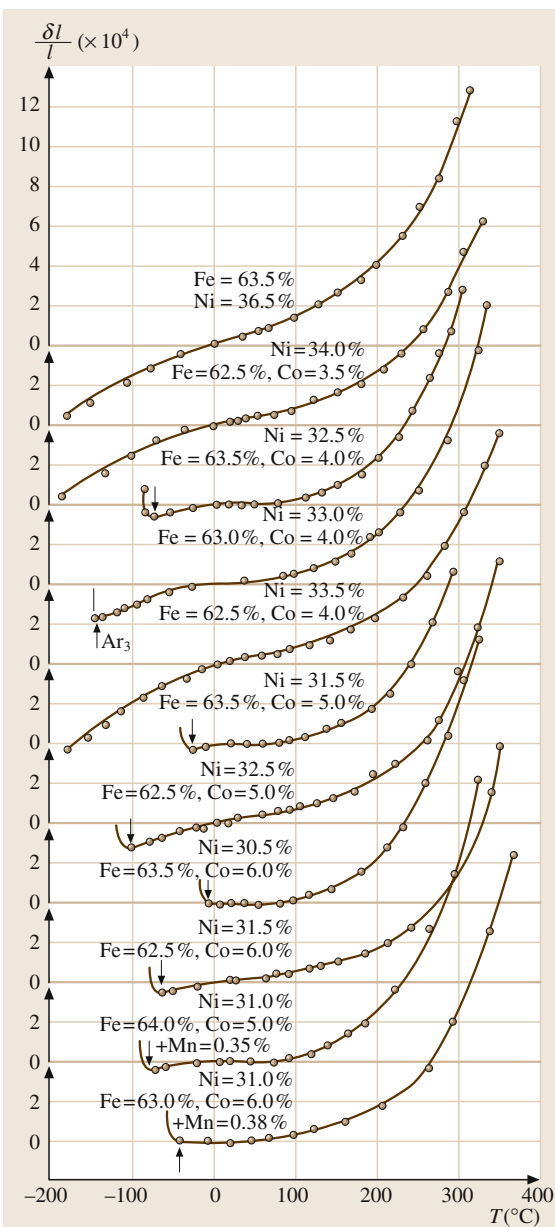

Fig. 4.3-40 Thermal expansion curves of super invar alloys [3.17]

a precipitation-hardening type Fe−Ni−Co−Ti alloy [3.17].

Fe−Pt−Based Invar Alloys. Among the ordered phases of the Fe−Pt system (Fig. 4.3-41 [3.17]), the Fe₃Pt phase shows the invar type thermal expansion anomaly. In
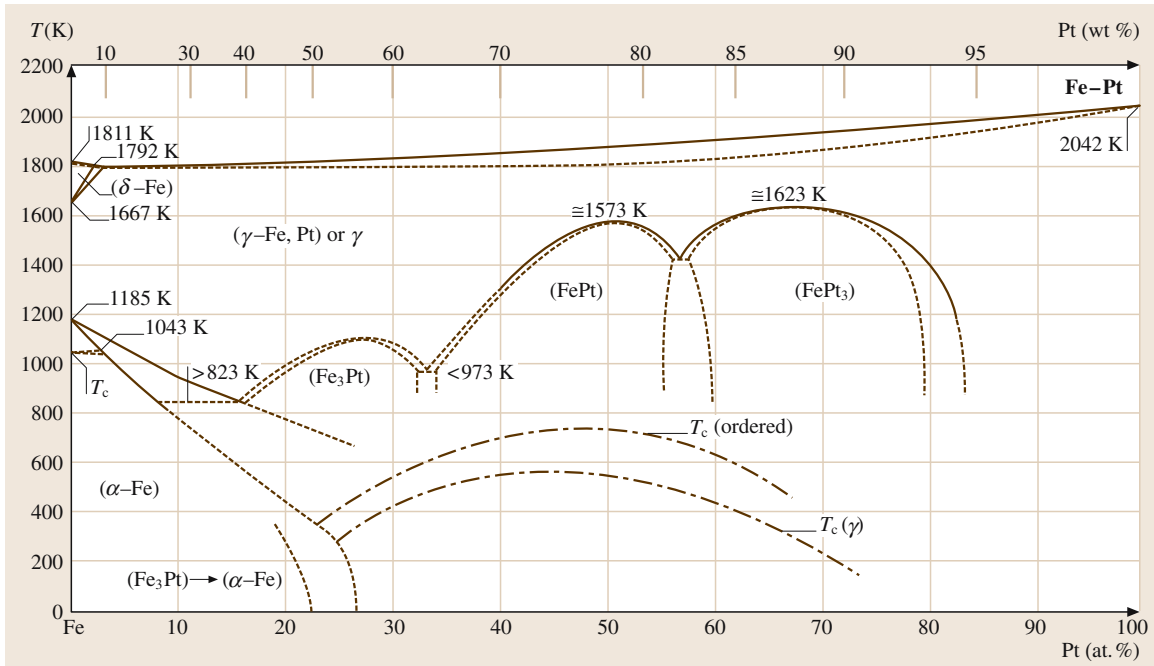
Fig. 4.3-41 Fe−Pt phase diagram. *Dashed-dotted lines*: Curie temperature T_c

order to obtain a well ordered state, a long annealing time is necessary (600 °C, 160 h). Disordered fcc alloys which show invar anomalies, too, may be obtained by rapid quenching from above the order–disorder transformation temperature. The Curie temperature of the disordered state is lower than that of the ordered state. A high negative value of α is observed just below the Curie temperature, particularly for disordered alloys. Annealed alloys containing 52 to 54 wt% Pt have small TEC and those containing 52.5 to 53.5 wt% Pt show negative values of α, Fig. 4.3-42 [3.17].

Fe−Pd-Based Invar Alloys. Alloys of Fe−Pd (see Fig. 4.3-43) containing 28 to 31 at.% Pd show invar characteristics, as seen in Fig. 4.3-44 [3.41]. In order to obtain invar behavior, the alloys are quenched from the high temperature γ phase field such that phase transformations at lower temperatures are suppressed. As shown in Fig. 4.3-45 [3.41], the thermal expansion is strongly decreased by cold deformation, i.e., by disordering, lattice defects, and internal stresses. After cold working, an instability of the invar property is observed.

Part 4 | 3.2

Fig. 4.3–42 Thermal expansivity curves of Fe−Pt alloys [3.17]

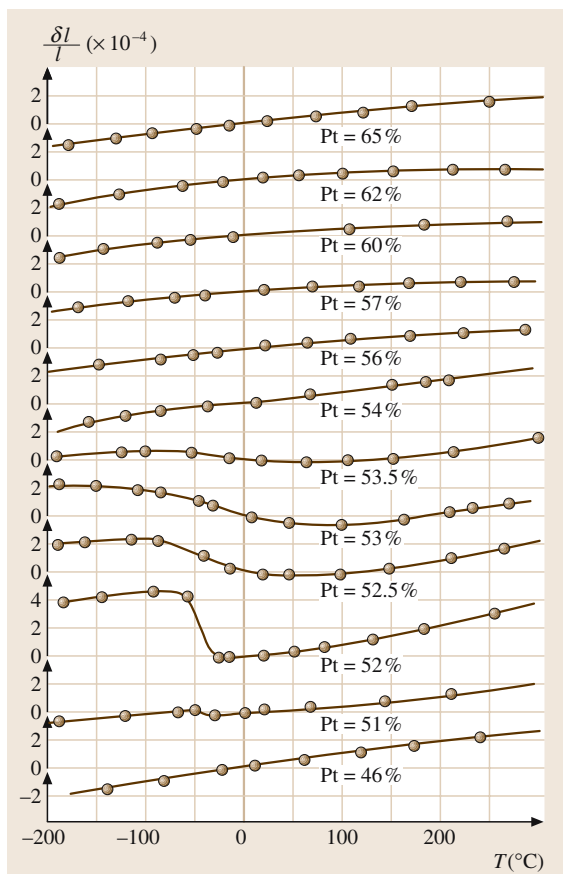*Other Alloy Systems with Invar Behavior.* Beyond the invar-type alloys mentioned, many other Fe-based alloy systems show invar behavior, for instance, Fe−Ni−Cr, Fe−Ni−V, Fe−Pt−Re, Fe−Ni−Pt, Fe−Ni−Pd, Fe−Pt−Ir, Fe−Cu−Ni, and Fe−Mn−Ni. Some amorphous melt/quenched alloy systems show invar characteristics too, e.g., $Fe_{83}B_{17}$, $Fe_{85}P_{15}$, $Fe_{79}Si_9B_{12}$. Similarly, amorphous alloys prepared by sputtering show invar characteristics: $Fe_{75}Zr_{25}$, $Fe_{72}Hf_{28}$. Some antiferromagnetic Mn- and Cr-based alloys also exhibit a remarkable anomaly of thermal expansion due to magnetic ordering: $Pd_{64.5}Mn_{35.5}$, $Mn_{77}Ge_{23}$, $Cr_{92.5}Fe_{4.3}Mn_{0.5}$, $Cr_{96.5}Si_3Mn_{0.5}$.

Elinvar Alloys

Elinvar or constant-elastic-modulus alloys are based on work by *Guillaume* [3.45] and *Chevenard* [3.46]. They show a nearly temperature-independent behavior of the Young's modulus (E). For technical applications, elinvar alloys are designed to show the anomaly in the range of their operating temperature, usually close to room temperature. Since the resonance frequency f_0 of an oscillating body is related to its E modulus by $f_0 \sim \sqrt{E/\varrho}$ ($\varrho =$density), the thermoelastic properties of elinvar alloys are utilized for components in oscillating systems of the precision instrument industry. In these applications highly constant resonance frequencies are required. Typical examples are: resonators in magnetomechanical filters; balance springs in watches, tuning forks; helical springs in spring balances or seismographs, as well as in pressure or load cells. The condition for temperature compensation of the Young's modulus E is:

$$2\Delta f / f \Delta T = \Delta E / E \Delta T + \alpha \approx 0 \,,$$

with $T =$ temperature and $\alpha =$ linear thermal expansion coefficient. Elinvar characteristics also refer to the temperature independence of the shear modulus G, which is related to the E modulus via

$$3/E = 1/G + 1/3B$$

and

$$E = 2(1 + \nu)G = 3(1 - \nu)B \,,$$

with $B =$ bulk modulus and $\nu =$ Poisson's ratio.

In ordinary metallic materials, E decreases with increasing temperature according to the variation of the elastic constants with temperature according to the anharmonicity in the phonon energy term. The temperature compensation of the E-modulus in ferromagnetic and antiferromagnetic elinvar alloys is caused by an anomaly in its temperature behavior (ΔE effect). As a consequence in ferromagnetic alloys, the E modulus in the demagnetized state is different from that in the magnetized state. The ΔE effect with ferromagnetic elinvar alloys consists of three parts [3.47]:

$$\Delta E = \Delta E_\lambda + \Delta E_\omega + \Delta E_A \,.$$

A schematic description of the components of the ΔE effect in ferromagnetic elinvar alloys is given in Fig. 4.3-46.
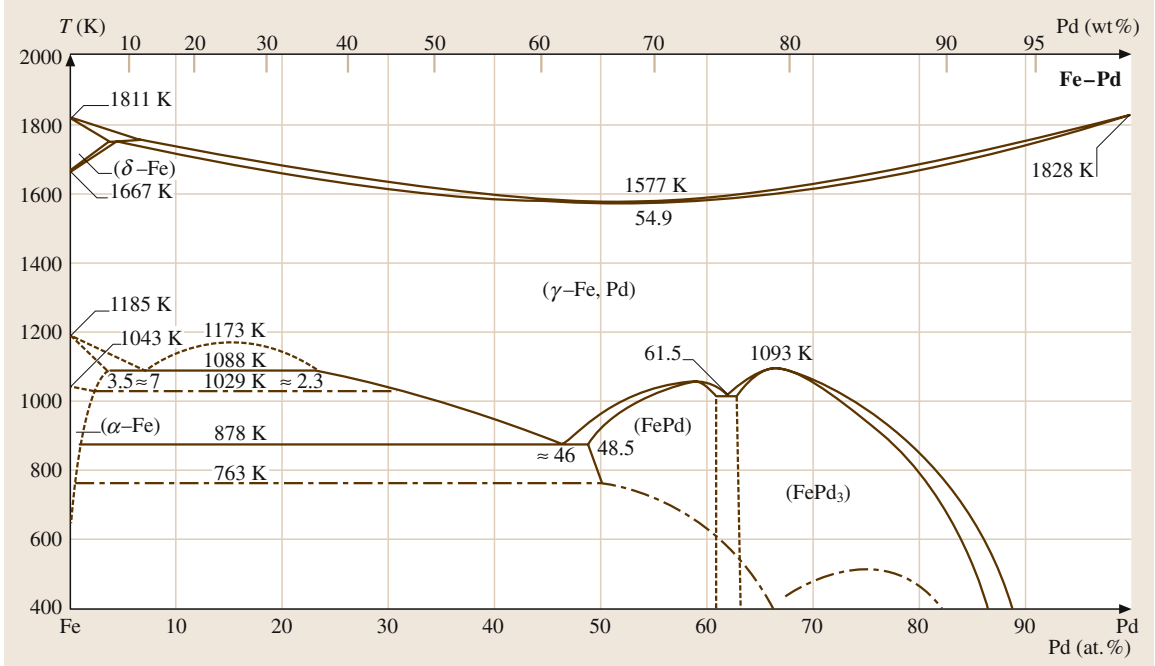
Fig. 4.3-43 Fe−Pd phase diagram. *Dashed-dotted lines*: Curie temperature T_c
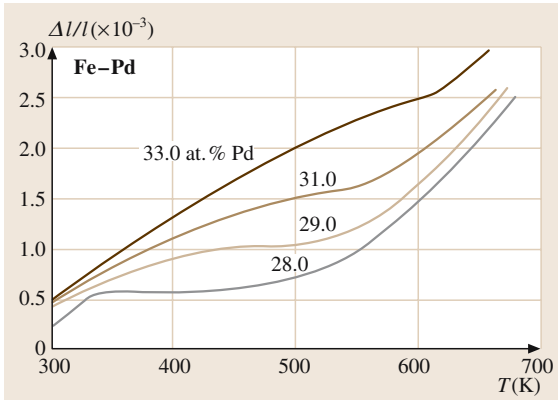
Fig. 4.3-44 Thermal expansion curves of Fe−Pd alloys rapidly cooled from high temperature [3.41]
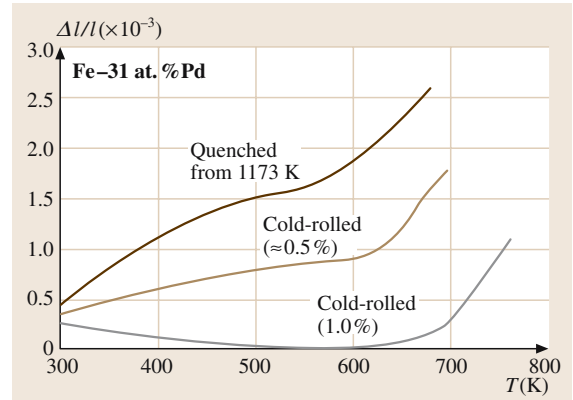
Fig. 4.3-45 Thermal expansion curves of cold-worked Fe–31 at.% Pd alloy. The rolling ratio is given by percentage

These components are attributable to the following relations:

$$\Delta E_\lambda = -2/5 E^2 \lambda_s / \sigma_i \,,$$

where ΔE_λ is attributed to the shape magnetostriction (λ_s) that changes the direction of the spontaneous magnetization, owing to domain wall motion and rotation processes as a consequence of the influence of mechanical stresses (σ_i) or magnetic fields on the unsat-

urated state of material [3.48]. The value ΔE_ω is caused by forced volume magnetostriction (ω) as a consequence of changes of the interatomic distances induced by stress or very high magnetic fields, which lead to a change of the magnetic interaction [3.49]:

$$\Delta E_\omega = -1/9 E^2 [(\partial \omega / \partial H)^2 / \partial J / \partial H] \,,$$

where $\partial \omega / \partial H =$ forced volume magnetostriction and $\partial J / \partial H =$ para-susceptibility. The value ΔE_A takes the
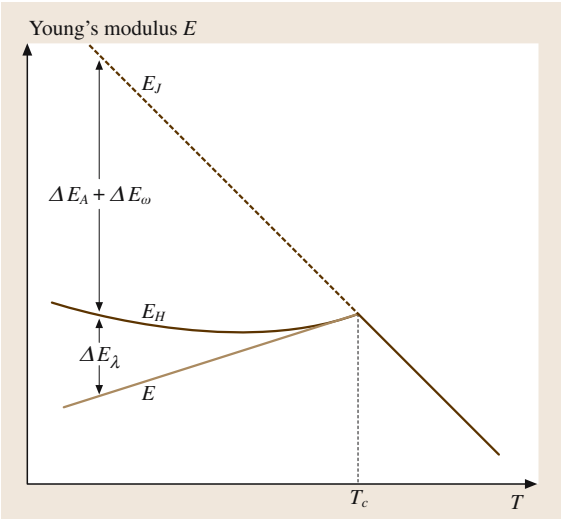
Fig. 4.3-46 Young's modulus E as a function of temperature of ferromagnetic elinvar alloys: $E = E$ modulus in the absence of a magnetic field, $E_H = E$ modulus measured in a magnetic field H, $E_J = E$ modulus at constant polarization J

Fig. 4.3-47 E modulus and its dependence on the temperature of an annealed Fe–39 wt% Ni alloy, with and without influence of a magnetic field H [3.51]

role of the exchange energy into account [3.50]:

$$\Delta E_A \sim -\omega_s \sim J_s^2 \,,$$

where ω_s = volume magnetostriction and J_s = saturation polarization. It originates from the spontaneous volume magnetostriction ω_s as a function of the change of exchange energy with temperature due to the variation of magnetic ordering up to the Curie temperature.

Ferromagnetic Elinvar Alloys. The development of ferromagnetic elinvar alloys is based on affecting the shape magnetostriction λ_s by control of internal stresses resulting from deformation and/or precipitation hardening. But this requires a zero or negative temperature coefficient of the E_H modulus. Based on an Fe–39 wt% Ni alloy, it can be shown how this behavior is achievable. Alloys of Fe–Ni with 36 to 45 wt% Ni have a positive sign of the temperature coefficient of the E_H modulus (see Fig. 4.3-47 [3.51]).

By addition of 7 wt% Cr this coefficient is reduced to zero or to slightly negative values. By a deformation it can be influenced furthermore while the absolute value

Fig. 4.3-48 Young's modulus E of an Fe−39Ni−7Cr−0.8Be−1.0Ti (wt%) alloy as a function of temperature, degree of cold deformation η (%) with and without a magnetic field H [3.51]

and 1.0 wt% Ti on the $E = f(T)$ characteristic. Cold deformation causes the Curie temperature to rise.

The final processing steps consist of solution annealing at 1150 °C, water quenching, cold deformation, and a final precipitation annealing at about 600 °C. Accordingly commercial elinvar alloys are produced, such as those listed in Tables 4.3-28, 4.3-29, and 4.3-30.

Apart from the well-tried Fe−Ni−Cr−(Be, Ti)-based elinvar-type alloys, Fe−Ni−Mo-based alloys have gained technical application. Addition of Mo improves the elastic properties, lowe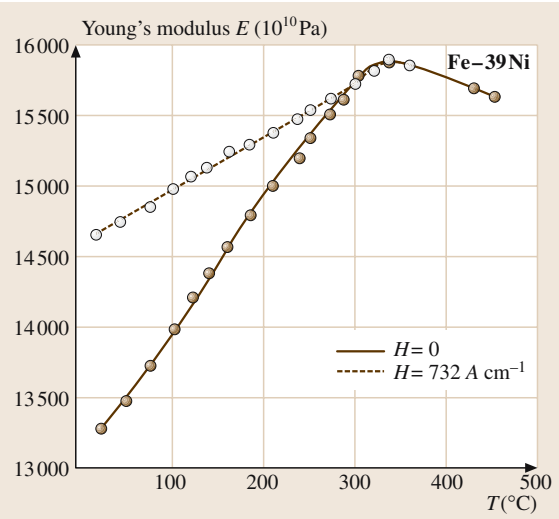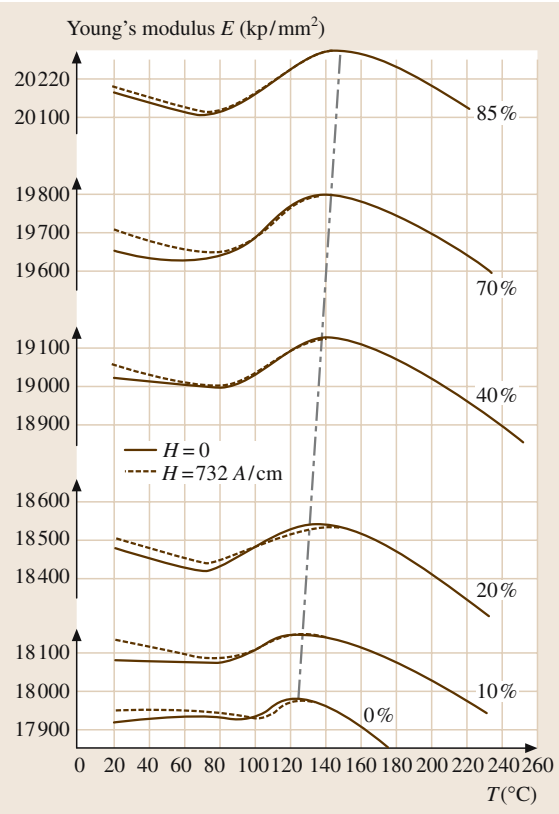rs the Curie temperature, and increases the resistance to corrosion. While in Europe and the USA, Fe−Ni-based elinvar-type alloys mainly were developed, in Japan Co−Fe-based elinvar alloys were discovered. Ternary Co−Fe−Cr alloys and quaternary alloys containing Ni (Co-elinvar) attained significant technical relevance. Distinguishing

marks worth mentioning include: higher Young's modulus than Fe−Ni-based alloys, corrosion resistance, wide range of temperature compensating of E modulus, and easy hardening by cold-working.

Antiferromagnetic Elinvar Alloys. In antiferromagnetic alloys no domains are formed and no ΔE_λ effect occurs. With antiferromagnetic ordering the ΔE_A effect can only be exploited in combination with a pronounced cubic to tetragonal lattice distortion associated with antiferromagnetic ordering. This requires methods to develop temperature compensating elastic behavior which are different from those for ferromagnetic thermoelastic materials. The development of antiferromagnetic alloys with Elinvar properties has been concentrated on Mn−Cu, Mn−Ni, and Fe−Mn base alloys. In [3.52] the distinct anomalies of Young's modulus at the Néel

Table 4.3-28 Compositions in (wt%) of Fe−Ni-based elinvar alloys [3.17]

| | Bal. Fe | | | | | | | | | | | | | | | |
	C	Ni	Cr	Ti	Mo	W	Mn	Si	Al	Be	Nb	Cu	V	Co	P	S
Durinal	0.1	42		2.1			2		2							
Elinvar Extra	0.04	43	5	2.75			0.6	0.5	0.3					0.35		
	0.6	42	5.5	2.5			0.5	0.5	0.6							
Elinvar New	1	35	5			2	1									
Elinvar Original		36	12													
	0.5−2	33−35	21−5			1−3	0.5−2	0.5−2								
	0.71	33.5	8.4			2.98	2.4	0.33							0.018	0.01
Iso-elastic		36	8		0.5	(other small constituents)										
	0.1	36	7.5		0.5		0.6	0.5				0.2				
Isoval	0.6	30			2.2	3.2	0.15	0.2			3.8		4.2			
Métélinvar	0.6	40	6		1.5	3	2									
Ni-Span C	0.03	42.2	5.3	2.5			0.4	0.4	0.4			0.05			<0.04	<0.04
Ni-Span C 902	<0.06	42	5.2	2.3			<0.8	<0.1	0.5							
Nivarox CT	0.02	37	8	1			0.8	0.2		0.8						
Nivarox CTC	0.2	38	8	1						1						
Nivarox M	0.03	31			6		0.7	0.1		0.7						
Nivarox M30		30			9					1						
Nivarox M40		40			9					1						
Nivarox W		36		1						1						
Sumi-Span 1		36	9													
Sumi-Span 2	0.4	38	11													
Sumi-Span 3		42.5	5.5	2.4												
Thermelast 4009		40			9					0.5						
Thermelast 5409		40			9					0.5						
Vibralloy		39			9											
		40			10											
YNiC	0.03	41−43	5.1−5.5	2.2−3					0.5−0.6							

Part 4 | 3.2

Table 4.3-29 Fe−Ni-based commercial elinvar-type alloys and the corresponding values of: density d, melting point T_m, Curie temperature T_c, electrical resistivity ρ, thermal expansion coefficient α, Young's modulus E, its temperature coefficient e, and shear modulus G [3.17]

	d (g cm^{-3})	T_m (°C)	T_c (°C)	ρ ($\mu\Omega$ cm)	α (10^{-6} K^{-1})	E (10^{10} Pa)	e (10^{-5} K^{-1})	G (10^{10} Pa)
Durinal			90				−1.0–1.0	
Elinvar		1420–1450	−100		8	7.8–8.3	−0.3–0.3	
Elinvar Extra [a]	8.15				6.5	18.9	0	6.9
Iso-elastic				88	6.7	18.0	−3.3–2.5	6.4
Métélinvar			260, 295				0	
Ni-Span C	8.15	1450–1480		80	7.1	18.9	−1.7–1.7	
Ni-Span C 902 [a]	8.14	1460–1480	160–190	100–120	8.1	17.7–19.6		6.9–7.4
Nivarox CT	8.3		80	97	7.5	18.6	−2.5–2.5	
Sumi-Span 1	8.15		−140	100	−10	18.1	0–2.5	
Sumi-Span 2	8.08		−190	105	−10	18.1	−1.5–0 [b]	
Sumi-Span 3 [a]	8.05		−190	110	≈8	19.2	−1.0–1.0	7.8
Thermelast 4002 [a]	8.3			100	8.5	18.6		6.4
Thermelast 4005 [a]	8.3			100	8.3	17.2		6.4
Thermelast 5405 [a]	8.3			100	8.0	18.6		6.4
Thermelast 5429 [a]	8.3			100	8.0	18.6		6.4
Vibralloy [a]	8.3		300		8	17.4	0	
YNiC	8.15		90–180		8.1	19.6	−1.8–1.5	6.5–6.8

[a] Properties in the fully aged state
[b] Temperature coefficient of the frenquency of proper vibration

Table 4.3-30 Co−Fe-based elinvar-type alloys (annealed state). Composition, thermal expansion coefficient α, Young's modulus E and shear modulus G, and their respective temperature coefficients, e and g [3.17]

	Composition in wt%								α [a] (10^{-6} K^{-1})	E [b] (10^{10} Pa)	e [c] (10^{-5} K^{-1})	G [b] (10^{10} Pa)	g [c] (10^{-5} K^{-1})
	Co	Fe	Cr	V	Mo	W	Mn	Ni					
Co-elinvar	60.0	30.0	10.0						5.1	17.07		6.91	−0.2
	51.5	38.5	10.0						8.7	18.84	−1.0	7.55	
	47.3	34.5	9.1					9.1	7.8			6.61	0.2
	27.7	39.2	10.0					23.1	8.1			6.48	−0.3
	26.7	50.8	5.8					16.7	7.8			4.99	0.3
	17.9	42.8	10.7					28.6	8.3			6.74	0.9
Elcolloy	40.0	35.0	5.0			5.0		15.0	5.0				−0.2
	35.0	36.0	5.0		4.0	4.0		16.0	9.0				0.5
Mangelinvar	38.0	37.0					15.0	10.0	9.7	18.0	−1.0		
Moelinvar	50.0	32.5			17.5				9.6			7.36	−0.2
	45.0	35.0			10.0			10.0	8.5			6.15	0.7
	20.0	40.0			20.0			20.0	8.4			7.70	0.9
	10.0	45.0			15.0			30.0	9.8			7.85	−0.4
Tungelinvar	50.0	28.5				21.5			7.4			6.45	−0.7
	39.0	32.0				19.0		10.0	7.8			8.13	0.4

Table 4.3-30 Co−Fe-based elinvar-type alloys (annealed state). Composition, thermal expansion coefficient α, cont.
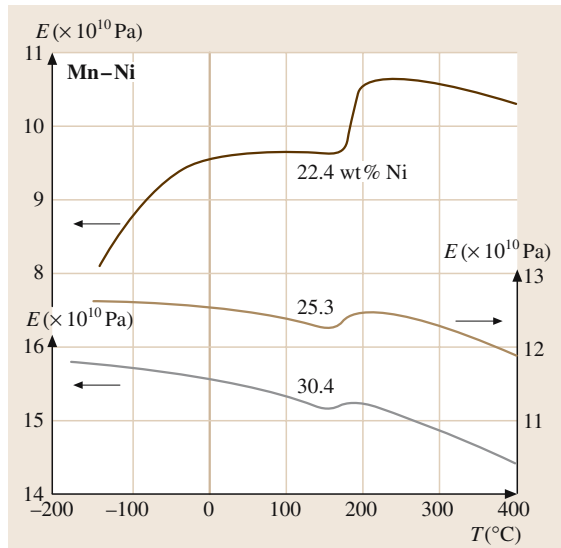
	Composition in wt%								α^a $(10^{-6}\,K^{-1})$	E^b $(10^{10}\,Pa)$	e^c $(10^{-5}\,K^{-1})$	G^b $(10^{10}\,Pa)$	g^c $(10^{-5}\,K^{-1})$
	Co	Fe	Cr	V	Mo	W	Mn	Ni					
Velinvar	60.0	30.0		10.0					8.1			6.53	0.0
	50.0	31.8		8.2				9.1	11.0			6.70	1.0
	37.5	35.5		7.0				20.0	11.1			6.45	−0.6
	22.5	43.5		4.0				30.0	12.3			5.66	−0.3

^{a} For the temperature range 10−50 °C
^{b} At 20 °C
^{c} For the temperature range 0−50 °C

temperature of Mn−Ni- and Mn−Cu-based alloys were modified by additions of Cr, Fe, Ni, Mo, and W as well as by suitable technological treatment in such a way that useful thermoelastic coefficients could be reached. However, the mechanical workability, the sensitivity of elastic properties to the degree of cold-working, the unsufficient spring properties as well the low corrosion resistance and high mechanical damping could not satisfy the conditions of technical application. Figures 4.3-49 and 4.3-50 [3.17] indicate the temperature dependence of E of some Mn−Ni- and Mn−Cu-based alloys. Table 4.3-31 [3.17] lists the compositions and the thermoelastic and mechanical properties of this group of alloys.

By optimization of the chemical composition and the processing technology, an Fe−24Mn−8Cr−7Ni−0.8Be
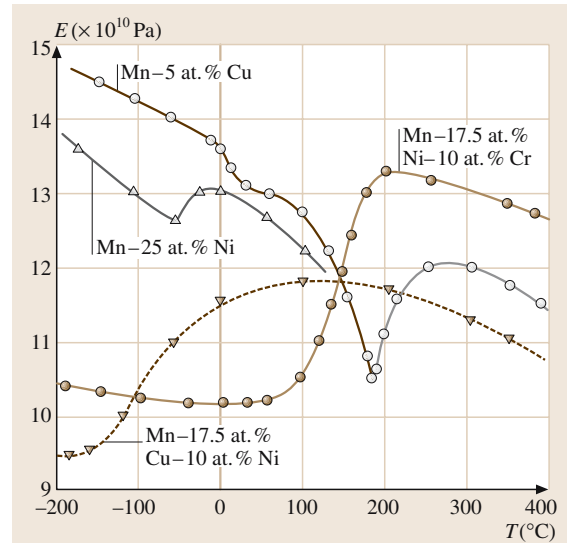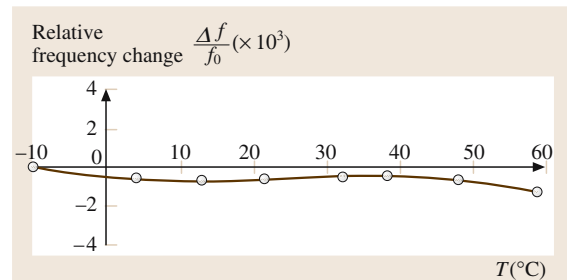
Fig. 4.3-50 Temperature dependence of Young's modulus E [3.17] for various Mn-based alloys annealed at 1223 K for 1 h and then quenched

Fig. 4.3-49 Mn−Ni binary alloys. Young's modulus E vs. temperature for alloys annealed at 1223 K for 1 h after cold-working [3.17]

Fig. 4.3-51 Temperature dependence of the frequency of a screw spring [3.53]

Table 4.3-31 Nonferromagnetic Mn-based elinvar-type alloys. Composition, thermal expansion coefficient α, Young's modulus E and shear modulus G, and their respective temperature coefficients, e and g and hardness HV [3.17]

| Composition in wt% | | | | | | | | | α^{a} $(10^{-6}\,\mathrm{K}^{-1})$ | E $(10^{10}\,\mathrm{Pa})$ | e^{a} $(10^{-5}\,\mathrm{K}^{-1})$ | G $(10^{10}\,\mathrm{Pa})$ | g^{a} $(10^{-5}\,\mathrm{K}^{-1})$ | HV |
Mn	Cu	Ni	Cr	Fe	Co	Mo	W	Ge						
87		10	3						23.7	12.3	1.25	5.18	1.05	121
82		15					3		23.0	12.1	0.55	5.07	0.78	149
80		16		4					21.1	12.2	−0.13	4.63	−0.75	150
80		9				11			20.3	11.9	0.05	5.00	1.10	380
80								20	12.3	9.0	1.5			255
79		21								9.8	−2.5	3.60	−2.7	235
67	20	13							22.4	14.4	0.21	4.55	0.29	125
59		16	25						21.6	16.2	0.85	5.21	0.83	250
49	41		10						22.4	13.5	−0.97	5.53	−0.20	250
44	55		1						22.1	13.2	0.11	5.03	0.08	145
43	57								23.6	11.2	0.3	4.2	−0.9	131
43	55			2					22.9	8.50	−1.11	4.02	−2.57	135
42	55				3				23.0	15.2	2.30	6.77	1.88	149
39	56						5		23.2	12.0	−0.25	5.05	−0.56	140

^{a} For the temperature range 0–40 °C

^{b} At 20 °C

Table 4.3-32 Properties of an antiferromagnetic Fe−24Mn−8Cr−7Ni−0.8Be elinvar alloy [3.53]

Property	Value
Young's modulus E	165–195 GPa
Thermoelastic coefficient TKE	$(1-10)\,\mathrm{MK}^{-1}$
Compensation range of E	0–50 °C
Shear modulus G	74–82 GPa
Coefficient of thermal expansion α (20–100 °C)	$13\,\mathrm{MK}^{-1}$
Tensile strength σ_{B}	1200–1800 MPa
Yield point σ_{s}	1100–1650 MPa
Elongation δ	12–2 %
Vicker's Hardness HV 10	420–540 HV
Quality factor Q	20 000–10 000
Specific electrical resistance ρ	$80\,\mu\Omega\,\mathrm{cm}$
Density γ	$7.6\,\mathrm{g\,cm}^{-3}$
Electrochemical breakdown potential ϵ_{D}	−0.25 V
Melting temperature T_{s}	1450–1480 °C

antiferromagnetic elinvar alloy was developed which fulfills the complex requirements for an antiferromagnetic, corrosion resistant, temperature compensating thermoelastic spring material for applications near room temperature, Fig. 4.3-51 [3.53]. The thermoelas-tic, mechanical and physical properties are summarized in Table 4.3-32 [3.53].

Other Nonmagnetic Elinvar–Type Alloys. In general, the elastic constants decrease with increasing tem-
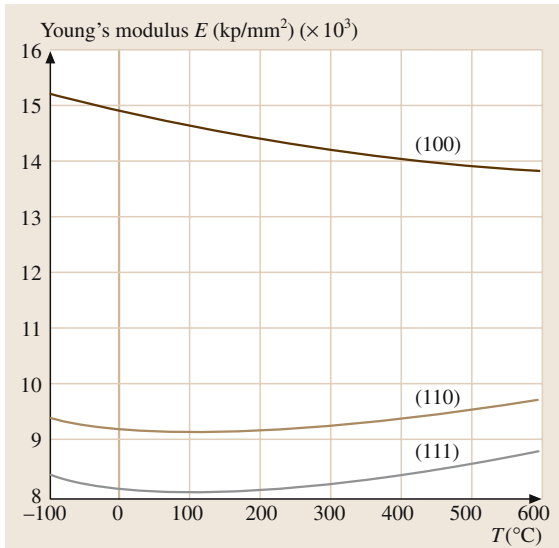
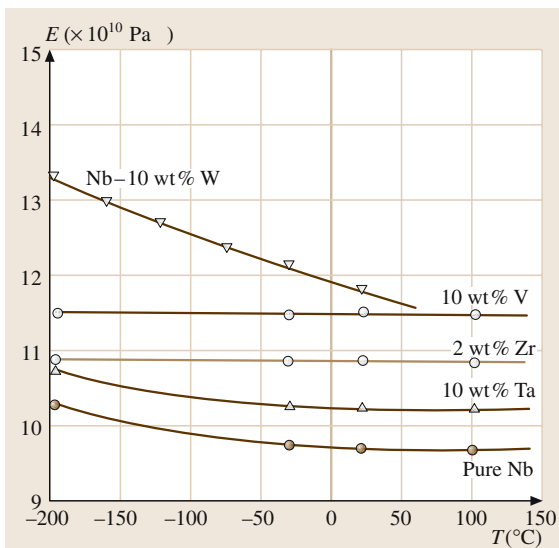**Fig. 4.3-52** Thermoelastic behavior of single crystalline Nb in the major lattice directions [3.54]

perature. The temperature dependence of the elastic properties of Nb shows highly anisotropic anomalies (see Fig. 4.3-52) [3.54]. In a randomly oriented polycrystal, Nb becomes an elinvar-type material, Fig. 4.3-53 [3.41]. This plot of Young's modulus vs. temperature also shows the influence of alloying elements.

Elinvar behavior is, also, found in concentrated Nb−Zr and Nb−Ti alloys. Furthermore, some amorphous alloys, e.g., in the Fe−B-, Fe−P-, and Fe−Si−B-based systems, show elinvar behavior. Examples for amorphous Fe−B alloys are shown in Fig. 4.3-54.

Fig. 4.3-53 Young's modulus E vs. temperature. Samples annealed at 1400 °C for 4 h [3.41] of pure Nb and Nb-based binary alloys
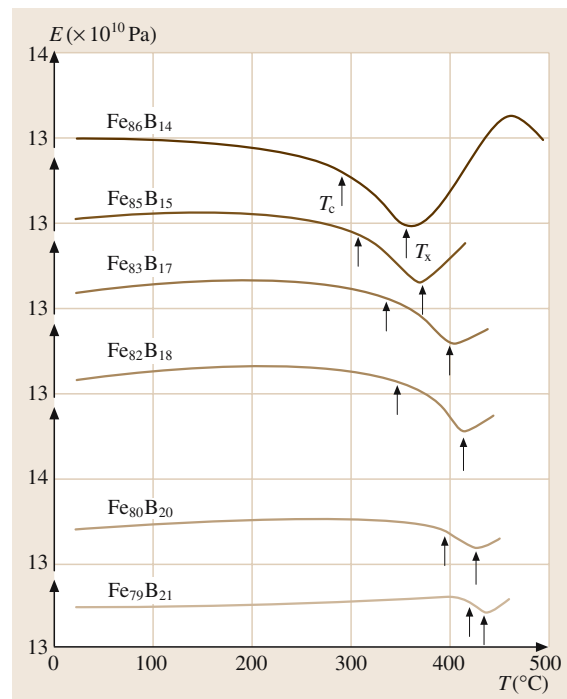

Fig. 4.3-54 Fe−B alloys. Temperature dependence of Young's modulus E for amorphous alloys annealed at 200 °C for 2 h. T_x and T_c show the crystallization and the Curie temperature, respectively [3.41]

4.3.3 Hard Magnetic Alloys

Permanent or hard magnetic materials comprise traditionally some special steels but consist essentially of multiphase alloys and intermetallic and ceramic compounds today. Relatively few magnetic alloys and compounds fulfill the requirement of combining high magnetic efficiency and competitive cost: Fe−Ni−Al−Co (Alnico), Fe−Cr−Co, Mn−Al−C, hard ferrites, and rare-earth transition metal compounds of the Co−Sm, Fe−Nd−B and Fe−Sm−N alloy systems. Surveys may be found in handbooks [3.1, 3, 55] and data collections [3.10, 56]. A survey of permanent magnetic materials is given in Table 4.3-33. The metallic hard magnets are treated in this chapter, the oxidic hard magnetic materials are dealt with in Sect. 4.3.4.

All of the hard magnetic materials are based on choosing a base alloy with a sufficiently high saturation magnetization M_s and a high magnetocrystalline anisotropy constant K_1, and tailoring the microstructure to exploit this crystal anisotropy. In some cases, shape anisotropy is generated in addition. This microstructural control is achieved by

1. Inducing a texture by processing in such a way that a macroscopic direction in the material, e.g., the rolling direction of a sheet or the pressing direction in a sintered material, is an easy direction, and processing at 90°, i.e., the transverse direction, is a hard direction for magnetization. This is the basic magnetic hardening mechanism of hard magnetic steels which have lost their importance in present technology; but it is the basis of producing the more recent high energy magnets made from intermetallic compounds such as Co_5Sm and ferrites.

2. Inducing a two-phase microstructure by coherent precipitation or decomposition and promoting, by suitable magnetic field annealing procedures, the alignment of the elongated precipitates in one direction of easy magnetization, i.e., inducing both

Table 4.3-33 Survey commercially used permanent magnetic materials. Survey

Material	Fe, Co content (wt%)	B_r [a] (T)	$_JH_c$ (kA m^{-1})	$(BH)_{max}$ (kJ m^{-3})	appr. T_c (°C)	T_{max} [b] (°C)	Process [c]
Dense magnets							
3.5Cr steel	94−95	0.95	5	2.3	745		C [d]
6W steel	92−93	0.95	6	2.6	760		C
36Co steel	90−91	0.95	19	7.4	890		C
Alnico	67−74	0.52−1.4	40−135	13−69	810−900	450−550	C, P [d]
Fe−Cr−Co	65−73	1.1−1.4	40−65	25−55	670	500	C
hard ferrite	58−63	0.37−0.45	160−400	26−40	460	250	P
Pt-Co	23.3	0.64	430	73	480	350	C, P
MnAlC	−	0.55	250	44	500	300	P
Co_5Sm	63−65	0.85−1	>1600	140−200	730	250	P
$TM_{17}Sm_2$	61−68	0.95−1.15	480−2000	190−220	810	330−550	P
Fe−Nd−B	66−72	1.05−1.5	950−2700	240−400	320	60−180	P
Bonded magnets							
hard ferrite	58−63	0.1−0.31	180−300	2−18		140	P
$TM_{17}Sm_2$	61−68			70−120		150	P
$Fe_{14}Nd_2B$	70−72	0.47−0.69	600−1200	35−80		80−110	P
$Fe_{17}Sm_2N_3$		0.77	650	105		100	P

[a] B_r values are for magnets operated at load lines $B/H \gg 1$

[b] The maximum operating temperature of bonded magnets is determined by the organic binder used

[c] Magnets are manufactured either by a casting/heat treatment technique or by a powder metallurgical process. Powder metallurgy is applied for small magnets where small and intricate shapes to precise tolerances are required

[d] C: magnets produced by cast and heat treatment; P: magnets produced by means of powder metallurgical techniques

magnetocrystalline and shape anisotropy. This is termed magnetic shape anisotropy and is employed in the Alnico and Fe−Co−Cr hard magnetic materials.

3. Inducing a fine grained microstructure with a magnetically insulating phase at the grain boundaries so that the grains are magnetically decoupled and, as a consequence, the nucleation of reverse magnetization is requiring an extremely high nucleation energy. This is applied, for example, to $TM_{17}Sm_2$, $Fe_{14}Nd_2B$ and bonded magnets.

In some of the hard magnetic materials two of these variants of microstructural design are combined.

4.3.3.1 Fe−Co−Cr

Hard magnetic materials made of ternary Fe−Co−Cr alloys are based on the high atomic moment of Fe−Co alloys and the miscibility gap occurring when Cr is added. Intrinsic magnetic properties are compiled in [3.6]. Extensive magnetic materials data are found in [3.56]. Figure 4.3-55 shows the relevant metastable phase relations in the ternary equilibrium diagram. If an alloy is homogenized in the solid solution range above the solvus surface with $T_{max} > 700\,°C$ first and annealed in the miscibility gap subsequently, coherent decomposition occurs, which results in a two-phase microstructure on the nanometer scale. The α_1 phase is rich in Fe and Co and ferromagnetic while the α_2 phase is rich in Cr and antiferromagnetic. This two-phase microstructure on the nm scale has hard magnetic properties which can be varied by adjusting the alloy composition and heat treatment. The term spinodal decomposition is frequently applied to all kinds of coherent decomposition, e.g., in [3.56]. But it is used correctly only if referring to a special mode of compositional evolution associated with particular kinetics in the initial stage of decomposition within the spinodal of a miscibility gap.

Three groups of materials have been developed, differing essentially in the Co content (< 5, 10–15, 23–25 wt% Co), while the Cr content ranges from 22 to 40 wt% Cr. Table 4.3-34 lists data obtained by varying composition, mode of manufacturing, and heat treatment systematically for the group characterized by < 5 wt% Co as an example. The variation of the magnetic properties is determined by the intrinsic properties of the decomposed phases α_1 and α_2 and their microstructural array.
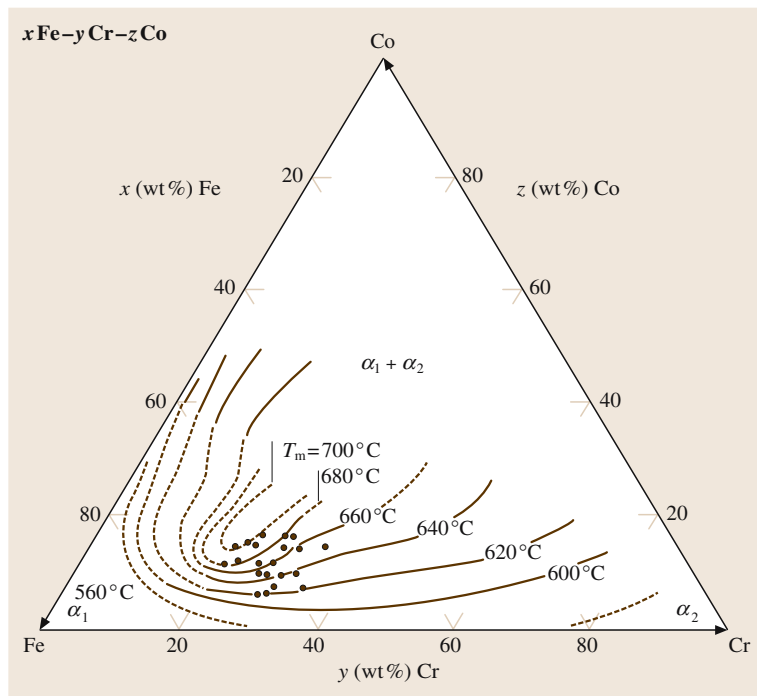

Fig. 4.3-55 The miscibility gap $(\alpha_1 + \alpha_2)$ of the bcc α-phase in the Fe−Co−Cr phase diagram [3.56]

Table 4.3-34 Survey of magnetic properties of Fe−Cr−Co (≤ 5 wt% Co) alloys in relation to the composition, mode of manufacturing and heat treatment [3.56]

Alloy components (wt%)			Mode of manufacturing and heat treatment	Magnetic properties					
				B_r		$_B H_c$		$(BH)_{max}$	
Cr	Co	others		(T)	(kG)	(kA m^{-1})	(kOe)	kJ m^{-3}	(MGOe)
33	2	1 Hf	H(700, 15):MCL $> T_s$, R, 500):FCL	1.25	12.5	16.2	0.203	14.0	1.76
32	3		As above	1.29	12.9	35.9	0.449	32.4	4.08
32	4	0.5 Ti	As above	1.26	12.6	42.7	0.534	40.1	5.06
28	5		As above	1.38	13.8	29.0	0.362	27.9	3.52
30	5		As above	1.34	13.4	42.2	0.528	42.1	5.31
33	5		As above	1.22	12.2	40.8	0.51	36.3	4.58
35	5		As above	1.15	11.5	37.0	0.462	29.3	3.69
30	5	0.1 B	As above	1.31	13.1	42.0	0.525	40.2	5.07
30	5	0.25 B	As above	1.29	12.9	39.8	0.498	34.8	4.39
30	5	0.1 C	As above	1.31	13.1	42.2	0.527	38.8	4.89
30	5	0.8 Ge	As above	1.32	13.2	24.8	0.31	39.1	4.93
30	5	0.25 Ti	As above	1.34	13.4	27.2	0.34	40.2	5.07
30	5	0.5 Ti	As above	1.30	13.0	41.4	0.518	40.1	5.06
30	5	1.5 Ti	As above	1.27	12.7	40.8	0.51	38.1	4.81
30	5	0.25 Hf	As above	1.32	13.2	43.0	0.537	41.2	5.2
30	5	0.5 Hf	As above	1.29	12.9	43.9	0.549	41.4	5.22
30	5	1 Hf	As above	1.30	13.0	43.0	0.537	40.4	5.1
30	5	3 Hf	As above	1.24	12.4	41.5	0.519	34.8	4.39
23	2	1 Hf	MCL($> T_s$, 550): CCL (550, 500)	1.24	12.4	36.8	0.46	34.1	4.3
32	3		As above	1.25	12.5	40.0	0.5	34.1	4.3
30	5		As above	1.34	13.4	42.4	0.53	42.0	5.3
32	4	0.5 Ti	As above	1.26	12.6	42.8	0.535	40.4	5.1
28	5	4 Ni	As above	1.27	12.7	29.6	0.37	30.1	3.8
28	7		As above	1.25	12.5	40.8	0.51	41.2	5.2
27	9		MCL: CCL (as above)	1.30	13.0	46.4	0.58	49.2	6.2
33	5		CL(680, 40 K/h):HW(D:67%):H (600): CCL (15−4 K/h, 500) [a]	1.15	11.5	24.8	0.31	19.0	2.4
33	7	2 Cu	As above	1.19	11.9	38.8	0.485	26.2	3.3
33	7		As above	1.18	11.8	42.0	0.525	33.3	4.2
33	9		As above	1.24	12.4	46.4	0.58	32.5	4.1
28	7		CL($> T_s$, 60 ($T_s = 645$ °C))	0.97	9.7	26.4	0.33	11.1	1.4
31	5		(Sintered 1400 °C, 4 h; H$_2$) [b]:WQ: H (700, 30): FCL (700, 640):MCL (640, 0.9 K/h, 500)	1.23	12.3	40.0	0.5	34.9	4.4

[a] For the deformation aging process the initially aged state corresponds to an overaged state

[b] Sintering ST

Commercial materials are characterized by the fact that they can be quenched from temperatures above the miscibility gap first, which results in mechanical properties amenable to forming by conventional processes such as rolling, stamping, drilling. The final annealing treatment in the miscibility gap results in the magnetically hard state. This is associated with a drastic decrease in ductility. If the annealing treatment is carried out in a magnetic field, the final product has an anisotropic behavior. Table 4.3-35 shows the property range of commercial Fe−Cr−Co materials.

4.3.3.2 Fe−Co−V

Magnetic materials based on the Fe−Co−V alloy system were the first ductile magnets. The intrinsic magnetic properties may be found in [3.6] while extensive magnetic materials data are treated in [3.56]. The optimum magnetic behavior is obtained for alloy compositions around Fe–55 wt% Co–10 wt% V. As the isothermal sections of the Fe−Co−V phase diagram Fig. 4.3-56a and Fig. 4.3-56b show, this alloy is mainly in the fcc γ-phase (austenite) state at 900 °C,

Table 4.3-35 Commercial Fe−Cr−Co magnetic materials

Composition nominal	Variant	Remanence	Coercivity	Energy density	Curie temperature	Maximum application temperature	Hardness HV	Commercial designation [a]
wt%		(T)	(kA m^{-1})	(kJ m^{-3})	(°C)	(°C)		
Fe−27Cr−11Co−Mo	isotropic	0.85−0.95	36−42	13	640	480	480	12/160
Fe−28Cr−16Co−Mo	isotropic	0.80−0.90	39−45	15	640	480	480	16/160
Fe−27Cr−11Co−Mo	anisotropic	1.15−1.25	47−55	35	640	480	480	12/500
Fe−28Cr−16Co−Mo	anisotropic	1.10−1.20	53−61	37	640	480	480	16/550

[a] Designation of CROVAC® by Vacuumschmelze, Hanau, Germany
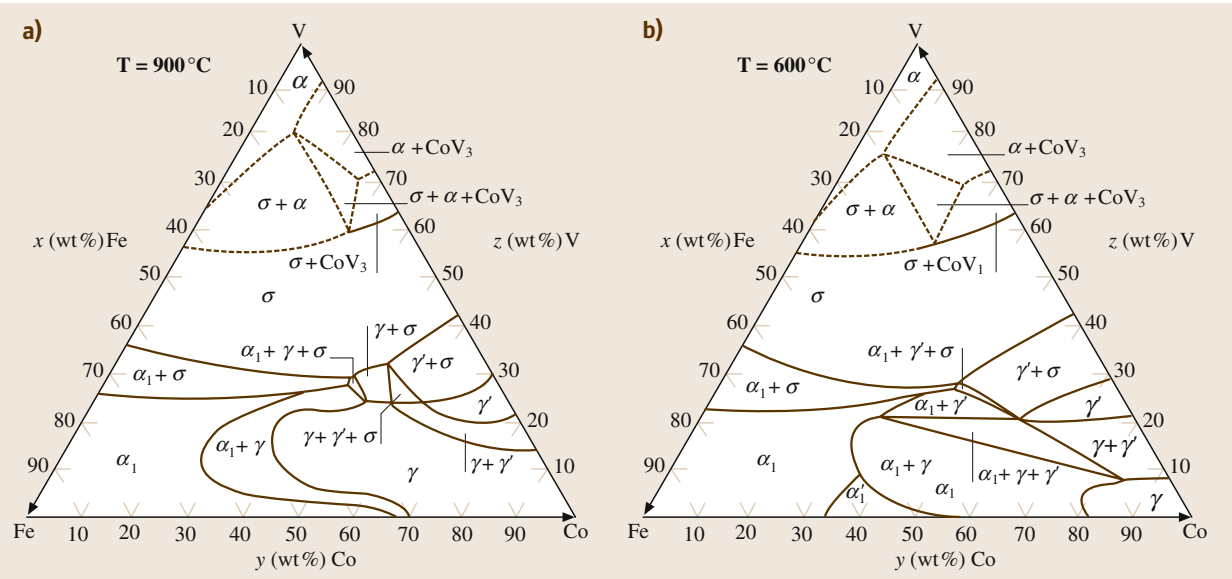
Fig. 4.3-56a,b Isothermal sections of the Fe−Co−V phase diagram at 900 °C (**a**) and 600 °C (**b**). α: bcc disordered; α_1: bcc ordered (CsCl type); γ: fcc disordered (austenite); γ': fcc ordered (Au$_3$Cu type) [3.56]

Table 4.3-36 Commercial Fe−Co−V-based magnetic materials

Composition nominal	Remanence	Coercivity	Energy density	Curie temperature	Maximum application temperature	Hardness (HV)		Alloy code [a]
						As rolled	Heat treated	
(wt%)	(T)	(kA m^{-1})	(kJ m^{-3})	(°C)	(°C)			
34Fe−52Co−13V	0.80−0.90	25−30	12	700	500	480	900	35U
34Fe−53Co−8.5V−3.5Cr	1.00−1.10	30−35	20	700	500	520	950	93

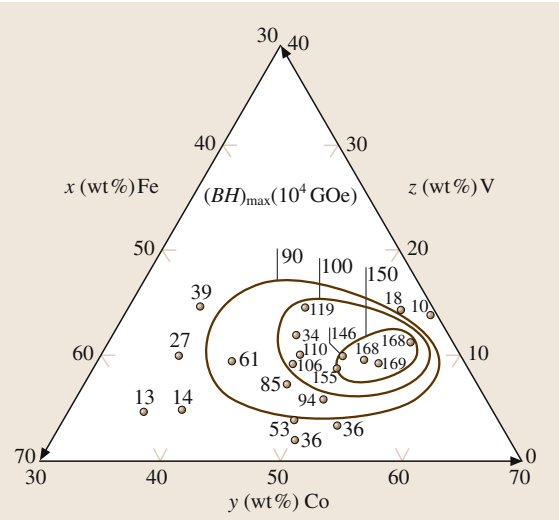[a] Designation of MAGNETOFLEX® by Vacuumschmelze, Hanau, Germany

Fig. 4.3-57 Contour map of $(BH)_{max}$ of Fe−Co−V alloys in the optimum annealed state. It is obtained by annealing in the temperature range $T_a = 555-750\,°C$ in the magnetically preferred direction of the anisotropic sample [3.56]

while it decomposes into the bcc ordered $\alpha_1 + \gamma$ state upon annealing at lower temperature such as 600 °C. In combinations of heat treatment with plastic deformation (also serving to form the product, e.g., wire) an optimum anisotropic hard magnetic state can be realized.

If quenched from the γ-phase state, the alloy can be deformed. By a judicious choice of annealing temperatures in the range of 555 to 750 °C the maximum energy product as a function of alloy composition, as shown in Fig. 4.3-57, may be obtained. This annealing treatment is associated with a drastic increase in hardness,

as indicated in Table 4.3-36, and a concomitant loss in ductility.

Based on these interrelations of phase equilibria and thermomechanical treatments as well as by optimization through further alloying additions, commercial magnetic materials such as those listed with their properties in Table 4.3-36 have been developed.

4.3.3.3 Fe−Ni−Al−Co, Alnico

The term Alnico refers to two-phase hard magnetic materials based on the Fe−Ni−Al system (Fig. 4.3-58). The intrinsic magnetic properties may be found in [3.6], while extensive magnetic materials data are treated in [3.56]. Table 4.3-37 lists some of the magnetic properties of Alnico type magnets. The magnetically optimized microstructure consists essentially of elongated ferromagnetic Fe-rich precipitates (α_1-phase, bcc disordered) in a non-magnetic matrix of NiAl (α_2-phase, bcc ordered, CsCl type). The remanence B_r is increased significantly by adding Co, which leads to the formation of precipitates rich in Fe−Co. The coercivity H_c is optimized by adding Ti and Cu. The two-phase state is obtained by a homogenization at about 1300 °C, followed by annealing treatments which lead to decomposition into structurally coherent phases on the nanometer scale. The particles are aligned preferentially along the ⟨100⟩ directions of the bcc lattice. This decomposition microstructure is the essential microstructural feature. Higher remanence and coercivity prevails in chill-cast magnets with a columnar microstructure and ⟨100⟩ fiber texture, providing additional magnetocrystalline anisotropy. More extensive treatments and data may be found in [3.10, 56, 57].
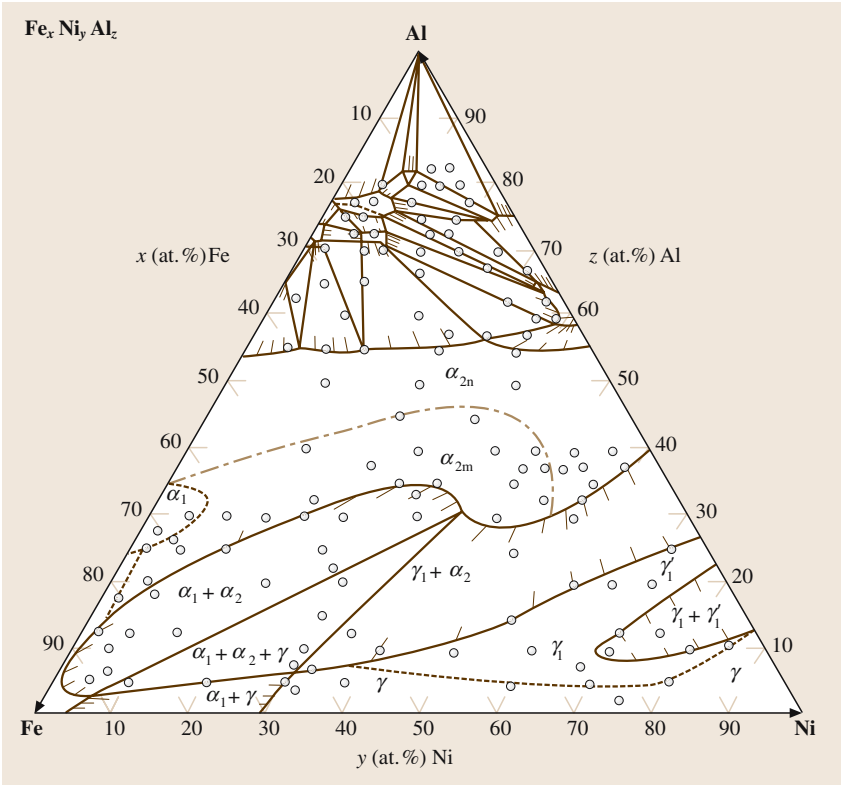
Fig. 4.3–58 Effective $Fe_xNi_yAl_z$ phase diagram after cooling from the melt at 10 K/h. *Broken lines* indicate superlattice phase boundaries; the *point-dash line* the magnetic phase boundary in the Ni(Al,Fe) phase field. α_1: bcc; α_1': Fe_3Al-type superlattice phase; α_2: (Fe,Ni)Al-type superlattice phase; γ: fcc; γ_1: Ni_3Al-type superlattice phase; γ_1': as γ_1 but with the larger lattice spacing. The indices m and n indicate magnetic and non-magnetic phases, respectively

Table 4.3–37 Magnetic properties of Alnico type magnets

Designation according to DIN 17410[a]	Remanence B_r		Coercivity $_BH_c$		$_JH_c$		Energy density $(BH)_{max}$		Alloy code[b]
	(mT)	(G)	(kA m^{-1})	(Oe)	(kA m^{-1})	(Oe)	(kJ m^{-3})	(MGOe)	
AlNiCo 9/5i	550	5500	54	679	57	716	10.3	1.3	130
AlNiCo 12/6i	650	6500	57	716	60	754	13.5	1.7	160
AlNiCo 19/11i	640	6400	105	1319	115	1433	22.3	2.8	260
AlNiCo 15/6a	750	7500	60	54	62	57	16.7	2.1	190
AlNiCo 28/6a	1100	11 000	64	804	65	817	31.8	4.0	400
AlNiCo 39/12a	880	8800	115	1445	119	1495	43.8	5.5	450
AlNiCo 37/5a	1240	12 400	51	641	51	641	41.4	5.2	500
AlNiCo 39/15a	740	7400	150	1855	160	2011	43.8	5.5	1800

[a] i = isotropic; a = anisotropic

[b] Commercial designations of Koerzit® by WIDIA Magnettechnik

Table 4.3-38 Intrinsic properties of $Fe_{14}RE_2B$ at $T = 300\,K$

RE	K_1 $(10^7\ \mathrm{erg\,cm^{-3}})$	$4\pi M_s$ (T)	$H_a = 2K_1/M_s$ $(\mathrm{MA\,m^{-1}})$	T_c (K)
Ce	1.7	1.28 (4)	3.0	430 (6)
Pr	4.5	1.59 (8)	6.3	563 (3)
Nd	4.8 (3)	1.68 (9)	5.7	590 (5)
Sm	plane	1.55 (10)		618
Gd	1.0	0.94 (2)	2.3	665 (4)
Tb		0.72 (5)	11.1 [a]	639
Dy	4.1	0.75 (5)	12.6	597 (5)
Ho		0.84 (12)	5.7 [a]	576
Er	plane	1.02 (12)		556 (3)
TM		1.25 (2)		543 (2)
Lu		–	2.1 [a]	538
La		–		543
Y	1.1(1)	1.40(5)	2.2	566 (2)

[a] Data taken from [3.58]. H_a value obtained directly by extrapolation of the magnetization curves for the easy and the hard direction. The average value is given where more than one reference is available; the number in parentheses indicates the standard deviation in the last figure

4.3.3.4 Fe−Nd−B

The most powerful permanent magnets presently available consist essentially of the tetragonal $Fe_{14}Nd_2B$ phase. The intrinsic magnetic properties may be found in [3.6] while extensive magnetic materials treatments and data may be found in [3.1, 10, 56]. Two different production routes are used to prepare dense anisotropic magnets: conventional powder metallurgy and a rapid quenching process to produce flake-shaped powder particles with a nanocrystalline microstructure as a starting material. The flakes are then processed further into dense isotropic or anisotropic magnets by means of a combination of cold pre-forming, hot pressing, and hot deformation steps.

The $Fe_{14}RE_2B$ phase is formed with all rare earth (RE) elements with the exception of Eu. Their intrinsic properties have been investigated extensively. They are listed in Table 4.3-38. Neodymium shows the highest permanent magnet potential based on its combination of high values of K_1 and M_s.

Conventional Powder Metallurgical Processing
Figure 4.3-59 shows the approximate phase relations of Fe−Nd−B at room temperature. According to the phase diagram of the Fe−Nd−B system the $Fe_{14}Nd_2B$ phase forms at 1180 °C. In powder metallurgical processing

of the magnets, sintering at 1050 °C leads to the formation of $Fe_{14}Nd_2B$ in equilibrium with a Nd-rich liquid and with the Fe_4NdB_4 boride phase. The liquid phase solidifies below the ternary eutectic at 630 °C. The resulting non-magnetic Nd-rich solid phase spreads along
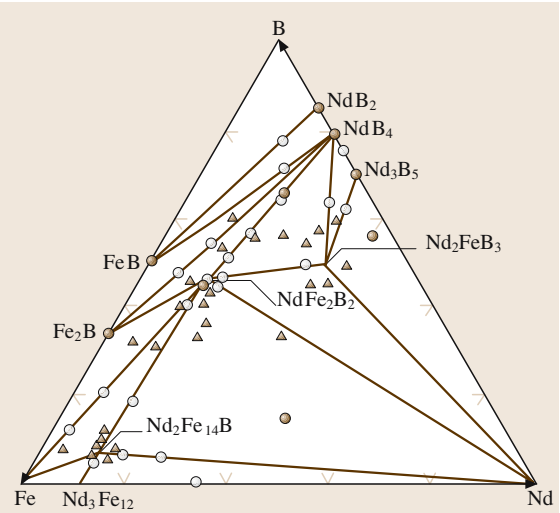

Fig. 4.3-59 Approximate phase relations of Fe−Nd−B at room temperature
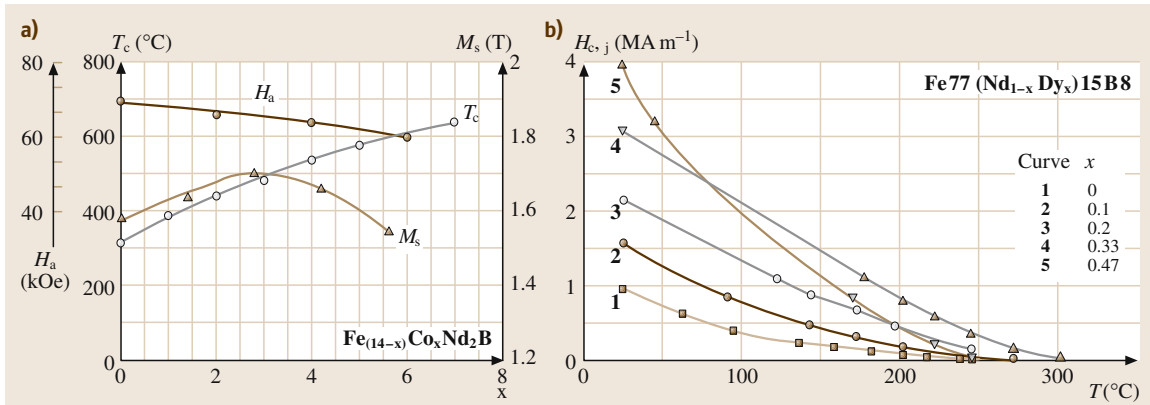
Fig. 4.3-60a,b Influence of substitutional elements on $Fe_{14}Nd_2B$ type magnets. (**a**) Influence of the Co content on the intrinsic properties at room temperature. Data for the magnetization M_s, for the anisotropy field H_a, and for the Curie temperature T_c. (**b**) Influence of the Dy content on the temperature dependence of the coercivity $_JH_c$ of sintered magnets. There is an approximately linear increase of $_JH_c$ at room temperature. The temperature dependence increases with increasing Dy content

the grain boundaries and provides the magnetic decoupling of the $Fe_{14}Nd_2B$ grains, thus providing the basic coercivity of the sintered magnet.

Additions of Dy and Al are increasing the coercivity. Dysprosium enters the RE sites in the $Fe_{14}Nd_2B$ structure, increasing the magnetocrystalline anisotropy but decreasing the magnetic remanence B_r. At compositions of > 2 at.% Al, the anisotropy field H_a decreases linearly at a rate of $0.13\,\text{MA m}^{-1}$ per at.% Al. Nevertheless the coercivity increases significantly due to an optimization of the microstructure: Al is enriched in the Nd grain boundary phase which is spreading more uniformly around the magnetic grains, thus leading to better decoupling of exchange interactions. This is a basic condition for the increase in coercivity.

As indicated by Fig. 4.3-60a, Co addition leads to a strong increase of the Curie temperature. However, the anisotropy field H_a is reduced by Co, and the decrease of the coercive field is even larger than expected from this decrease in H_a. On the other hand, there is only a small increase in the magnetic saturation with a maximum at 20 at.% Fe substituted by Co. Accordingly the alloying is limited to 20 at.% Co.

The vulnerability of RE compounds to corrosion is a problem. The corrosion behavior of Fe−Nd−B

magnets has been improved by adding elements which influence the electrochemical properties of the Nd-rich grain boundary phase. Additions of small amounts of more noble elements such as Cu, Co, Ga, Nb, and V result in the formation of compounds which replace the highly corrosive Nd-rich phase. Table 4.3-39 lists some of the elements used for manufacturing Fe−Nd−B magnets.

A multitude of grades of Fe−Nd−B magnets is produced by varying chemical composition and processing, such as the press technique applied in order to satisfy the different specifications required for the different fields of application. A maximum remanence is needed, for instance, for disc drive systems in personal computers and for background field magnets in magnetic resonance imaging systems. On the other hand, straight line demagnetization curves up to operating temperatures of 150 °C are specified for application in highly dynamic motors. This requires very high coercive fields at room temperature. Magnetic remanence values of $B_r > 1.4\,\text{T}$ as well as $_JH_c$ values of $> 2500\,\text{kA/m}$ can be achieved. However, high B_r values are attainable only with lowering the $_JH_c$ value and the operating temperature, and vice versa. Possible combinations of B_r and $_JH_c$ for a given manufacturing process (pressing technique), can be rep-

Table 4.3-39 Elements used for manufacturing Fe−Nd−B magnets

Element	Fe	Nd	B	Dy	Co	Al	Ga	Nb, V
wt%	balance	15−33	0.8−1	0−15	0−15	0.5−2	0−2	0−4

Table 4.3-40 Physical properties of sintered Nd–Fe–B magnets [a]

Density	Curie temperature	Electrical resistivity	Specific heat	Thermal conductivity	Thermal expansion coefficient		Young's modulus	Flexural strength	Compression strength	Vickers Hardness
					∥-c axis	⊥-c axis				
(g cm^{-3})	(K)	(Ω mm^2 m^{-1})	(J kg^{-1} K^{-1})	(W m^{-1} K^{-1})	(10^{-6} K^{-1})	(10^{-6} K^{-1})	(kN mm^{-2})	(N mm^{-2})	(N mm^{-2})	
7.5 (0.05)	580–605	1.50 (0.10)	430 (10)	9	4.4 (0.6)	-1	155 (5)	260 (10)	930 (170)	580 (10)

[a] All values are for 300 K. The values are the averages taken from the companies brochures of: VAC Vacuumschmelze, Hanau, Germany; MS Magnetfabrik Schramberg, Schramberg, Germany; Ugimag Inc, Valparaiso, USA; Neorem Magnets Oy, Ulvila, Finland; TDK Corporation, Tokyo, Japan; Hitachi Metals Ltd, Tokyo, Japan. The numbers in parentheses indicate the maximum deviation
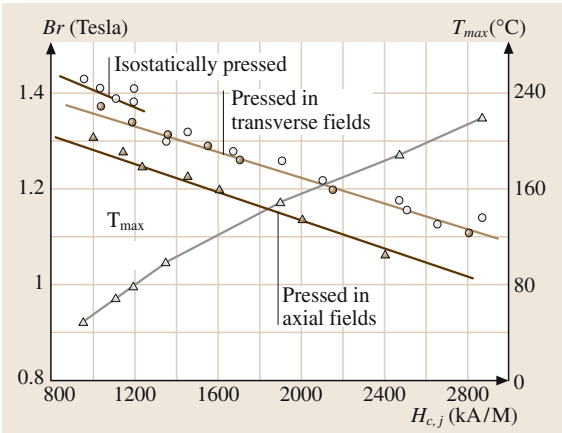

Fig. 4.3-61 Sintered Nd–Fe–B magnets. Possible combinations of B_r and $_JH_c$

resented by a straight line, as shown in Fig. 4.3-61. The physical properties of sintered Nd–Fe–B magnets are given in Table 4.3-40.

Magnets Processed by the Rapid Quenching/Hot Working Technique

This alternative technology uses isotropic or amorphous material processed by a rapid quench technique involving melt spinning the molten alloy through a nozzle on to a rotating wheel. Flakes that are about 30 μm thick are obtained. Their microstructure shows typically an average grain size of 50 to 60 nm. The material is subjected to controlled deformation at elevated temperatures, which gives rise to a texture oriented perpendicular to the direction of mass flow during deformation. Hot working processes applied are the die-upset method and indirect extrusion. The major steps of the process are: alloy preparation, melt spinning, cold forming, hot

working, coating, and magnetizing. The first step of the hot working procedure is pressing to 100% density at temperatures between 700 and 800 °C. Isotropic magnets are obtained. The isotropic parts are deformed at about 800 °C by using the die-upset technique. Constant strain rates have to be applied. Typically, the strain rate is about 0.1 sec^{-1}. The strain rate and the degree of deformation determine the alignment factor of the final magnet. A maximum value for the magnetic remanence B_r of about 1.35 T may be achieved under economically reasonable conditions. The relationship between the degree of deformation and B_r is shown in Fig. 4.3-62. Properties of commercially availabe magnets are included in Table 4.3-41. The application of the magnets is limited to special fields where complicated shapes would otherwise require expensive machining
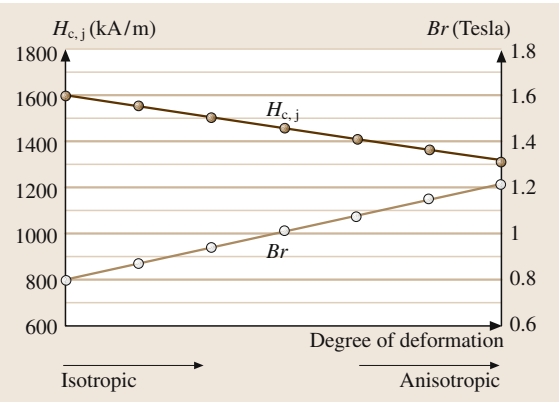

Fig. 4.3-62 Dependence of remanence B_r and coercivity $_JH_r$ of dense magnets, manufactured by the hot pressing/hot working technique, on the degree of deformation. Data provided and authorized for publication by Magnequench Int., Tübingen

Table 4.3-41 Magnetic properties of $Fe_{14}Nd_2B$-based magnetic materials at room temperature. Typical values of commercially available magnets

Remanence (T) B_r	Coercivity (kA m^{-1}) $_BH_c$	$_JH_c$	Energy density (kJ m^{-3}) $(BH)_{max}$	Temperature coefficients (% K^{-1}) $TC(B_r)$	$TC(_JH_c)$	Max. operation temperature[a] (°C) T_{max}	Product code[b]
Sinter Route							
1.47	915	955	415	−0.115	−0.77	50	VD722HR
1.44	1115	1195	400	−0.115	−0.73	70	VD745HR
1.35	1040	1430	350	−0.095	−0.65	110	VD633HR
1.30	980	1035	325	−0.115	−0.80	70	VD335HR
1.18	915	2465	270	−0.085	−0.55	190	VD677HR
1.43	915	9550	395	−0.115	−0.77	50	VD722TP
1.41	1090	1195	385	−0.115	−0.73	70	VD745TP
1.32	1020	1430	335	−0.095	−0.65	110	VD633TP
1.25	965	1195	300	−0.115	−0.75	70	VD335TP
1.14	885	2865	250	−0.080	−0.51	220	VD688TP
1.32	965	1115	335	−0.115	−0.73	80	VD510AP
1.26	965	1510	305	−0.095	−0.64	120	VD633AP
1.22	900	1195	285	−0.115	−0.75	80	VD335AP
1.08	830	2865	225	−0.080	−0.51	230	VD688AP
Hot Working							
0.83	575	1400	120	−0.10	−0.50	180	MQ2-E15
1.28	907	995	302	−0.10	−0.60	125	MQ3-E38
1.25	915	1313	287	−0.09	−0.60	150	MQ3-F36
1.31	979	1274	334	−0.09	−0.60	150	MQ3-F42
1.16	876	1592	255	−0.09	−0.06	200	MQ3-G32SH

[a] Maximum operating temperature is defined by a straight demagnetization line up to an operation point of the magnet of $B/\mu_0 H = -2$

[b] VD = Vacodym, trade name of Vacuumschmelze GmbH for NdFeB based magnets; HR grades = isostatically pressed, TP grades = transverse field pressed, AP grades = axial field pressed. MQ2, MQ3 = trade names of Magnequench International Inc. for hot pressed - hot deformed magnets

work, as for instance screwed arcs for non-cogging motors.

Typical technical alloys and their properties are listed in Table 4.3-41. Characteristic demagnetization curves are shown in Fig. 4.3-63.

4.3.3.5 Co–Sm

Numerous magnetic, binary, rare earth (RE) transition metal (TM) compounds exist, of which the Co_5RE and $Co_{17}RE_2$ phases form the basis for materials with excellent permanent magnetic properties. They combine high saturation magnetization M_s with high crystal anisotropy K_1 and high Curie temperature T_c. The intrinsic magnetic properties of the Co_5RE and $Co_{17}RE_2$ phases are summarized in Tables 4.3-42 and 4.3-43, respectively (Co_5RE and $Co_{17}RE_2$ are, also, referred to as 5/1 and 17/2 phases). It is obvious that Co_5Sm and $Co_{17}Sm_2$ have the best potential for manufacturing permanent magnetic materials.
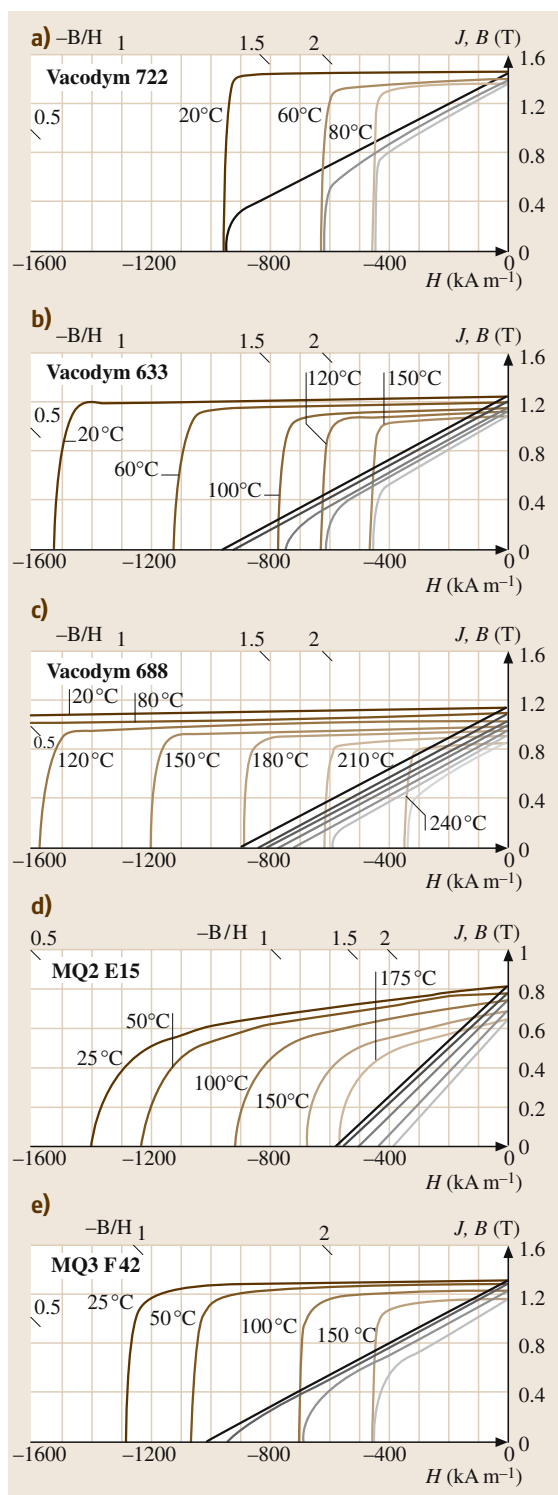
Fig. 4.3-63a–e $Fe_{14}Nd_2B$-based commercial magnets [3.10]. **(a)** Top grade magnet with highest remanence B_r. Isostatically pressed, designed to meet exceptional requirements for maximum energy density at operating temperatures up to 60 °C. **(b)** Magnet, axially pressed, with an optimum combination of high coercivity and energy product **(c)** Magnet, axially pressed, with a very high coercivity; exceptionally well suited for use in highly dynamic servo motor applications. **(d)** Isotropic dense magnet made from rapidly quenched powder by means of the hot pressing technique. **(e)** Magnet made from rapidly quenched powder by means of the hot pressing and hot deforming technique; especially well suited for complicated shaped magnets, such as scewed arcs in special motor applications
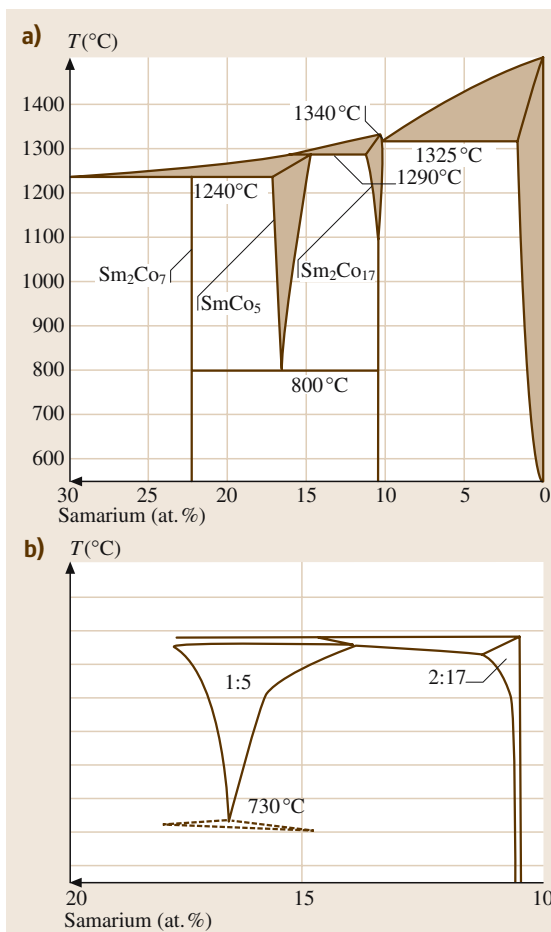

Fig. 4.3-64 (a) Part of the Co−Sm phase diagram. **(b)** Section of the Co−Sm−Cu phase diagram at 10 at.% Cu [3.10]

Table 4.3-42 Co_5RE alloys. Room temperature intrinsic magnetic properties, the crystal anisotropy constant K_1, the magnetic saturation M_s, the anisotropy field $H_a = 2K_1/M_s$, and the Curie temperature, T_c [3.10]

RE[a]	K_1^b (10^7 erg cm^{-3})	$4\pi M_s^b$ (T)	H_a (MA m^{-1})	T_c^b (K)
Ce	5.3 (6)	0.83	13	660 (20)
Pr	8.1 (9)	1.29	12.5	900 (10)
Nd	0.7 (5)	1.34	1.1	910 (2)
Sm	17.2 (9)	1.12 (3)	31	990 (10)
Gd	4.6 (5)	0.35 (3)	26	1035
Tb	NC			973
Dy	NC			961
Ho	3.6 (3)	0.52	13.8	996
Er	4.2 (4)	0.4	14.6	983
La	5.9 (5)	0.91	10.6	834
Y	5.2 (4)	1.11	9.3	980

[a] No data are available for the RE elements Tm, Yb, and Lu

[b] The mean value is given where more than one reference is available; the number in parentheses indicates the standard deviation in the last figure. NC: non-collinear spin structure

Table 4.3-43 Room temperature intrinsic magnetic properties, of $Co_{17}RE_2$ alloys [3.10]

RE[a]	K_1^b (10^7 erg cm^{-3})	$4\pi M_s^b$ (T)	H_a (MA m^{-1})	T_c^b (K)
Ce	− 0.6	1.15		1068 (10)
Pr	− 0.6	1.38		1160 (10)
Nd	− 1.1	1.39		1160 (3)
Sm	3.3 (1)	1.25 (3)	5.3 (1)	1196 (1)
Gd	− 0.5	0.73		1212 (6)
Tb	− 3.3 (6)	0.67		1189 (4)
Dy	− 2.6 (5)	0.69		1173 (8)
Ho	− 1.0 (2)	0.85		1177 (1)
Er	0.41 (3)	1.05 (5)	0.75	1175 (15)
TM	0.50 (5)	1.21	0.83	1179 (2)
Yb	− 0.38	1.35		1180
Lu	− 0.20 (5)	1.41		1202 (6)
Y	− 0.34 (2)	1.27		1199 (13)

[a] La does not form the 17/2 phase. The 17/2 phases with Sm, Er, and Tm show uniaxial anisotropy while all others have easy plane anisotropy

[b] The mean value is given where more than one reference is available; the number in parentheses indicates the standard deviation in the last figure

Phase Equilibria of Co−RE Systems

The phase diagrams of Co−RE systems are very similar. Figure 4.3-64 shows the magnetically relevant part of the Co−Sm phase diagram. The features to note are: Co and $Co_{17}Sm_2$ form a eutectic, while Co_5Sm forms as a result of a peritectic reaction between $Co_{17}Sm_2$ and liquid.

Both Co_5Sm and $Co_{17}Sm_2$ show a significant range of homogeneity at elevated temperatures. The compound Co_5Sm is unstable at room temperature and decomposes via an eutectoid reaction into Co_7Sm_2 and $Co_{17}Sm_2$.

Iron and Cu are two important substitutional elements for Co−RE alloys with respect to manufacturing

permanent magnets. In Co_5RE compounds, Fe may substitute up to 5 at.% Co while complete solubility occurs in $(Co_{1-x}Fe_x)_{17}RE_2$. Copper is essential in $Co_{17}Sm_2$ type alloys. The different solubility of Cu in 5/1 and 17/2 is used to form precipitates in the 17/2 phase, resulting in a microstructure which provides high coercivity.

Co–Sm–Based Permanent Magnets

Powder Metallurgical Processing. Cobalt–Samarium magnets are produced using powder metallurgical techniques. Alloys are prepared by an inductive melting process or a Ca reduction process. The starting alloys are crushed and pulverized to single crystalline particles 3–4 μm in diameter. The powders are compacted in a magnetic field to obtain anisotropic magnets: by uniaxial compaction in magnetic fields, either parallel or transverse to the direction of the applied force; or by isostatic compaction of powders in elastic bags after subjecting the filled bags to a pulsed field. The magnet-

ically aligned green compacts are sintered in an inert atmosphere to achieve an optimum combination of high density and high coercive field.

5/1 Type Magnets. Binary Co_5Sm is the basis of 5/1 type magnets. Table 4.3-44 lists some of the magnetic properties at room temperature and Table 4.3-45 lists the physical properties of sintered Co_5Sm magnets. Partial substitution of Sm by Pr increases B_s while still yielding sufficiently high $_JH_c$. The microstructure of Co_5Sm magnets consists of single domain grains. Magnetization reversal starts by nucleation of domains in a demagnetizing field. The domain wall moves easily through the particle.

The application of permanent magnets in measuring devices or in devices in aircraft or space systems requires a small temperature coefficient (TC) of B_r. The combination of Co_5Sm which has a negative TC, with Co_5Gd, which has a positive TC, yields magnets with reduced temperature dependence of B_r, reaching about

Table 4.3-44 Co_5Sm-based magnetic materials. Magnetic properties at room temperature, typical values [3.10]

B_r (T)	$_BH_c$ (kA m^{-1})	$_JH_c$ (kA m^{-1})	$(BH)_{max}$ (kJ m^{-3})	Press mode [a]	Material	Producer code [b]
1.01	755	1500	200	Iso	Co_5Sm	Vacomax 200
0.95	720	1800	180	TR	Co_5Sm	Vacomax 170
1.0	775	2400	200	Iso	Co_5Sm	Recoma 25
0.94	730	2400	175	TR	Co_5Sm	Recoma 22
0.9	700	2400	160	A	Co_5Sm	Recoma 20
0.73	570	>2400	105	A	$Co_5Sm_{0.8}Gd_{0.2}$	EEC 1.5TC-13
0.61	480	>2400	70	A	$Co_5Sm_{06}Gd_{0.4}$	EEC 1.5TC-9

[a] Iso: isostatically pressed; TR: uniaxially pressed in transverse oriented aligning fields; A: uniaxially pressed in axially oriented aligning fields

[b] Vacomax: Trademark of Vacuumschmelze GmbH, Germany; Recoma: Trademark of Ugimag AG, Switzerland; EEC: Trademark of EEC Electron Energy Corporation, USA

Table 4.3-45 Physical properties of sintered Co_5Sm magnets [a] [3.10]

Density (g cm^{-3})	Curie temperature (K)	Electrical resistivity (Ω mm^2 m^{-1})	Specific heat (J kg^{-1} K^{-1})	Thermal conductivity (W m^{-1} K^{-1})	Thermal expansion coefficient ∥ c axis (10^{-6} K^{-1})	Thermal expansion coefficient ⊥ c axis (10^{-6} K^{-1})	Young's modulus (kN mm^{-2})	Flexural strength (N mm^{-2})	Compression strength (N mm^{-2})	Vickers Hardness
8.40 (0.10)	990 (10)	0.53 (0.03)	372 (3)	11.5 (1.0)	6.0 (1.5)	12.5 (0.5)	150 (40)	125 (35)	900 (300)	580 (50)

[a] All values for 300 K. Average values are taken from the companies brochures of: VAC Vacuumschmelze, Hanau, Germany; MS Magnetfabrik Schramberg, Schramberg, Germany; Ugimag AG, Lupfig, Switzerland; EEC Electron Energy Corporation, Landisville, USA; TDK Corporation, Tokyo Japan; Hitachi Metals Ltd, Tokyo, Japan. The numbers in parentheses indicate the standard deviation
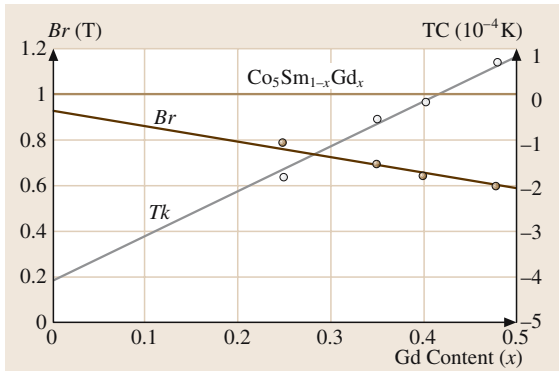
Fig. 4.3-65 Temperature coefficient TC of $Co_5Sm_{1-x}Gd_x$ magnets in the temperature range between 20 and 200 °C. The coercivity of these ternary magnets is comparable to that of binary Co_5Sm magnets due to the high anisotropy field of Co_5Gd $H_a = 24$ MA m^{-1} while for Co_5Sm, $H_a = 31$ MA m^{-1} [3.10]

zero for $Co_5Sm_{0.6}Gd_{0.4}$ between room temperature and 200 °C (Fig. 4.3-65).

Tables 4.3-44 and 4.3-45 list the magnetic properties of typical Co_5Sm based magnets and their physical properties, respectively. Figures 4.3-66a,b show characteristic demagnetisation curves.

17/2 Type Magnets. The permanent magnetic potential of the binary phase $Co_{17}Sm_2$ is increased by partially substituting Co by other transition metals. The general chemical composition of commercial magnets corresponds to $(Co_{bal}Fe_vCu_yZr_x)_zSm$. Copper is the essential addition. Its solubility in the 17/2 phase is strongly temperature-dependent, and this is used for precipitation hardening of 17/2 magnets.

The influence of Fe on the intrinsic magnetic properties is summarized in Fig. 4.3-67. Both Zr and Hf increase coercivity. Figures 4.3-67a,b show the combined effects of Fe, Cu, and Zr additions and the Co/Sm ratio on the temperature dependence of coercivity $_JH_c$. The magnets are sintered between 1200 and 1220 °C. A single phase with $Zn_{17}Th_2$ structure is obtained by homogenization at temperatures between 1160 and 1190 °C. After rapid cooling the magnets are finally annealed between 800 and 850 °C, followed by cooling to 400 °C. The microstructure leading to high coercivity $_JH_c$ consists of 17/2 matrix grains, a 5/1 boundary phase enriched in Cu, and platelet-shaped precipitates enriched in Fe and Zr. The coercivity of these magnets
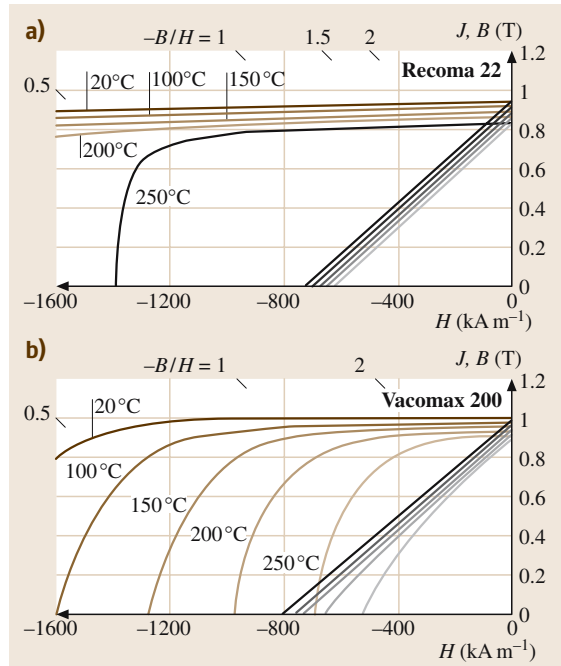

Fig. 4.3-66a,b Co_5Sm magnets. Demagnetization curves of typical commercially available magnets [3.10]. **(a)** Magnet with high intrinsic coercivity $_JH_c$ up to 300 °C, uniaxially pressed in a transverse aligning field; Recoma: trademark of Ugimag AG, Switzerland. **(b)** Magnet with highest energy density obtained by cutting from isostatically pressed block; Vacomax: trademark of Vacuumschmelze GmbH, Germany
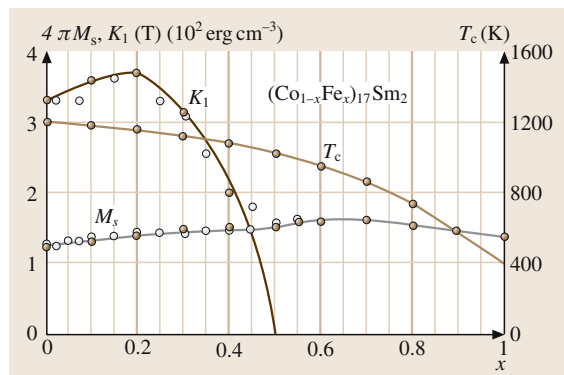

Fig. 4.3-67 $(Co_{1-x}Fe_x)_{17}Sm_2$. Dependence K_1, $4\pi M_s$, and T_c on the Fe content x [3.10]

is based on pinning of the Bloch walls at the 5/1 grain boundary phase.

Part 4 | 3.3

Table 4.3-46 Chemical composition of commercial high energy 17/2 magnets [3.10]

Element	Sm [a]	Co	Cu	Fe	Zr
wt%	25–27	balance	4.5–8	14–20	1.5–3

[a] The Sm content includes the fraction of Sm which is present as Sm_2O_3, typically 2.5 wt%

Table 4.3-47 Annealing treatments for 17/2 type magnets [3.10]

	Isothermal ageing	Cooling rate to 400 °C	$_JH_c$ (kA m^{-1})	Magnetizing field H_m (kA m^{-1})
high $_JH_c$	850 °C/10 hours	1 K/min	> 2000	5000
low $_JH_c$	800 °C/30 min.	5 K/min	500–800	1500

Table 4.3-48 High energy $TM_{17}Sm_2$ magnets for applications up to 300 °C, typical values [3.10]

B_r (T)	$_BH_c$ (kA m^{-1})	$_JH_c$ (kA m^{-1})	$(BH)_{max}$ (kJ m^{-3})	Press mode [a]	Material	Producer code [b]
1.14	670	800	247	Iso	$TM_{17}Sm_2$	Hicorex -30CH
1.12	730	800	240	Iso	$TM_{17}Sm_2$	Vacomax 240HR
1.05	720	800	210	A	$TM_{17}Sm_2$	Vacomax 240
1.10	820	2070	225	Iso	$TM_{17}Sm_2$	Vacomax 225HR
1.07	800	2000	215	TR	$TM_{17}Sm_2$	Recoma 28
1.04	760	2070	205	A	$TM_{17}Sm_2$	Vacomax 225
0.9	654	> 2000	150	A	$TM_{17}(Sm_{0.8}, Gd_{0.2})_2$	EEC2:17TC-18
0.8	575	> 2000	115	A	$TM_{17}(Sm_{0.6}, Gd_{0.4})_2$	EEC2:17TC-15

[a] Iso: isostatically pressed; TR: uniaxially pressed in transverse oriented aligning fields; A: uniaxially pressed in parallel oriented aligning fields

[b] Hicorex: Trademark of Hitachi Metals Ltd., Japan; Vacomax: Trademark of Vacuumschmelze GmbH, Germany; Recoma: Trademark of Ugimag AG, Switzerland; EEC: Trademark of EEC Electron Energy Corporation, USA

Table 4.3-49 Composition of 17/2 magnets for operating up to 550 °C [3.10]

Element	Sm	Co	Cu	Fe	Zr
wt%	26.5–29	balance	6–12	7	2.5–6

Table 4.3-50 Physical properties of sintered $TM_{17}Sm_2$ magnets [a] [3.10]

Density	Curie temperature	Electrical resistivity	Specific heat	Thermal conductivity	Thermal expansion coefficient		Young's modulus	Flexural strength	Compression strength	Vickers hardness
					∥-c axis	⊥-c axis				
(g cm^{-3})	(K)	(Ω mm^2 m^{-1})	(J kg^{-1} K^{-1})	(W m^{-1} K^{-1})	(10^{-6} K^{-1})	(10^{-6} K^{-1})	(kN mm^{-2})	(kN mm^{-2})	(kN mm^{-2})	
8.38 (0.08)	1079 (8)	0.86 (0.05)	355 (30)	10.5 (1.5)	8.4 (1)	11.5 (0.5)	160 (40)	130 (15)	760 (150)	600 (50)

[a] All values are for 300 K. The values are the average of values taken from company brochures

High Energy Magnets for Applications at Temperatures up to 300 °C. The compositional parameters v, y, x, and z of the 17/2 type magnets are normally optimized for highest $(BH)_{max}$ between room temperature and 300 °C. The range of chemical compositions of these high energy magnets is given in Table 4.3-46.

Tables 4.3-48 and 4.3-50 list the magnetic properties of typical $Co_{17}Sm_2$ based magnets and their physical properties, respectively. Figures 4.3-69a–c show characteristic demagnetization curves.

Two modifications of 17/2 magnets can be obtained from identical chemical compositions according to the annealing treatment applied (see Table 4.3-47). 17/2 magnets with reduced TC of B_r are obtained by substituting part of Sm by Gd. Table 4.3-45 shows some

typical values of the magnetic properties of high energy $TM_{17}Sm_2$ magnets.

Magnets for High Temperature Applications. Special applications in aircraft and spacecraft require magnets with linear demagnetization curves up to 550 °C. Suitable high temperature magnets are obtained by increasing Sm and Cu and decreasing Fe. Data are given in Table 4.3-49 and Fig. 4.3-69a.
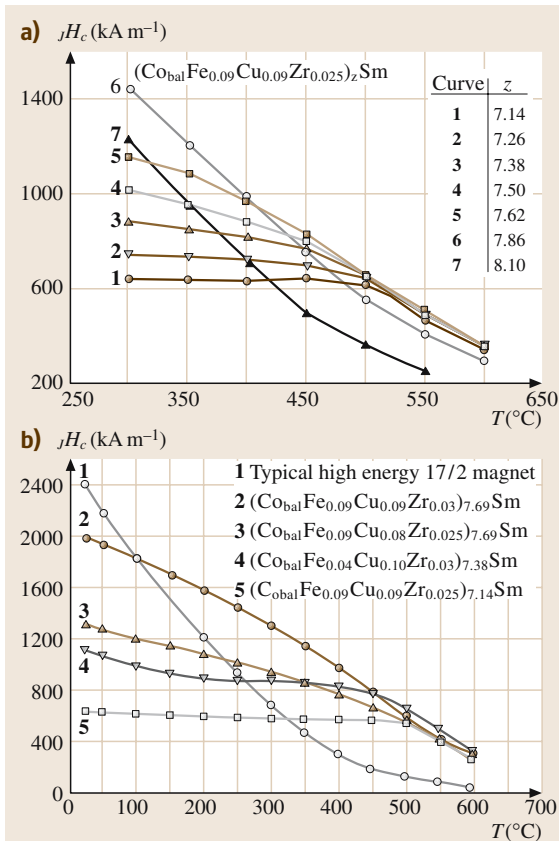
Fig. 4.3-68a,b Temperature dependence of $_JH_c$ for $(Co_{bal}Fe_vCu_yZr_x)_z$ as varied by the concentration of the substitutional elements and of Sm [3.10] **(a)** Dependence on the TM/Sm ratio; **(b)** Dependence on other variations in chemical composition
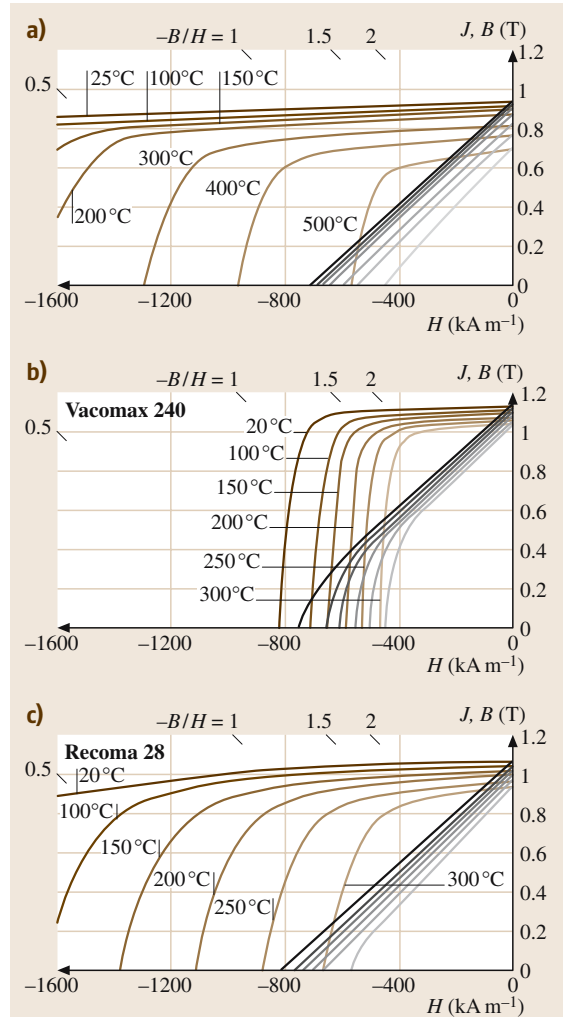

Fig. 4.3-69a–c $TM_{17}Sm_2$ magnets. Demagnetization curves [3.10] **(a)** Magnet may be used up to 500 °C. Coating is needed for protection against oxidation > 300 °C. **(b)** Low coercivity, easy-to-magnetize magnet. **(c)** High energy, high coercivity magnet

4.3.3.6 Mn−Al−C

In the binary Mn−Al system the ferromagnetic, metastable τ-Mn−Al phase containing 55 wt% Mn is obained by annealing at 923 K, or by controlled cooling of the stable ε phase from $\geq$ 1073 K. The τ phase has a high magnetocrystalline anisotropy $K_1 \cong 10^6$ J m^{-3} and $I_s = 0.6$ T. The magnetic easy axis is the c axis. The τ phase can be stabilized by adding 0.5 wt% C. Hot deformation at about 973 K permits formation of
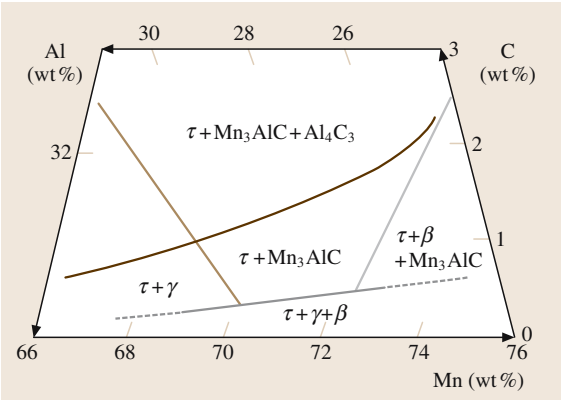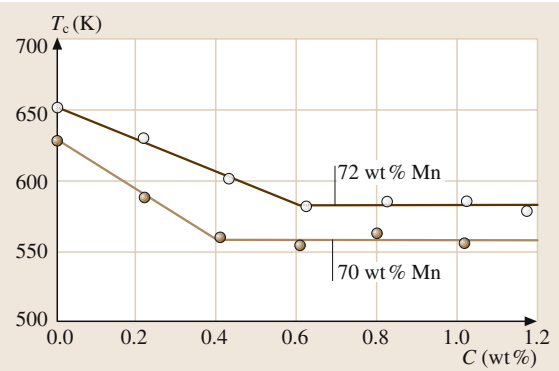

Fig. 4.3-71 Dependence of Curie temperature of τ-Mn−Al−C on the carbon concentration [3.10]

anisotropic magnets. Figure 4.3-70 shows schematically the 873 K isotherm of the Mn−Al−C phase diagram.

Carbides coexist with the metallic ferromagnetic phases. This is unfavorable for the mechanical properties. The Curie temperature of the τ phase decreases with increasing C content to a constant value (see Fig. 4.3-71) according to the phase diagram.

An alternative process to form τ-Mn−Al−C magnets is to use gas-atomized powder which is canned
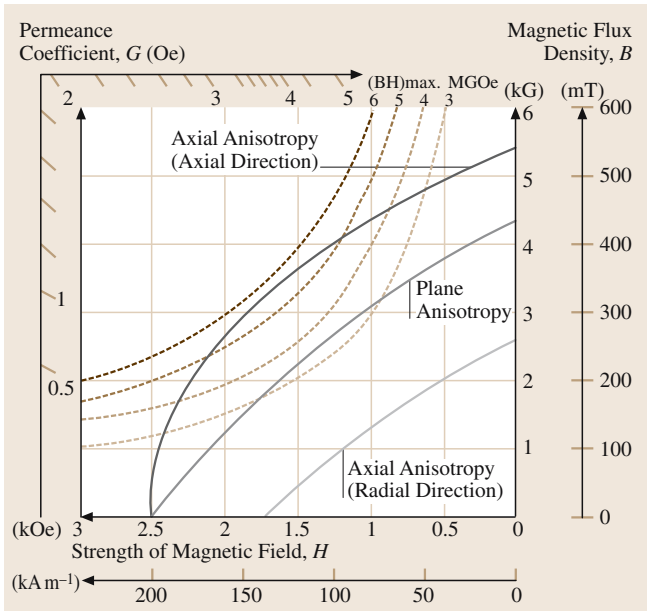

Fig. 4.3-70 Schematic representation of the phase relations of Mn−Al−C at 873 K [3.10]

Fig. 4.3-72 Magnetic properties of an extruded Mn−Al−C magnet [3.10]

Table 4.3-51 Properties of a Mn−Al−C magnet [3.10]

| | | Axial Anisotropy | | Plane anisotropy |
		Axial direction	Radial direction	
Maximum energy product $(BH)_{max}$	$(kJ\,m^{-3})$	44	10	28
Residual magnetic flux density B_r	(mT)	550	270	440
Coercivity H_c	$(kA\,m^{-1})$	200	144	200
Optimum permeance coefficient	$(\mu H\,m^{-1})$	1.9	1.9	1.9
Average reversal permeability	$(\mu H\,m^{-1})$	$1.4 \sim 1.6$	$1.4 \sim 1.6$	$1.4 \sim 1.6$
Temperature coefficient of B_r	$(\%\,K^{-1})$	-0.11	-0.11	-0.11
Curie point T_c	(K)	573	573	573
Maximum operating temperature	(K)	773	773	773
Density	$(kg\,m^{-3})$	5100	5100	5100
Hardness	(HR_c)	$49 \sim 56$	$49 \sim 56$	$49 \sim 56$
Tensile strength R_m	$(N\,m^{-2})$	$> 290 \times 10^6$	$> 290 \times 10^6$	$> 290 \times 10^6$
Compression strength	$(N\,m^{-2})$	$> 2000 \times 10^6$	$> 2000 \times 10^6$	$> 2000 \times 10^6$

and extruded at 973 K. By atomizing, the powder is rapidly quenched and consists of the high temperature ε phase. During hot extrusion it transforms to the axi-ally anisotropic τ phase. Repeated die pressing results in plane anisotropy. The magnetic properties are shown in Fig. 4.3-72 and listed in Table 4.3-51.

4.3.4 Magnetic Oxides

The magnetic properties of oxides and related compounds have been tabulated in comprehensive data collections [3.4]. A review of the basic magnetic properties of garnets $\{A_3\}[B_2](Si_3)O_{12}$ and spinel ferrites $MeOFe_2O_3$ or $Me^{II}Fe_2^{III}O_4$ is given by *Guillot* in [3.3].

4.3.4.1 Soft Magnetic Ferrites

Both MnZn and NiZn ferrites are the common designations of the two main groups of soft magnetic oxide materials. A more extensive account is given in [3.10]. The chemical formula of MnZn and NiZn ferrites is $M^{2+}Fe_2O_4$ and they have spinel structures. The divalent ions (M^{2+}) are elements such as Mn, Fe, Co, Ni, Cu, Mg, Zn, and Cd. They are located at tetrahedral or octahedral sites of the spinel structures. Ceramic processing methods are applied to produce the magnetic parts such as ring-shaped cores for inductive components.

The use of different types of MnZn and NiZn ferrite materials varies with the operating frequency in the application concerned. Figure 4.3-73 and Table 4.3-52 indicate the typical ranges of use and the magnetic properties of characteristic materials. Typically, MnZn ferrites are used in the range of several MHz. Table 4.3-53 lists the major applications with the perti-nent operating frequencies. Since a phase shift occurs in an ac-excited magnetic field, the permeability μ is expressed as a complex number, $\mu' - i\mu''$. The imaginary
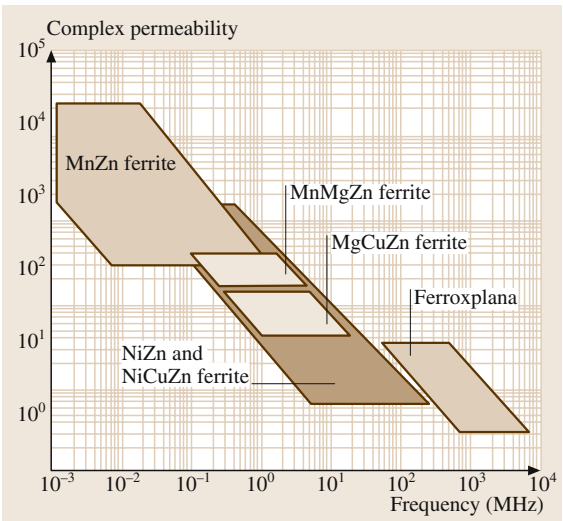

Fig. 4.3-73 Relationships between frequency and complex permeability of groups of characteristic soft magnetic ferrites [3.10]

Table 4.3-52 Typical magnetic properties of characteristic materials [3.10]

Type	MnZn ferrite					NiCuZn ferrite		
Designation	PC40	PC44	PC45	PC50	H5C4	L7H	HF70	L6
μ_i	2300	2400	2500	1400	12 000	800	1300	1500
B_s (mT) at 25 °C	510	510	530	470	380	390	270	280
H_c (A m^{-1}) at 25 °C	14	13	12	37	4	16	16	16
T_c (°C)	>215	>215	>230	>240	>110	>180	>110	>110
ρ_v (m)	6.5					10^6	10^6	10^6
Pcv (kW m^{-3})	410	300	250	80^a				
At 100 kHz, 200 mT	(100 °C)	(100 °C)	(75 °C)	(100 °C)				

^{a} At 500 kHz, 50 mT

Table 4.3-53 Ferrite applications [3.10]

| Application	Frequency	Ferrite material
Communication coils	1 kHz ~ 1 MHz	MnZn
	0.5 ~ 80 MHz	NiZn
Pulse transformers		MnZn, NiZn
Transformers	~ 300 kHz	MnZn
Flyback transformers	15.75 kHz	MnZn
Deflection yoke cores	15.75 kHz	MnZn, MnMgZn, NiZn
Antennas	0.4 ~ 50 MHz	NiZn
Intermediate frequency transformers	0.4 ~ 200 MHz	NiZn
Magnetic heads	1 kHz ~ 10 MHz	MnZn
Isolators		MnMgAl
Circulators	30 MHz ~ 30 GHz	YIG
Splitters		YIG
Temperature responsive switches		MnCuZn
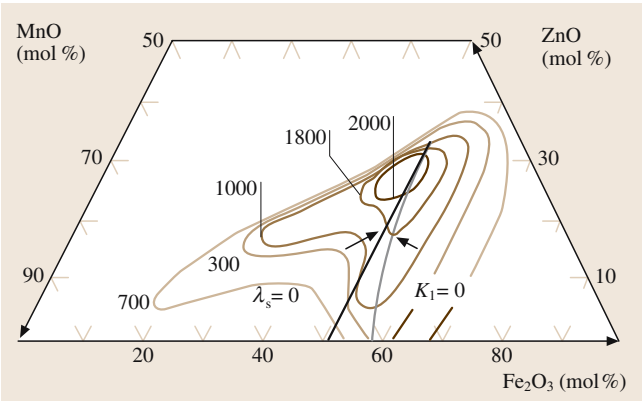
Fig. 4.3-74 Relationship between composition and complex permeability in MnZn ferrites [3.10]

part, μ'', is related to magnetic losses and is high at the resonance frequency. For a specific composition range, the values of magnetic anisotropy and magnetostriction are reduced to near zero leading to a maximum in complex permeability, as shown in Fig. 4.3-74. By suitable control of the microstructure it is possible to favor the formation and mobility of fast-moving domain walls. Consequently, the permeability of MnZn ferrite is the highest among the ferrites with spinel structure. However, the increase of the loss factor is considerably enhanced with increasing frequency because of the lower resistivity of MnZn ferrites compared to other ferrite materials.

The properties of NiZn and NiCuZn ferrites are designed for applications in the radio wave band. Figure 4.3-75 shows the effect of the Zn content on
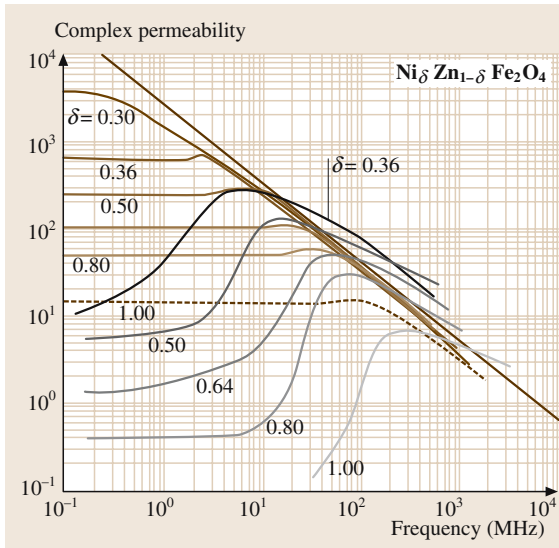
Fig. 4.3-75 Frequency dependence of the complex permeability in NiZn ferrites. *Solid* and *dashed lines* refer to the real and the imaginary part, respectively [3.10]

the complex permeability spectra of NiZn ferrites. In general, the high-permeability materials cause lower resonance frequencies.

4.3.4.2 Hard Magnetic Ferrites

A hard magnetic ferrite, also called ferrite magnet, is a magnetic material based on iron oxide. The composition of the typical hard magnetic ferrite compounds is shown in Table 4.3-54. M type material is used most widely and BaO can be replaced by SrO.

Figure 4.3-76 shows the quasi-binary phase diagram $BaO–Fe_2O_3$. The composition of the actual industrial hard magnetic ferrite is selected to deviate slightly from the stoichiometric composition in order to provide easy wetting and permit liquid-phase sintering. The ferromagnetic phase $SrO·6Fe_2O_3$ has a higher magnetocrystalline anisotropy constant K_1 and, thus, a higher intrinsic coercive force $_JH_c$ than the BaO-based compound.

Table 4.3-55 shows the basic magnetic properties of hard magnetic ferrites. The properties of actual products are shown in Fig. 4.3-77. The demagnetization curves of type YBM-9B, which have the best magnetic properties, are shown in Fig. 4.3-78.

Comparing hard ferrites and rare earth magnets, the ratio of remanence B_r is about $1:3$, that of the coercivity $_JH_c$ is also about $1:3$, such that the ratio of the energy product $(BH)_{max}$ is about $1:10$. From the cost/performance point of view, the rare earth magnets are used where weight and size are essential.
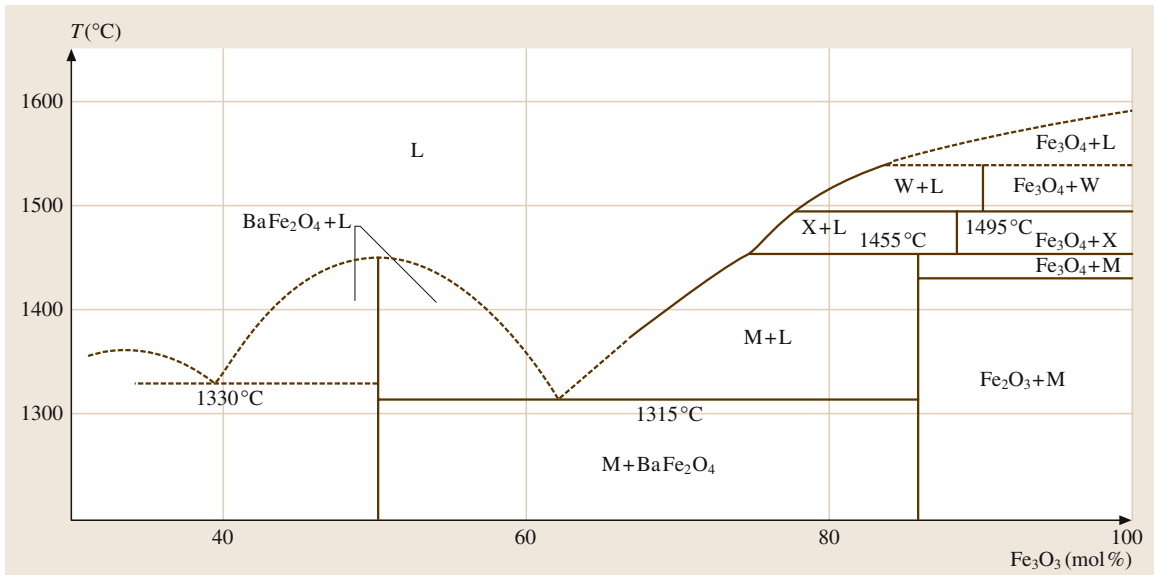
Part 4 | 3.4

Fig. 4.3-76 Quasi-binary phase diagram $BaO–Fe_2O_3$. $p(O_2) = 1$ atm; $X = BaO·FeO·7Fe_2O_3$; $W = BaO·2FeO·8Fe_2O_3$. *van Hook* 1964 [3.10, 59]

Table 4.3-54 BaO−MeO−Fe$_2$O$_3$ hexagonal magnetic compounds and their technical designations as hard ferrite materials 3.10

Designation symbol	Molecular formula	Chemical composition (mol%)		
		MeO	BaO	Fe$_2$O$_3$
M	BaO·6Fe$_2$O$_3$	–	14.29	85.71
W	2MeO·BaO·8Fe$_2$O$_3$	18.18	9.09	72.71
Y	2MeO·2BaO·6Fe$_2$O$_3$	20	20	60
Z	2MeO·3BaO·12Fe$_2$O$_3$	11.76	17.65	70.59

Table 4.3-55 Magnetic properties of hard ferrites 3.10

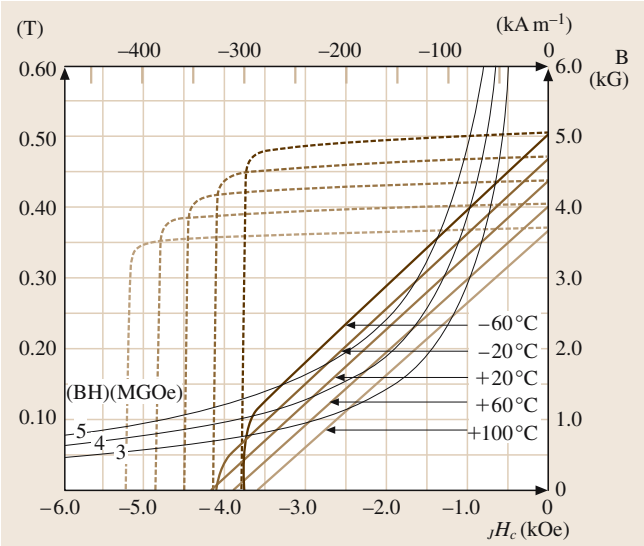| Composition	σ_s (10^{-4} Wb m kg^{-1})	(emu g^{-1})	σ_o (10^{-4} Wb m kg^{-1})	(emu g^{-1})	J_s (wb m^{-3})	T_c (K)	K_1 (10^3 J m^{-2})	H_a (kA m^{-1})	D_c (μm)
BaFe$_{17}$O$_{19}$	0.89	71	1.257	100	47.8	723	3.2	1.350	0.90
SrFe$_{17}$O$_{19}$	0.905	72	1.357	108	47.8	735	3.5	1.590	0.94

Fig. 4.3-78 Demagnetization behavior and its temperature dependence of a hard ferrite YBM9B (Hitachi Metals) 3.10
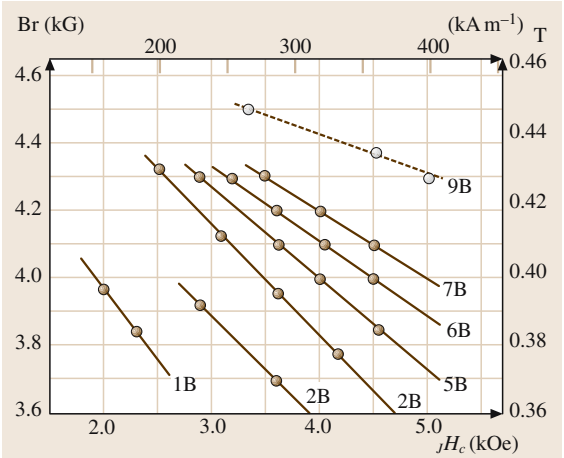

Fig. 4.3-77 Magnetic properties of ferrite magnets (Hitachi Metals series YBM 1B-9B) 3.10

References

3.1   K. H. J. Buschow: Electronic and Magnetic Properties of Metals and Ceramics, Part I. In: *Materials Science and Technology*, Vol. 3, ed. by R. W. Cahn, P. Haasen, E. J. Kramer (VCH, Weinheim 1991)

3.2   H. P. J. Wijn (Ed.): *Magnetic Properties of Metals*, Landolt−Börnstein, New Series III/19, 32 (Springer, Berlin, Heidelberg 1986−2001)

3.3   K. H. J. Buschow: Electronic and Magnetic Properties of Metals and Ceramics, Part II. In: *Materials Science and Technology*, Vol. 3, ed. by R. W. Cahn, P. Haasen, E. J. Kramer (VCH, Weinheim 1994)

3.4   K.−H. Hellwege, A. M. Hellwege (Eds.): *Magnetic and Other Properties of Oxides and Related Compounds*, Landolt−Börnstein, New Series III/4, 12 (Springer, Berlin, Heidelberg 1970−1982)

3.5   H. P. J. Wijn (Ed.): *Magnetic Properties of Non-Metallic Inorganic Compounds Based on Transition Metals*, Landolt−Börnstein, New Series III/27 (Springer, Berlin, Heidelberg 1988−2001)

3.6   K. Adachi, D. Bonnenberg, J. J. M. Franse, R. Gersdorf, K. A. Hempel, K. Kanematsu, S. Misawa, M. Shiga, M. B. Stearns, H. P. J. Wijn: *Magnetic*

Properties of Metals: 3d, 4d, 5d Elements, Alloys, Compounds, Landolt–Börnstein, New Series III/19 (Springer, Berlin, Heidelberg 1986)

3.7 G. Bertotti, A. R. Ferchmin, E. Fiorello, K. Fukamichi, S. Kobe, S. Roth: *Magnetic Alloys for Technical Applications. Soft Magnetic Alloys, Invar, Elinvar Alloys*, Landolt–Börnstein, New Series III/19, ed. by H. P. J. Wijn (Springer, Berlin, Heidelberg 1994)

3.8 R. Boll: *Soft Magnetic Materials* (Heyden & Son, London 1979)

3.9 J. Evetts: Concise Encyclopedia of Magnetic & Superconducting Materials. In: *Advances in Materials Science, Engineering* (Pergamon Press, Oxford 1992)

3.10 P. Beiss, R. Ruthardt, H. Warlimont (Eds.): *Advanced Materials, Technologies: Materials: Powder Metallurgy Data: Metals, Magnets*, Landolt–Börnstein, New Series VIII/2 (Springer, Berlin, Heidelberg 2003)

3.11 K. Günther: SMM Conference 2003

3.12 R. Boll: Soft Magnetic Metals and Alloys. In: *Materials Science and Technology*, Vol. 3B, ed. by K. H. J. Buschow (VCH, Weinheim 1994) pp. 399–450

3.13 Bölling and Hastenrath

3.14 G. Rassmann, U. Hofmann: Magnetismus, Struktur und Eigenschaften magnetischer Festkörper. In: (VEB Deutscher Verlag für Grundstoffindustrie, Leipzig 1967) pp. 176–198

3.15 G. Rassmann, U. Hofmann: J. Appl. Phys. **39**, 603 (1968)

3.16 R. Boll: *Weichmagnetische Werkstoffe*, 4 edn. (Vacuumschmelze, 1990)

3.17 H. Saito (Ed.): *Physics and Application of Invar Alloys* (Maruzen Company, Ltd., Tokyo 1978)

3.18 O'Handley 1977

3.19 Hilzinger 1980

3.20 Miyazaki 1972

3.21 Fujimori 1976

3.22 Allied Signal: Technical Bulletin 9 (1998)

3.23 H. Herzer: Nanocrystalline Soft Magnetic Alloys. In: *Handbook of Magnetic Materials*, ed. by K. H. J. Buschow (Elsevier, Amsterdam 1997) pp. 416–462

3.24 Hono and Sakurai 1995

3.25 M. Müller, N. Mattern, L. Illgen, H. R. Hilzinger, G. Herzer: Key Eng. Mater. **81–83**, 221–228 (1991)

3.26 M. Müller, N. Mattern, L. Illgen: Z. Metallkunde **82**, 895–901 (1991)

3.27 G. Herzer: IEEE Trans. Magn. Mag. **26**, 1397 (1990)

3.28 *Herzer* 1990

3.29 *Herzer* 1990–1995

3.30 *Herzer* and *Warlimont* 1992

3.31 *Sawa* and *Takahashi* 1990

3.32 *Suzuki* et al. 1991

3.33 *Guo* et al. 1991

3.34 *Pfeifer* and *Radeloff* 1980

3.35 *Arai* et al. 1984

3.36 Y. Yoshizawa, S. Oguma, K. Yamauchi: J. Appl. Phys. **64**, 6044 (1988)

3.37 K. Suzuki, A. Makino, N. Kataoka, A. Inoue, T. Masumoto: Mater. Trans. Japn. Inst. Met. (JIM) **32**, 93 (1991)

3.38 K. Suzuki, A. Makino, N. Kataoka, A. Inoue, T. Masumoto: J. Appl. Phys. **74**, 3316 (1993)

3.39 *Masumoto*

3.40 *Kussmann* and *Jessen*

3.41 K. Fukamichi: *Magnetic Properties of Metal*, Landolt–Börnstein, New Series III/19, ed. by H. P. J. Wijn (Springer, Berlin, Heidelberg 1994) pp. 193–238

3.42 M. Shiga: Invar Alloys. In: *Materials Science and Technology*, Vol. 3B, ed. by K. H. J. Buschow (VCH, Weinheim 1994) pp. 161–207

3.43 *Patrick*

3.44 *Fujimori* and *Kaneko*

3.45 C. E. Guillaume: C.R. hebd. Séances Acad. Sci. **1244**, 176–179 (1897)

3.46 P. Chevenard, X. Waché, A. Villechon: Ann. France Chronométrie , 259–294 (1937)

3.47 M. Müller: . Ph.D. Thesis (Akademie der Wissenschaften der DDR, Berlin 1977)

3.48 M. Kersten: Z. Phys. **85**, 708 (1933)

3.49 R. Becker, W. Döring: *Ferromagnetismus* (Springer, Berlin 1939) p. 340

3.50 G. Hausch: Phys. Stat. Sol. (a) **15**, 501 (1973) **16 (1973), 371**

3.51 M. Müller: . Ph.D. Thesis (Technische Universität Dresden, Dresden 1969)

3.52 H. Masumoto, S. Sawaya, M. Kikuchi: J. Japn. Inst. Met. (JIM) **35**, 1143, 1150 (1971) **36 (1972), 57, 176, 492, 498, 881, 886, 1116**

3.53 M. Müller: J. Magn. Magn. Mater. **78**, 337 (1989)

3.54 P. E. Armstrong, J. M. Dickinson, A. L. Brown: Trans. AIME **236**, 1404 (1966)

3.55 E. P. Wohlfahrt: Hard Magnetic Materials. Advances in Physics, Phil. Mag. **A8** (1959)

3.56 D. Bonnenberg, K. Burzo, K. Fukamichi, H. P. Kirchmayr, T. Nakamichi, H. P. J. Wijn: *Magnetic Properties of Metals: Magnetic Alloys for Technical Applications. Hard Magnetic Alloys*, Landolt–Börnstein, New Series III/19 (Springer, Berlin, Heidelberg 1992)

3.57 WIDIA Magnettechnik, Gesinterte Dauermagnete Koerzit und Koerox, d.2000.D.5

3.58 C. Abache, H. Oesterreicher: J. Appl. Phys. **57**, 4112 (1985)

3.59 *van Hook* 1964

Part 4 | 3